

MONITORING AIR FLOW AND WATER MOVEMENT IN THE
SUBSURFACE WITH CROSS-BOREHOLE RESISTIVITY
AND INDUCED POLARIZATION

by

Susan Anastasia Schima

A Thesis Submitted to the Faculty of the
DEPARTMENT OF MINING AND GEOLOGICAL ENGINEERING
In Partial Fulfillment of the Requirements
For the Degree of
MASTER OF SCIENCE
WITH A MAJOR IN GEOLOGICAL AND GEOPHYSICAL ENGINEERING
In the Graduate College
THE UNIVERSITY OF ARIZONA

1 9 9 4

STATEMENT BY AUTHOR

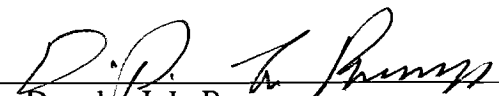
This thesis has been submitted in partial fulfillment of requirements for an advanced degree at The University of Arizona and is deposited in the University Library to be made available to borrowers under rules of the Library.

Brief quotations from this thesis are allowable without special permission, provided that accurate acknowledgment of source is made. Requests for permission for extended quotation from or reproduction of this manuscript in whole or in part may be granted by the head of the major department or the Dean of the Graduate College when in his or her judgment the proposed use of the material is in the interests of scholarship. In all other instances, however, permission must be obtained from the author.

SIGNED: 

APPROVAL BY THESIS DIRECTOR

This thesis has been approved on the date shown below:

 9/7/94
Douglas J. LaBrecque Date
Assistant Professor of Geological
and Geophysical Engineering

ACKNOWLEDGMENTS

Throughout the course of my graduate research, I have been supported and assisted by many people and organizations that I would like to here thank.

During field work at Avra Valley, Arizona, I was grateful to Jose Arce for developing field system software and, together with Qin Jizeng and Robert Mallan, for assisting with field work. The lined basin in which the studies of this thesis were carried out was constructed with funding from the Electric Power Research Institute (EPRI), contract RP 2485-11, principal investigators being Ben K. Sternberg, Mary M. Poulton, Michael J. Sully, and Shlomo P. Neuman.

During field work in Florence, Oregon, I was grateful to Todd Ririe, Paul Lundegard, Dave Yasumura, and Dong Li of the Fred L. Hartley Research Center for providing information and assisting with field work. I would like to thank UNOCAL Corporation for funding the study. I greatly appreciate the help of Marcella Boyer, Brad Baird, and George Saunders of GeoEngineers for assisting with well installation. I would also like to thank Tim Olsen for assisting with the construction of electrodes and circuit boards.

Finally, I would like to express my sincere appreciation to Douglas J. LaBrecque for his invaluable guidance, Thomas Maddock III, Ben K. Sternberg, and the Laboratory for Advanced Subsurface Imaging at The University of Arizona.

DEDICATION

I dedicate this Masters Thesis to Dr. Gerardo W. Gross at the New Mexico Institute of Mining and Technology, for without whom, I never would have been at The University of Arizona.

TABLE OF CONTENTS

	Page
LIST OF ILLUSTRATIONS	7
LIST OF TABLES	12
ABSTRACT.....	13
1. INTRODUCTION.....	14
Background.....	14
Previous Studies.....	15
2. THEORY.....	18
Rock Properties.....	18
Tomography.....	21
Finite Element Mesh Design.....	26
Two Dimensional Solution.....	26
Axially Symmetric Solution.....	28
Data Interpretation.....	30
3. AVRA VALLEY, ARIZONA.....	31
Introduction.....	31
Site Description.....	32
Purpose.....	38
Data Acquisition.....	39
Field Measurements.....	39
In Lab Rock Properties Measurements.....	42
Expected Results.....	47
Rock Properties Measurements.....	47
EM39 Logs.....	47
Results.....	53
Resistivity Reconstructions.....	53
Percent Difference Images.....	57
Induced Polarization.....	60
Conclusions.....	65
3. FLORENCE, OREGON.....	66
Introduction.....	66
Site Description.....	67
Purpose.....	71
Data Acquisition.....	71
Field Measurements.....	71
Air Sparging Process.....	80
Expected Results.....	82
Previous Studies.....	82
Results.....	84

TABLE OF CONTENTS - *Continued*

Resistivity Reconstructions.....	84
C Plane.....	84
H Plane.....	89
B Plane.....	91
Percent Difference Images.....	92
C Plane.....	92
H Plane.....	100
Water Saturation Images.....	101
Conclusions.....	109
5. SUMMARY.....	110
Closing Remarks.....	111
APPENDIX: Resulting Images from Florence, Oregon.....	112
REFERENCES.....	149

LIST OF ILLUSTRATIONS

Figure	Page
2.1	Simplified circuit diagram of apparatus used in rock properties measurements for Avra Valley sediments.....19
2.2	Finite element mesh design used to model the lined basin27
2.3	Foreground mesh28
2.4	Finite element mesh design used to model axial symmetry around the Sparge Well29
3.1	Map of Avra Valley Geophysical Test Site33
3.2	Plan view of lined basin34
3.3	Cross-section of lined basin35
3.4	Plan view of lined basin showing all wells37
3.5	Cross-section of lined basin showing wells and electrodes39
3.6	Detail of water emitters in line source injection40
3.7	Monitor wells shown projected onto one line49
3.8	EM 39 survey from August 17, 199250
3.9	EM 39 survey from September 5, 199251
3.10	EM 39 survey from September 26, 199252
3.11	Background resistivity reconstruction, August 17 and 18, 1992.....54
3.12	Post-injection resistivity reconstruction, September 15, 199255
3.13	Post-injection resistivity reconstruction, January 28, 1993.....56
3.14	Percent difference of resistivity reconstruction, September 15, 199258
3.15	Percent difference of resistivity reconstruction, January 28, 199359

LIST OF ILLUSTRATIONS - *Continued*

3.16	Background IP reconstruction, August 17 and 18, 1992	62
3.17	Post-injection IP reconstruction, September 15, 1992	63
3.18	Post-injection IP reconstruction, January 28, 1993	64
4.1	The process of air sparging	66
4.2	Map view of field site in Florence, Oregon	68
4.3	Plan view of field site in Florence, Oregon	70
4.4	Plan view of well locations in Florence, Oregon	72
4.5	Cross-section of Sparge Well	74
4.6	Cross-section of Well 1	75
4.7	Cross-section of Wells 2 and 4	76
4.8	Cross-section of Well 3	77
4.9	Cross-section of Well 5	78
4.10	Detail of Electrode	79
4.11	Resistivity reconstruction, C Plane, Background, July 14, 1993	85
4.12	Percent difference reconstruction, C Plane, 20 min after sparge began, July 14, 1993	93
4.13	Percent difference reconstruction, C Plane, 1 hr after sparge began, July 14, 1993	94
4.14	Percent difference reconstruction, C Plane, 3 hr after sparge began, July 14, 1993	95
4.15	Percent difference reconstruction, C Plane, 1 hr after sparge off, July 14, 1993	97
4.16	Percent difference reconstruction, C Plane, after about 48 hr of continuous sparging, July 18, 1993	98
4.17	Percent difference reconstruction, C Plane, long term effects after sparge off, July 20, 1993	99

LIST OF ILLUSTRATIONS - *Continued*

4.18	Percent saturation reconstruction, C Plane, 20 min after sparge began, July 14, 1993	103
4.19	Percent saturation reconstruction, C Plane, 1 hr after sparge began, July 14, 1993	104
4.20	Percent saturation reconstruction, C Plane, 4 hr, 20 min after sparge began, July 14, 1993.....	105
4.21	Percent saturation reconstruction, C Plane, after second sparge, July 16, 1993	106
4.22	Percent saturation reconstruction, C Plane, 48 hr after continuous sparging, July 18, 1993	107
4.23	Percent saturation reconstruction, C Plane, long term effects, July 20, 1993	108
A1	Resistivity reconstruction, C Plane, 20 min after sparge began, July 14, 1993	113
A2	Resistivity reconstruction, C Plane, 1 hr after sparge began, July 14, 1993	114
A3	Resistivity reconstruction, C Plane, 3 hr after sparge began, July 14, 1993	115
A4	Resistivity reconstruction, C Plane, 4 hr, 20 min after sparge began, July 14, 1993	116
A5	Resistivity reconstruction, C Plane, 1 hr after sparge off, July 14, 1993	117
A6	Resistivity reconstruction, C Plane, 2 hr after sparge off, July 14, 1993	118
A7	Resistivity reconstruction, C Plane, Background, July 15, 1993	119
A8	Resistivity reconstruction, C Plane, 1 hr after sparge began, July 15, 1993	120
A9	Resistivity reconstruction, C Plane, 2 hr after sparge began, July 15, 1993	121
A10	Resistivity reconstruction, C Plane, 3 hr after sparge began, July 15, 1993	122

LIST OF ILLUSTRATIONS - *Continued*

A11	Resistivity reconstruction, C Plane, 1 hr after sparge off, July 15, 1993	123
A12	Resistivity reconstruction, C Plane, Background, July 16, 1993	124
A13	Resistivity reconstruction, C Plane, after 3 half-hour sparge events, July 16, 1993	125
A14	Resistivity reconstruction, C Plane, after about 24 hr continuous sparging, July 17, 1993	126
A15	Resistivity reconstruction, C Plane, after about 42 hr of continuous sparging, July 18, 1993	127
A16	Resistivity reconstruction, C Plane, after about 47 hr of continuous sparging, July 18, 1993	128
A17	Resistivity reconstruction, C Plane, after about 48 hr of continuous sparging, July 18, 1993	129
A18	Resistivity reconstruction, C Plane, long term effects after sparge off, July 20, 1993	130
A19	Resistivity reconstruction, C Plane, long term effects after sparge off, July 21, 1993	131
A20	Resistivity reconstruction, C Plane, long term effects after sparge off, July 22, 1993	132
A21	Resistivity reconstruction, H Plane, Background, July 20, 1993	133
A22	Resistivity reconstruction, H Plane, 10 min after sparge began, July 20, 1993	134
A23	Resistivity reconstruction, H Plane, 20 min after sparge began, July 20, 1993	135
A24	Resistivity reconstruction, H Plane, 1 hr, 30 min after sparge began, July 20, 1993	136
A25	Resistivity reconstruction, H Plane, 2 hr, 20 min after sparge began, July 20, 1993	137
A26	Resistivity reconstruction, H Plane, 10 min after sparge off, July 20, 1993	138

LIST OF ILLUSTRATIONS - *Continued*

A27	Resistivity reconstruction, H Plane, 20 min after sparge off, July 20, 1993	139
A28	Resistivity reconstruction, B Plane, Background, July 13, 1993	140
A29	Resistivity reconstruction, B Plane, Background, July 14, 1993	141
A30	Resistivity reconstruction, B Plane, 1 hr, 30 min after sparge began, July 14, 1993	142
A31	Percent difference reconstruction, H Plane, 10 min after sparge began, July 20, 1993	143
A32	Percent difference reconstruction, H Plane, 20 min after sparge began, July 20, 1993	144
A33	Percent difference reconstruction, H Plane, 1 hr, 30 min after sparge began, July 20, 1993	145
A34	Percent difference reconstruction, H Plane, 2 hr, 20 min after sparge began, July 20, 1993	146
A35	Percent difference reconstruction, H Plane, 10 min after sparge off, July 20, 1993.....	147
A36	Percent difference reconstruction, H Plane, 20 min after sparge off, July 20, 1993	148

LIST OF TABLES

Table		Page
3.1	Graph of cumulative water injection for lined basin experiment	41
3.2	Graph of Bulk Resistivity Vs Water Resistivity and Salinity	43
3.3	Graph of Chargeability Vs Water Resistivity and Salinity	44
3.4	Graph of bulk conductivities determined by the Waxman-Smits equation for 20%, 50%, and 100% water saturation Vs pore water conductivity ...	45
3.5	Graph of bulk conductivities determined from actual laboratory measurements and predicted by the Waxman-Smits equation Vs pore water conductivity	46
4.1	Table of the schedule of air sparge and vacuum extraction events	81
4.2	Graph of Water Saturation Vs Bulk Resistivity	83

ABSTRACT

The research included in this thesis consists of the following two geophysical surveys: a cross-borehole resistivity and induced polarization tomography survey to track the flow of water in the unsaturated zone at Avra Valley, Arizona; and a cross-borehole resistivity tomography survey to monitor air flow resulting from air sparging in the saturated zone in Florence, Oregon.

In Avra Valley, the resistivity decreases from background values in the areas saturated by the injected water, while the IP in these saturated areas increases, indicating that salts may have been flushed out by the descending water.

In Florence, Oregon, resistivity increases from background values, delineating the cone-shaped region beginning at the injection point and extending up to the water table where air has displaced water in the saturated zone during sparging, and delineating entrapped air below the water table long after sparging has ceased.

CHAPTER 1

INTRODUCTION

Background

Due to the growing concern for environmental protection, there is a need for technology which is able to accurately and efficiently assess contaminated sites. The migration and size of a contaminated area in the subsurface are strongly influenced by the often complex hydraulic and lithologic characteristics of the soil. Furthermore, numerical simulations or scaled experiments have not proven to be an adequate means for modeling the true nature of heterogeneous soil. What is required to effectively evaluate a contaminated site is a method applied on a field scale with high resolution that can delineate inhomogeneities in the soil over time.

One means of generating images of the underground is resistivity and induced polarization tomography. The resistivity of a material is the measured resistance to the passage of electrical current through a 1 m by 1 m by 1 m cube of material. Induced polarization (IP) is the time or frequency varying resistivity that occurs when the current is suddenly interrupted. When the current is interrupted, the voltage will gradually decay after an initial large decrease. In the time domain, the IP is measured as the area under this decay curve at regular time intervals and is called chargeability. Once the current is turned on again, the potential gradually builds up after a large initial increase. Resistivity will decrease as the frequency of the applied current increases. In this thesis, IP was measured in the time domain as chargeability.

Both resistivity and IP data can be collected simultaneously in a survey. In my research, cross-borehole surveys were conducted to collect resistivity and IP measurements. A cross-borehole survey uses electrodes arranged down-hole at regular spacings that are used as both current transmitters and voltage receivers.

Current is transmitted through a pair of electrodes in one well, the voltage is received by a pair of electrodes in the other well, and the resistivity is calculated. After numerous measurements have been made between two boreholes, the data points are combined to calculate the distribution of resistivity between boreholes. The result is a tomographic image that detects anomalies between the boreholes based on their resistive signatures. Taken over time, these images can be used to track changes occurring in the anomalies between boreholes.

I applied cross-borehole resistivity tomography to two different field studies, one of which included IP tomography. The first field site to be discussed was in Avra Valley, Arizona, in which I conducted resistivity and IP tomography surveys to track the flow of water injected into a lined basin. This study was conducted to gain a better understanding of fluid transport in the unsaturated, or vadose, zone. In the second field site in Florence, Oregon, I conducted resistivity surveys to track the flow of air injected in the saturated zone from a borehole. At this site, subsurface hydrocarbon contaminants were being remediated by "air sparging," a relatively new and inadequately understood method of volatile organic clean-up. The cross-borehole survey was among the first attempts to monitor air sparging on a field scale and learn more about this remediation technique from actual field data rather than lab data.

Previous Studies

The term "resistivity tomography" was first used by Shima and Sakayama, 1987 for describing the method of reconstructing a resistivity distribution between wells based on dense data sampling. Later, Shima, 1990, proposed a two-dimensional inversion technique that uses alpha centers for the analysis of direct current (DC) resistivity data as a more effective alternative to finite-element or finite-difference methods. A non-linear transformation, the alpha center method, was applied to the

DC continuity equation, enabling the potential and conductivity for any point to be expressed quickly as a simple numerical sum. One of the numerical experiments conducted using alpha centers simulated cross-borehole data collection. The analysis suggested that complex, two-dimensional structures can be accurately resolved by this technique, reinforcing its wide applicability.

Sasaki, 1992, examined the following factors that affect the resolution of resistivity tomography using a numerical simulation: block size, damping factor, choice of electrode array, and presence of an outside anomaly. The inversion used was a smoothness-constrained least squares and finite element method combination. When the model for inversion consists of blocks, the block size in the region of interest that gave the best results was a size equal to half the minimum electrode spacing. The resolution was found not to be sensitive to Gaussian noise, providing the damping factor, λ , even though it significantly affects the resolution, is properly chosen according to noise levels. The pole-dipole array gave the best compromise between high signal strength and resolution than either the dipole-dipole or pole-pole arrays. Finally, an anomaly outside the region of interest need not adversely affect resolution and accuracy if the block discretization reflects resistivity variations from the outside as well as the inside.

In another study by LaBrecque, 1991, stabilized tomographic inversion was applied to IP data to determine if there was a correlation between IP response and an oil bearing zone of the subsurface. In these results, IP responses were seen in the oil producing zone and additionally in a shale layer above the zone, indicating the ability of a tomographic inversion to effectively display an IP signature.

In a study by Daily et al., 1992, cross-borehole electrical resistance tomography (ERT) was used to image the movement of injected water into the vadose zone in two field scale sites. In both cases, the tomographs were able to show a progression of

water movement through time, and they agreed with other data and what was known of the lithology of the sites. This study shows electrical resistance tomography to be a useful tool for delineating an infiltration plume in a hydrologically complex environment.

In an environmental restoration study by Ramirez et al., 1993, ERT was employed to monitor the underground injection of a steam flood as a function of time. Dipole-dipole measurements of the bulk resistivity distribution were made where steam heated the native pore water of the soil. ERT proved to be an effective method for mapping the invasion of steam in the formation in space and time. Results indicated that the steam injection was constrained vertically by a gravel layer 3 m - 5 m thick from 39.5 m to 44.5 m, which was surrounded by layers of silt and clay. Horizontally, the steam injection reached all monitor wells, a distance of 18.3 m away from the injection well. ERT was determined to be an accurate technique for defining the location and size of the zone invaded by heated water.

In situ and in lab experiments have been carried out in the past to learn more about the process of air sparging, but none have used cross-borehole tomography. A laboratory study, conducted by Ji et al., 1993, shows that air flows in discrete channels, sensitive to heterogeneities, in medium to fine grained water saturated media. In an actual field application of sparging to environmental remediation, Brown et al., 1991, showed that at an injection depth between 30 ft (9.14 m) to 33 ft (10.06 m) depth, the radius of influence of the air attained a lateral extent of 70 ft (21.33 m) to 225 ft (68.58 m) from the point of injection. The study also indicated that the air injection was radially symmetric about the injection well, with no preference in orientation.

CHAPTER 2

THEORY

In this section of my thesis, I will discuss the finite element mesh and inversion used in the tomography for the two studies, Avra Valley and Florence, and also the theory behind the rock properties measurements that were conducted.

Rock Properties

The in-lab rock properties measurements of the sediments collected from the lined basin soil generated resistance and IP values. Resistance values were converted into resistivities in $\Omega\text{-m}$ by the following relation:

$$\rho = (R A)/L$$

where R is the measured resistance in Ω , A is the cross-sectional area of the sample in m^2 , and L is the length of the sample in m . Using the apparatus circuit design in Figure 2.1, $A = (0.028 \text{ m})^2 \times \pi$, and $L = 0.09 \text{ m}$.

IP values were converted to chargeability in mV/V by the following relation:

$$m = (1000 \times V)/V_0,$$

where V is the off-time voltage for each window [mV], V_0 is the on-time voltage [V]. These voltages are normalized as resistances, and thus are actually measured as resistances.

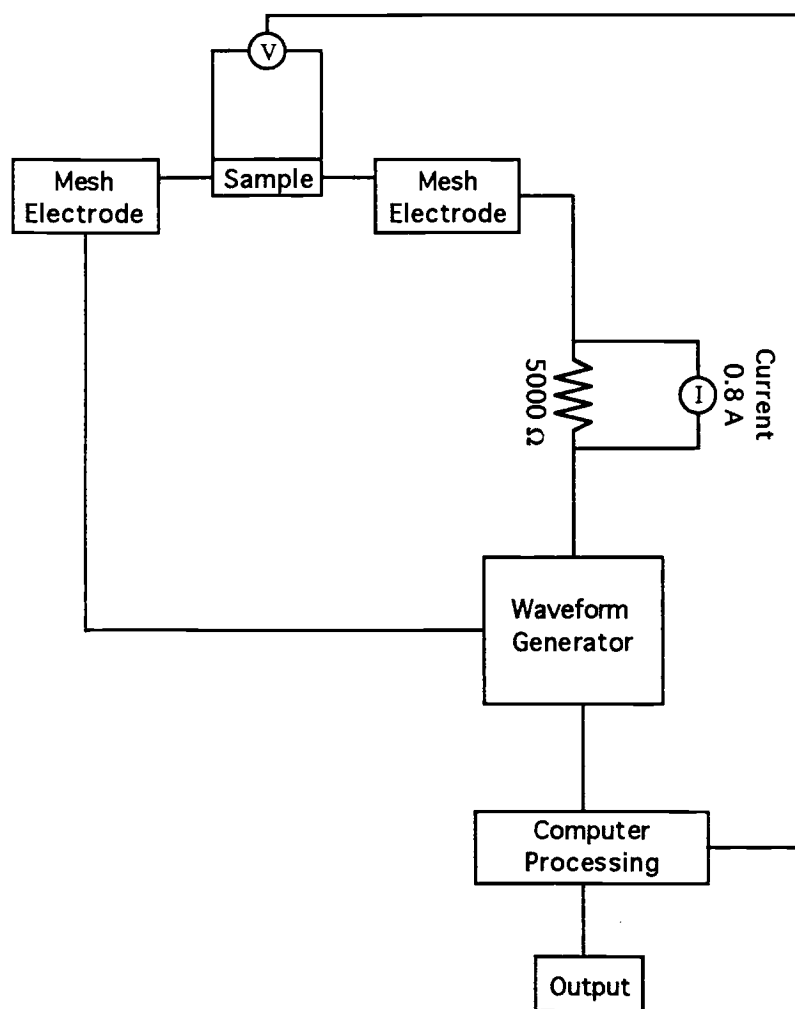


Figure 2.1 Simplified circuit diagram of apparatus used in rock properties measurements for Avra Valley sediments.

One of the models used to study bulk resistivity as a function of pore water salinity was the Waxman-Smits equation. The Waxman-Smits equation is a semi-empirical model that relates the electrical conductivity of water-saturated sediment to the water conductivity and cation-exchange capacity per unit pore volume of the rock. This equation can be used to predict the sediment conductivity/resistivity given the pore water conductivity/resistivity and can be used to solve for saturation. Because salinity is directly related to conductivity, the sediment conductivity/resistivity can be predicted knowing the pore water salinity, and then compared to actual values obtained from laboratory measurements.

The Waxman-Smits equation is based on Archie's Relation

$$\sigma_0 = \sigma_t / F$$

where F is the formation factor, σ_t is the total sum conductivity of the solution conductivity and an equivalent surface conductivity, and σ_0 is the bulk conductivity of the sediment (Klein and Sill, 1982). The Waxman-Smits equation is as follows:

$$\sigma_0 = (S_w^2)/F (\sigma_w + (Q B)/S_w)$$

where σ_0 is the bulk, or sediment, conductivity, measured in S/m; S_w is the water saturation of the sediment (unitless); F is the formation factor (unitless); σ_w is the pore water conductivity, measured in S/m; Q is the effective ratio of the cation-exchange capacity of the sediment divided by its pore volume, measured in equivalents/l; and B is an empirical parameter which represents the equivalent conductance of the counterions as a function of solution conductivity, measured in S/m milliequivalents/cm³ (Waxman and Smits, 1968).

The formation factor, F , is defined by the Winsauer equation (Waxman and Smits, 1968),

$$F = a \phi^{-m} S^{-n}$$

where a is a constant which incorporates the tortuosity changes for sandstones of differing porosities; ϕ is the porosity, assumed to be 45% for the sediments used based on laboratory results; m , the power of ϕ , is a cementation factor regulated by tortuosity, a unitless value assumed to be 2.15 for unconsolidated sediments; S is the saturation; and n , the power of S , is the saturation exponent, assumed to be 2 (Doveton, 1982). In this equation, 100% saturation is assumed and the constant a is 0.65. The Winsauer equation becomes

$$F = 0.65 \phi^{-2.15}$$

The empirical parameter B is defined as follows for NaCl solutions:

$$B = 3.83 [(1 - 0.83 e^{(-0.5/R)})]$$

where R is the resistivity of the pore water in $\Omega\text{-m}$ (Waxman and Thomas, 1974).

Tomography

Resistivity tomography is a method by which the resistance data collected between two boreholes are combined reconstructively to generate a resistivity distribution image between those two boreholes. The resulting image is a contoured

cross-section of the subsurface showing the geo-electric characteristics that exist, such as the location of water or air. Tomography was used in this study to reconstruct resistivity and IP images of the subsurface. For resistivity, the tomographic reconstruction uses a forward solution of Laplace's equation to calculate the electrical potential response of a two-dimensional earth from a three-dimensional source. The forward problem is as follows:

$$\nabla \times \sigma \nabla \phi = I \delta(\mathbf{r}_+),$$

where σ is conductivity, ϕ is electrical potential, I is current, δ is the delta function, and \mathbf{r} is the spatial covariance vector (Hohmann, 1988). The Fourier transform is taken as the derivative with respect to the Y direction as

$$\nabla_{xz} \times \sigma \nabla_{xz} \phi - \sigma K_y^2 f = I \delta(x_+, z_+),$$

where σ is the constant in the y direction and K_y is the transform variable.

The solution is approximated numerically using the method of finite elements. In the algorithm, the same electrode positions are used for current transmission and potential measurement within the borehole or along the surface, whether they be dipole-dipole measurements using electrode pairs, or pole transmissions using a distant electrode. In the finite element method, the true potential in the differential equation above is approximated by

$$\phi \cong \sum \phi_e \Gamma_e(x, z),$$

where Γ is a linear basis function extending over a finite range. The differential equation becomes a linear system of equations which can be solved for ϕ_e . The Fourier transform is performed numerically by integrating for ϕ .

The non-linear resistivity problem is

$$\mathbf{W} \mathbf{D} = \mathbf{W} \times \mathbf{F}(\mathbf{P}),$$

where \mathbf{D} is the vector of known data values, \mathbf{W} is a weighting matrix, the data covariance matrix, and $\mathbf{F}(\mathbf{P})$ is the forward solution.

This non-linear problem is approximated by the first order term of a Taylor series,

$$f(\sigma + \Delta \sigma) = f(\sigma) + \mathbf{A}(\Delta \sigma)$$

where \mathbf{A} is a rectangular sensitivity matrix, and

$$\Delta \sigma = (\mathbf{A}^T \mathbf{A} + \lambda \mathbf{I})^{-1} \mathbf{A}^T (\mathbf{D} - \mathbf{f}(\sigma))$$

where \mathbf{I} is the identity matrix and λ is the Marquardt factor, an arbitrary component.

The solutions were then inverted numerically using an Occam's style inversion which finds the model with the smoothest resistivity or IP section which fit the data within estimated standard deviations (LaBrecque et al., 1992). The Occam's inversion does this by treating the conductivities as values within the rectangular elements of the finite element mesh, not within the triangular subelements, resulting in the smoothest possible model.

In this method, the objective function,

$$\Psi (P) = X^2 (P) + \alpha \Omega (P)$$

is minimized finding the maximum value of α to get

$$X^2 (P) = X^2 \text{ a-priori,}$$

where $\Omega (P)$ is the model roughness and α is a stabilization parameter. The model roughness operator is defined as

$$\Omega (P) = P^T \mathbf{R} P,$$

where \mathbf{R} is the roughness matrix given by

$$\mathbf{R} = \underline{x}^T \underline{w}_x^T \underline{w}_x \underline{x} + \underline{z}^T \underline{w}_z^T \underline{w}_z \underline{z},$$

where \underline{x} and \underline{z} are the first order difference operators in the X and Z directions, respectively, and \underline{w}_x and \underline{w}_z are diagonal weighting matrices.

The IP data were modelled using a perturbation of the resistivity solution (LaBrecque, 1991 and Seigel, 1959). The percent frequency effect (PFE) is the measurement of resistivity at two or more frequencies given by

$$\text{PFE} = \frac{\rho_{\text{low}} - \rho_{\text{high}}}{\rho_{\text{low}}} \times 100 = \frac{\Delta \rho}{\rho} \times 100.$$

When the perturbation of resistivity is small, then the change in potential, ΔF_i , is approximated by

$$\Delta F_i \approx \frac{\Delta \rho}{\rho} \partial F_i.$$

Apparent PFE is given by

$$PFE_a = \frac{\Delta F_i}{F_i}$$

and approximated by

$$PFE_a \approx \frac{PFE}{F_i} \frac{\partial F_i}{\partial \rho} = - \frac{PFE}{F_i} \frac{\partial F_i}{\partial \log(\sigma)}.$$

The IP problem is linear, if IP effects are small perturbations of resistivity, making IP inverse modeling easier than resistivity inverse modeling. Furthermore, the partial derivatives with respect to conductivity are calculated during the inversion process, meaning little additional effort is needed to calculate IP values.

Finite Element Mesh Design

A mesh is used in the finite element method to approximate the two-dimensional earth cross-section. The array of the mesh consists of quadrilateral elements, which are subdivided into triangular sub-elements. The values of potentials at the corners of the sub-elements, the nodes, are determined by summing a series of subsectional basis functions to approximate the total potential throughout the mesh.

Two-Dimensional Solution

The finite element mesh used to model the planes between boreholes in the Avra Valley study is shown in Figure 2.2. The mesh consisted of a 57 by 24 element array, distorted at the lateral edges to account for the sloping basin. The array consists of quadrilateral pixels with a node at each corner. The portion of the array between a pair of wells, the foreground, shown in Figure 2.3, consists of an 8 element wide by 22 element long symmetrical mesh, each pixel equaling one element. This mesh represents the area that exists in the subsurface between a pair of wells, which is 2 m in width and 5.1 m in depth with 0.46 m spacing between electrodes. The foreground area is the only portion of the mesh that is contoured to create resistivity distribution images. The elements outside the bounds of the well are distorted to quadrilaterals rather than true rectangles. Also, outside of the well boundaries, the pixels are not equal to elements, but rather can contain several elements.

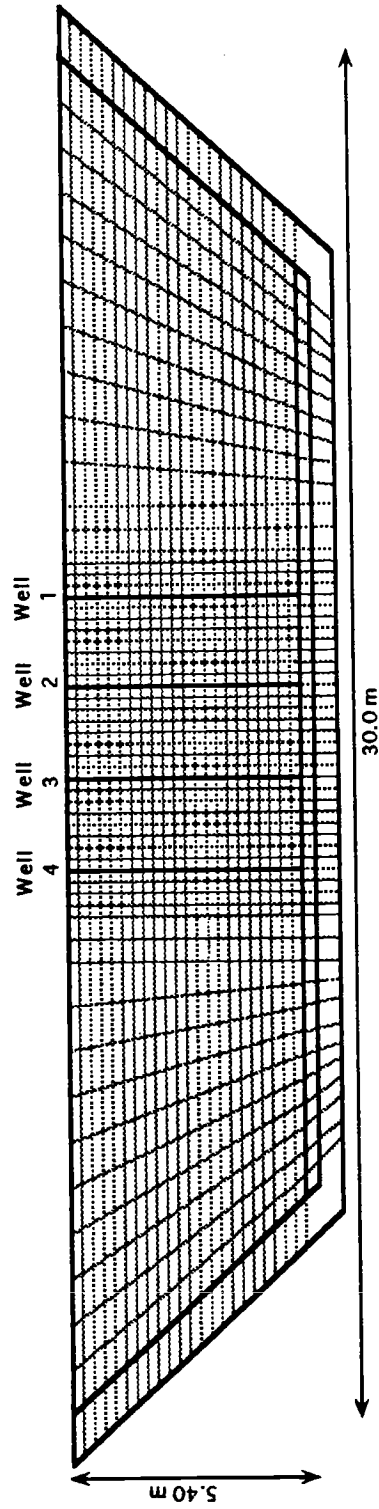


Figure 2.2. Finite element mesh design used to model the lined basin.

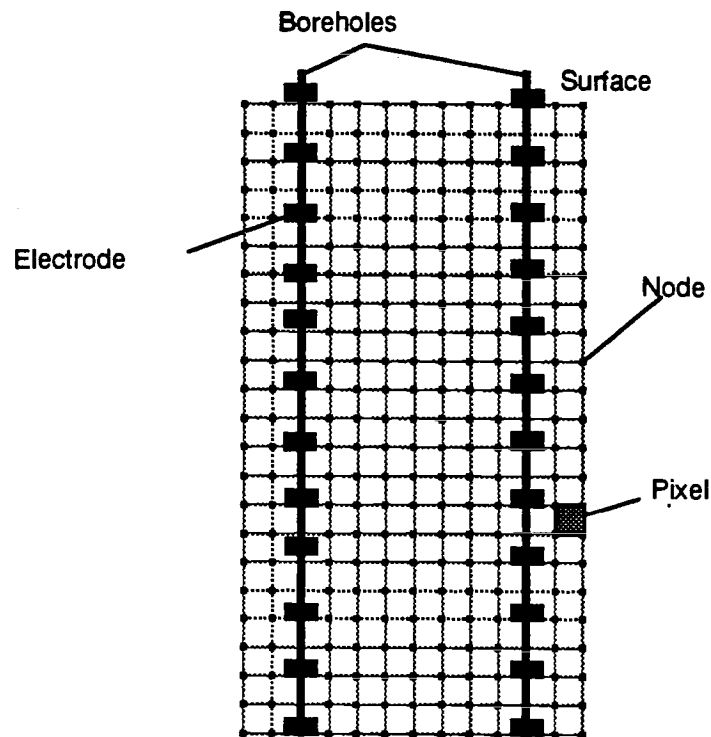


Figure 2.3. Foreground mesh.

Axially Symmetric Solution

For the Florence study, tomographic image planes were taken between well pairs arranged radially around the sparge well. The tomography reconstruction uses a forward solution of Poisson's equation to calculate the potential response of an axially symmetric earth from sources along the axis of symmetry.

The finite-element mesh used to model the reconstruction plane is shown in Figure 2.4. The entire mesh, including background regions, consists of 20 by 38 elements. The portion between the wells, the foreground, is 11 elements wide by 29 elements long. Flanking the foreground region on the right and bottom are four more elements, the same size as those in the foreground. The remaining elements expand out exponentially to complete the mesh of 20 by 38 elements. The foreground is the only portion of the mesh that is contoured to show resistivity distributions.

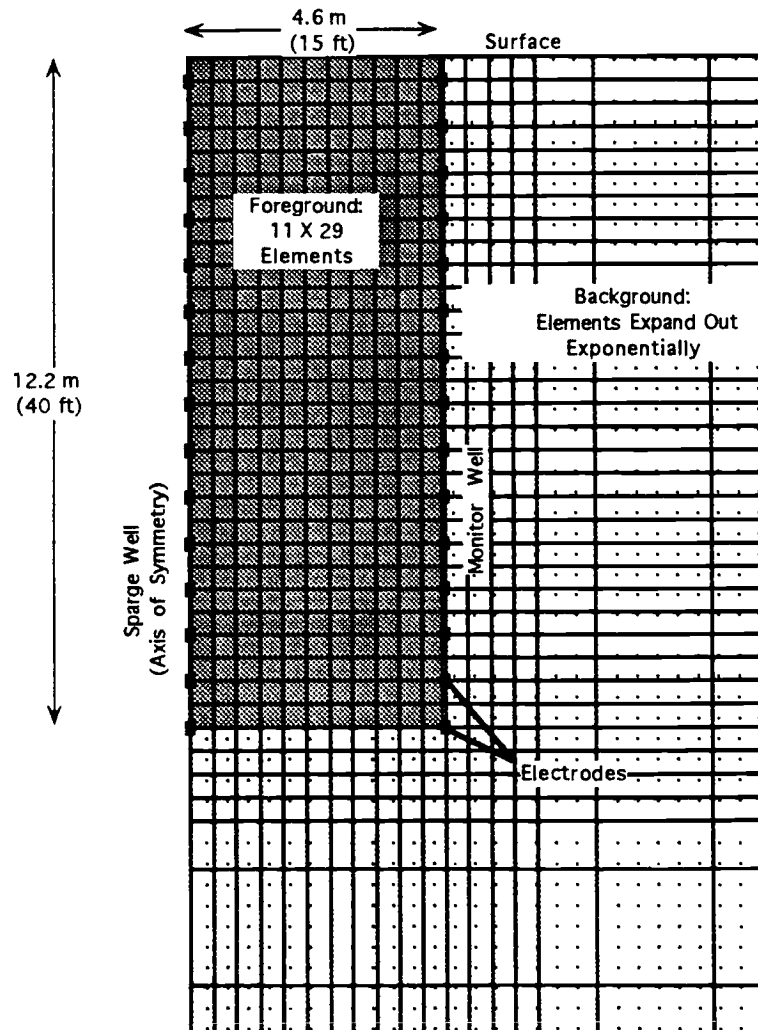


Figure 2.4. Finite element mesh design used to model axial symmetry around the Sparge Well.

Data Interpretation

During a typical data interpretation session, the raw data generated from the field measurements would be stripped of all header information and have appended onto it a new header, ready for input into the inversion program. After the inversion was run, the Chi-square value after the last iteration was expected to have leveled off below 500, which is close to the number of data points. Usually 5 iterations were necessary to achieve this requirement, but sometimes up to 10 iterations were needed to reach squared errors below 500. If the squared errors were still not below 500 even after 10 iterations in the inversion, the data would be examined more closely and "bad" data points would be removed before the next attempt at inversion. A data point was deemed "bad" if the ratio of the field and calculated resistivity values to the standard deviation was greater than a certain tolerance, usually 2 to 5. Those data points that were greater than the tolerance were removed from the data set and the inversion was reattempted. Such manipulation of the data is considered justifiable because realistically, there will be data points collected that are erroneous, due to interference or machine malfunctions, that need to be removed to obtain a true geoelectric interpretation.

Once a satisfactory inversion was obtained, the resistivity values for the area between boreholes were imported into the contouring package Spyglass Transform, where an image was generated and contoured.

CHAPTER 3

AVRA VALLEY, ARIZONA

Introduction

Contaminant plumes in the subsurface often reach groundwater aquifers that are used for human water supply after moving through the vadose zone. Structural characteristics as well as the hydraulic nature of the soil determine the path along which a contaminant plume will migrate. The transport and storage of contaminants in the vadose zone is therefore an important issue that must be understood for effective site remediation.

Current hydrological methods of detection cannot adequately track the complex nature of plume movement. A more useful and accurate method of tracking fluid flow is resistivity and induced polarization tomography. Resistivity tomography has been used in previous studies to reconstruct images of the vadose zone. However, the use of IP data in a tomographic array to image the subsurface is still under investigation. The study presented here attempts to explore the data that can be obtained through IP measurements, which is complimentary to information from resistivity image reconstruction.

Cross-borehole resistivity and IP surveys were carried out at the Avra Valley Geophysical Test Site to follow water flow in the unsaturated zone within a 30 m by 30 m sediment filled basin. The study used four collinear wells, 2 m apart, to monitor the flow of approximately 24,000 L of tap water injected from a line source. Data were collected beginning in late August, 1992, through January, 1993 on the three image planes between the four wells. Resistivity and IP distributions were reconstructed by a non-linear, two-dimensional inversion of a finite element forward

solution of Laplace's equation. The resistivity distributions are expected to delineate the wetting front, while the IP images should reveal information about the amount of salt present. I hope to show with this study that the combination of resistivity and IP can yield a unique image of both the fluid saturation and salinity.

Site Description

This field study was conducted at the Avra Valley Geophysical Test Site, an 800 m by 800 m area of land owned by The University of Arizona, shown in Figure 3.1. The test site is in the southern region of Avra Valley, about 32 km (20 miles) southwest of Tucson, Arizona. It is centered in the south half of Section 22, Township 15 South, Range 11 East. The average elevation of the area is 760 m (2500 ft) (Sternberg, 1993).

The land consists of low relief alluvium, dips gently to the north-northwest, and is crossed by various washes, subjecting it to frequent flooding. The site contains cactus and mesquite vegetation predominantly. The basement rocks consist of Precambrian granites, Paleozoic limestones, Mesozoic sandstones and conglomerates, and Cenozoic volcanic rocks. The upper unit (down to an estimated depth of 120 m) is Pliocene and Quaternary sediments, consisting of sand and gravel lenses of irregular thickness interbedded with silt and clay (Sternberg et al., 1991-1992).

Within the Avra Valley Geophysical Test Site, a lined basin was constructed in Cell D4 for purposes of a controlled injection of water into a volume of subsurface representing the vadose zone (Sternberg, 1993). It was this lined basin that housed the resistivity and IP tomography study carried out in this thesis. The basin, shown schematically in plan view and in cross section in Figures 3.2 and 3.3, respectively, measured 30 m by 30 m on each side, and extended to 5.9 m depth. Construction of

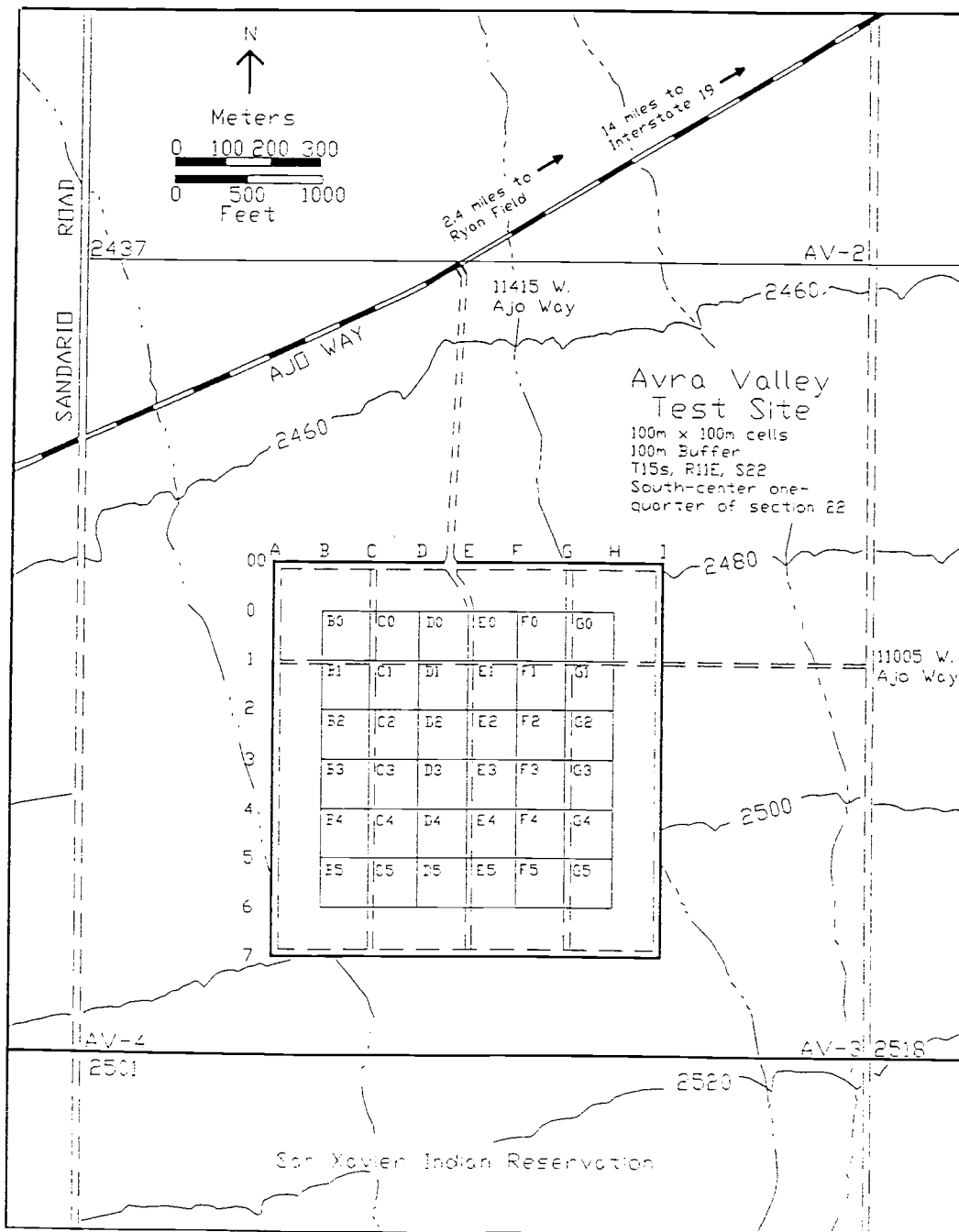


Figure 3.1. Map of Avra Valley Geophysical Test Site.

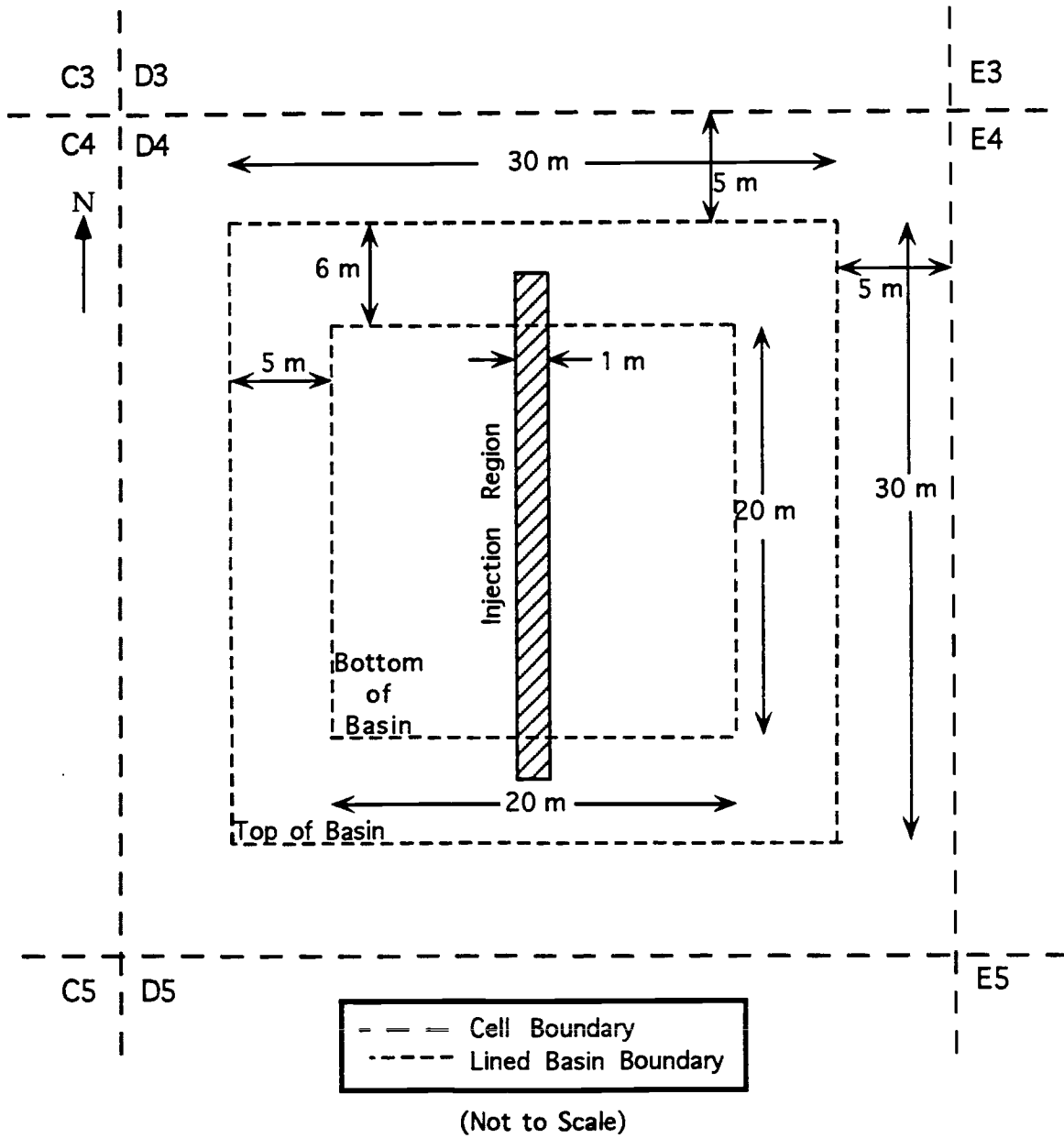


Figure 3.2. Plane view of lined basin.

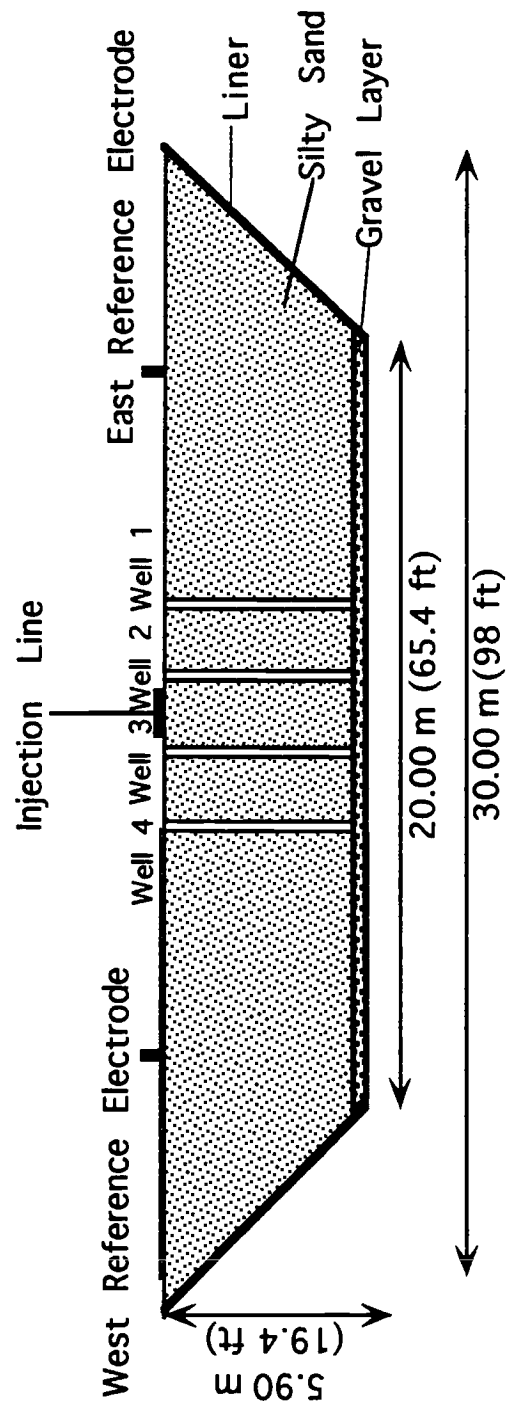


Figure 3.3. Cross-section of lined basin.

the basin occurred during the summer of 1992. During the excavation, sediments were removed to a berm on the south side of the proposed basin, the topmost sediments being removed first. The sides of the basin were sloped inwards from the top at a continuous dip of 45 degrees from the horizontal. The bottom area was thus 20 m by 20 m. After complete excavation of the basin, a thick, continuous plastic layer was placed down as the liner to contain the sediments. A layer of gravel, 0.3 m thick, was spread over the bottom. Sediments were then replaced into the basin, with the first sediments to be removed being the last to be transported back in. This system created a volume as near to homogeneous as possible while still retaining the nature of the sediments. The basin's surface area was covered with overlapping layers of clear plastic tarpaulin to protect the basin from rain.

Four wells were used in the DC resistance tomography surveys of this thesis, and twenty-five additional monitor wells were placed in the basin for well logging and other measurements. A more detailed plan view of the basin diagram is found in Figure 3.4 showing the placement of 25 monitor wells and the four wells used in the tomography surveys. Each of the wells extend to a depth of 5.1 m.

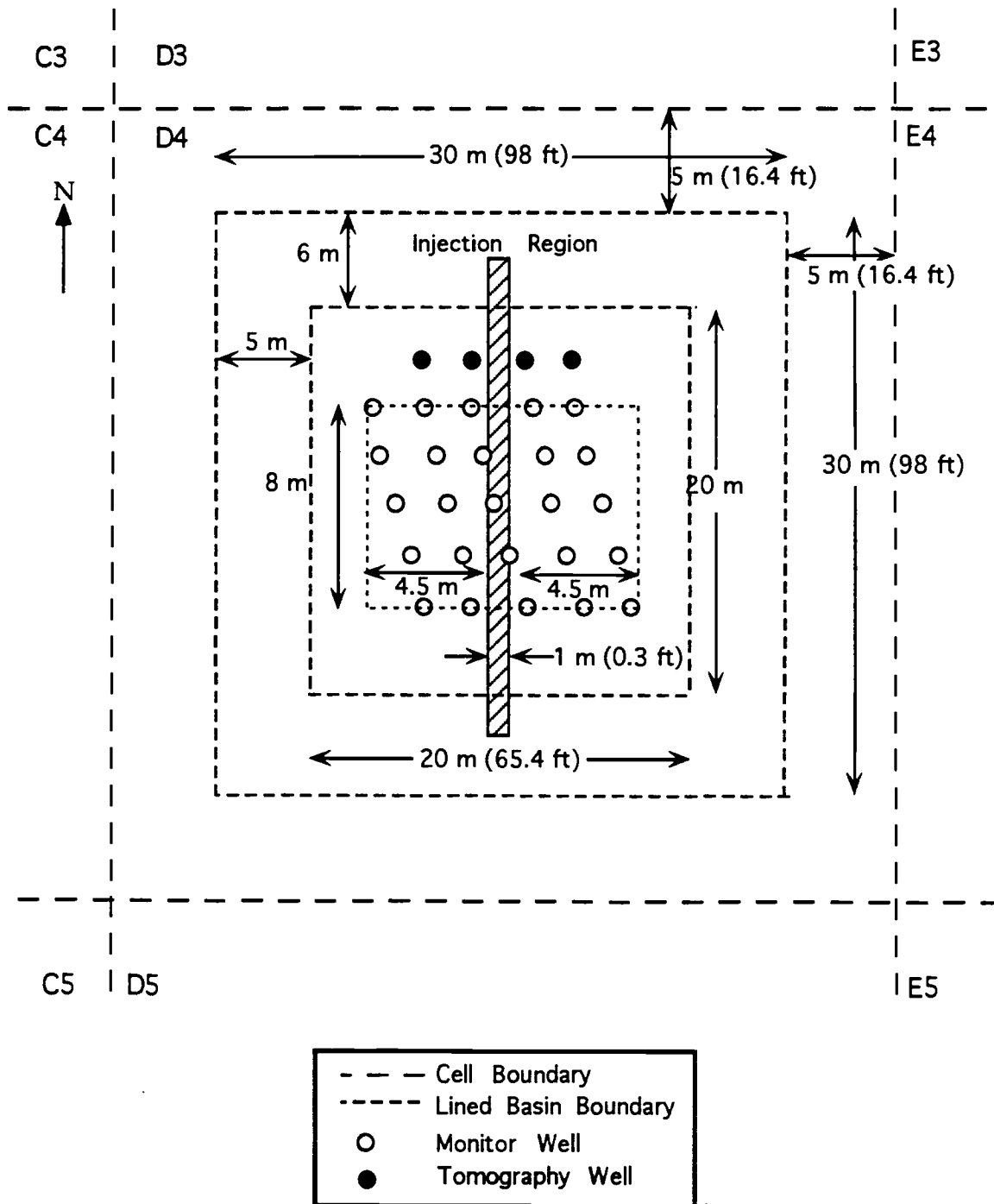


Figure 3.4. Plan view of lined basin showing all wells.

Purpose

The purpose of the study conducted at Avra Valley was to explore the capabilities of resistivity and IP tomography for tracking the movement of water in the vadose zone. The study was considered an initial field trial of the automated data acquisition system developed by the faculty and students at LASI, the Laboratory for Advanced Subsurface Imaging. The investigation was preliminary, considering the data acquisition system was being used for the first time in the field since its construction, and the lined basin was still in its infancy stage. Results from the experiment were expected to delineate the wetting front and track its migration downwards and outwards.

Dissolved solids found in water increase bulk conductivity, thereby reducing bulk earth resistivity (Stollar, 1975). Using the inverse proportionality that relates conductivity to resistivity, the areas saturated by water would be expected to have anomalously low resistivity values in the tomographic image. IP could perhaps determine the amount of total dissolved solids (TDS) in the injected water by decreasing where the TDS level is high and increasing where the TDS level is low. When the TDS level is high, such as in a highly saline solution, the dissolved solids would force current to be carried by free ions in solution rather than cation exchange within the clays of the soil, resulting in a decrease in IP. Likewise, IP increases in a solution with much less TDS because the cation exchange within the clays is now greater.

Data Acquisition

Field Measurements

For the resistivity and IP surveys, four borehole wells were placed collinearly within the lined basin at a separation of 2 m. Each well had a 4 in (10.16 cm)

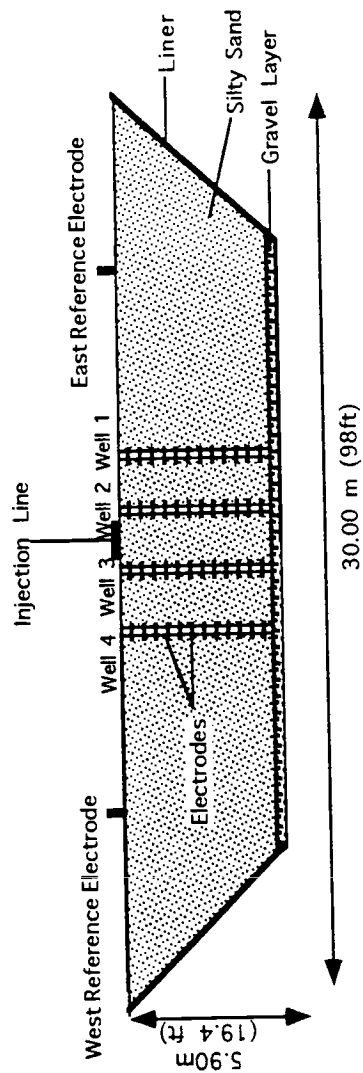


Figure 3.5. Cross-section of lined basin showing wells and electrodes.

diameter and contained twelve equally spaced electrodes from the surface to the gravel layer at 5.1 m depth. Two reference electrodes for a pole-pole configuration were buried just below the surface along the same line as the four wells, and in opposite directions, each 9 m from the center of the wells. The four wells are assumed to be vertical. Figure 3.5 shows a cross-sectional view of the basin with the four wells and electrodes.

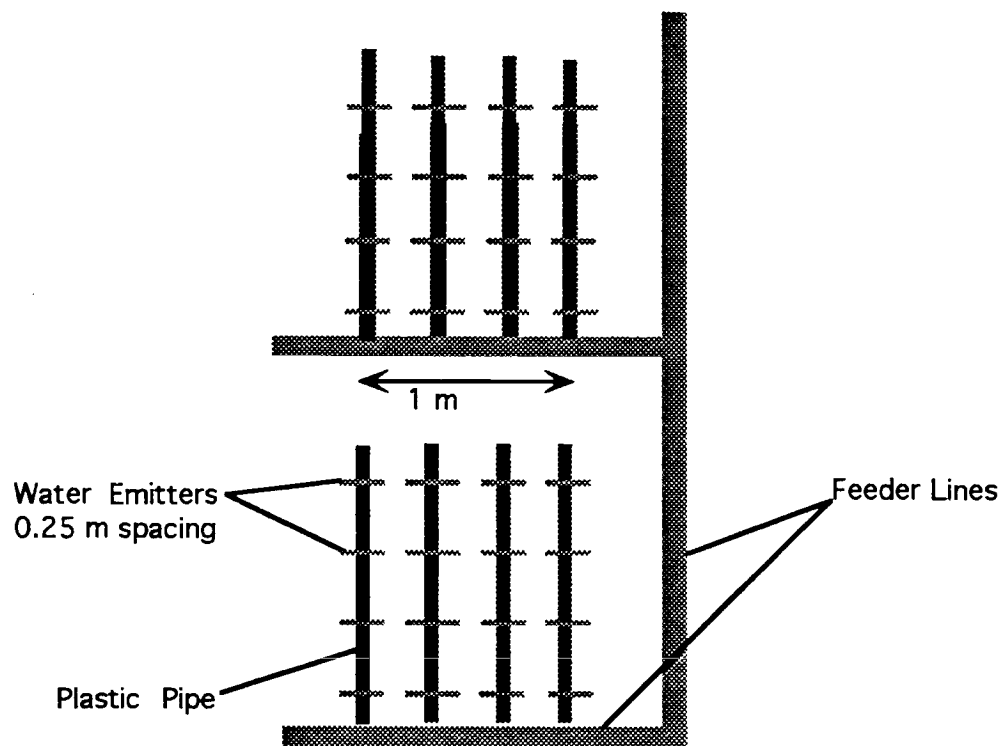


Figure 3.6. Detail of water emitters in line source injection.

An injection system was designed to provide a constant flux of water per unit area over a zone 1 m wide by 25 m long. Four plastic pipes, 24 m long each and 0.25 m apart, were placed on the surface of the basin, parallel to each other and perpendicular to the four boreholes. Figure 3.6 shows the water injection system in detail. Water emitters were located at intervals of 0.25 m along each plastic pipe.

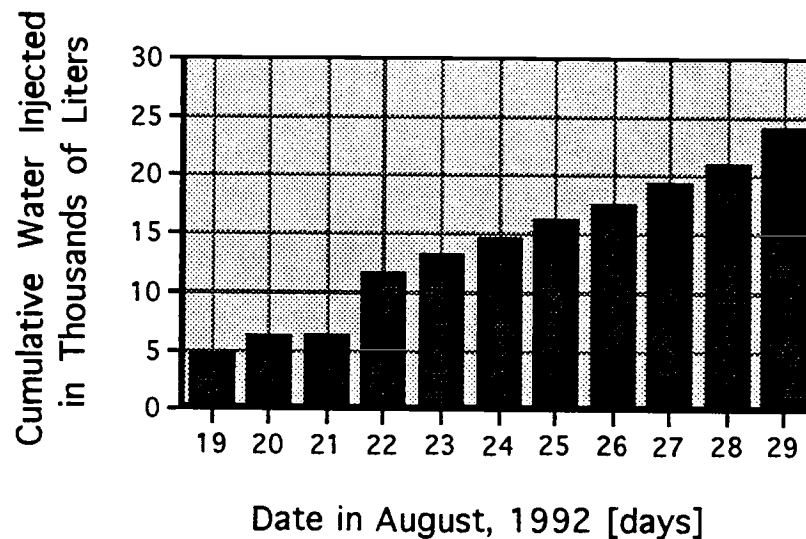


Table 3.1. Graph of cumulative water injection for lined basin experiment.

Tucson tap water was injected beginning August 19, 1992, with the pumping of 1220 gal (4617.70 l) in 12 hrs. Injection continued at an average rate 500 gal/day (1892.50 l/day), reaching a total of nearly 6385 gal (24167.23 l) on August 29, 1992. The schedule of water injection is shown graphically in Table 3.1.

To acquire data, a combination of on-time DC resistance and IP measurement sets were made. Each set of data consists of three planes of data, which are the two-

dimensional areas between adjacent boreholes. To collect a plane of data, an electrode in one well and a reference electrode transmit a known current of approximately 0.5 Amps to a receiving electrode in the other well, which measures the resulting voltage difference. This process is then repeated for other electrodes in the wells to obtain measurements between as many linearly independent combinations of electrodes as possible. The collection of an entire data plane, which included measurements between adjacent wells and within the same well, lasted about 45 min.

A background set of measurements was taken August 17 and 18, 1992, before the injection of water. Measurements that were taken during the injection were later deemed unusable, as the equipment had not been functioning properly at the time. Post-injection measurements were taken on September 15, 1992, and again on January 28, 1993.

In-Lab Rock Properties Measurements

Rock properties measurements were carried out as part of these studies. The purpose of these measurements was to study resistivity and chargeability as functions of pore water salinity using rock property models discussed in CHAPTER 2 of this thesis. A combination of resistivity and IP methods were used to conduct the measurements on the unconsolidated sediments that fill the lined basin. Experimentation was carried out on the Avra Valley sediments using three different levels of logarithmically increasing water salinity levels. The three solutions used were as follows: Tucson tap water (sampled from water injected at the site) with approximately 2 g/l total dissolved solids (T.D.S.); a solution with about 10 times the tap water salinity; and a solution with about 100 times the tap water salinity. These solutions were all made by adding the necessary amount of salt to tap water.

The sediment used was collected from a berm on the southern border of the lined basin at a depth of approximately 10 cm from the surface, on November 9, 1992. This sediment from the berm is the same unconsolidated sediment used in filling the basin.

At each salinity level, a blank was measured using only the solution without sediments. Then, unconsolidated sediments were packed into the sample holder and saturated by forcing solution in from one end. Once saturated, a current of 0.8 Amps was passed through the two inner current electrodes and received by the outer metal mesh electrodes. The resistance and IP measurements were made using a 100 ms delay time, 200 ms window time, and 1, 2, 4, and 8 windows. A total of three samples of the same sediments were measured for repeatability.

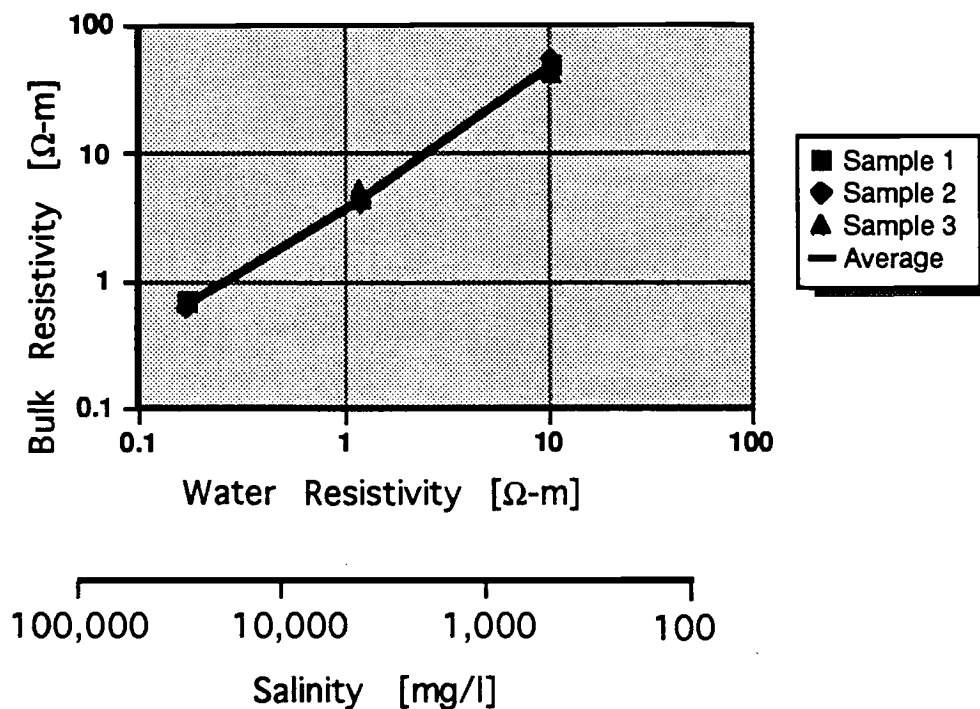


Table 3.2. Graph of bulk, or soil, resistivity Vs pore water resistivity and salinity.

The Bulk Resistivity Vs Water Resistivity and Salinity graph, Table 3.2 shows an increase in sediment resistivity with decreasing salinity consistently for the three samples. These data are in agreement with the expected results that the saturated sample would become more resistive as the water saturating it contains less ions in the form of salt to facilitate electrical conduction. In general, the resistivity of a rock depends on the resistivity of the fluid in its pores.

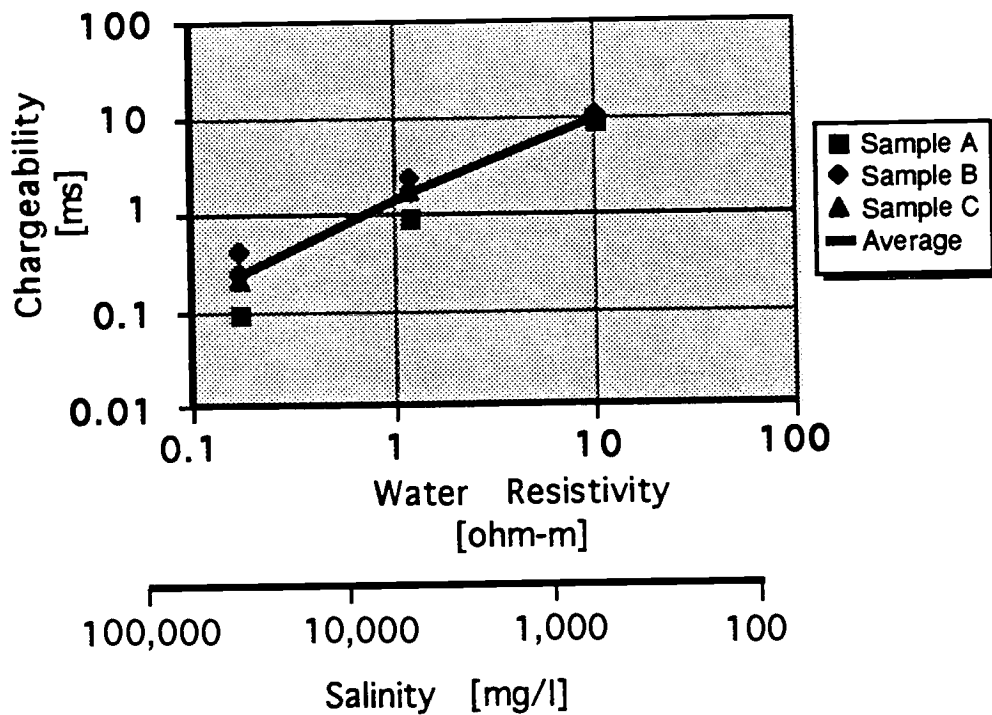


Table 3.3. Graph of chargeability Vs pore water resistivity and salinity.

The Chargeability Vs Water Resistivity and Salinity graph, Table 3.3, shows an increase in chargeability with decreasing salinity for the three samples. The increase in chargeability is likely due to current being carried through exchangeable cations within the clays of the sediment at the lowest salinity. At the high salinity level, the current is more likely carried by free ions in solution, shown by a decreased chargeability. Similar behavior is seen in the chargeability data for the cross-borehole tomography field measurements.

The results from these rock properties measurements were then compared with the Waxman-Smits model for predicting bulk resistivity based on pore water resistivity. First, a Waxman-Smits family of curves was plotted in Table 4.1, for saturations of 20%, 50%, and 100% using a pore water resistivity range of 0.125 Ω -m to 5 Ω -m and a Q value of 0.04 equivalents/l.

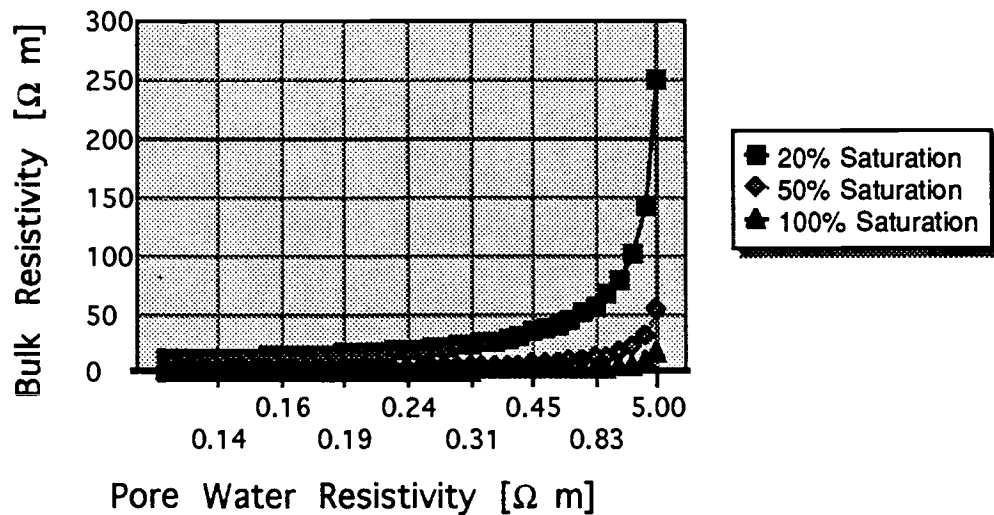


Table 3.4. Graph of bulk resistivities determined by the Waxman-Smits equation for 20%, 50%, and 100% water saturation Vs pore water resistivity.

The samples used in the laboratory analysis were assumed to be 100% saturated. The three different salinity levels used to saturate the samples (tap water, 10 times the salinity of tap water, and 100 times the salinity of tap water) were translated into conductivities and were used as pore water conductivity values in the Waxman-Smits equation. The resulting bulk conductivities predicted from the Waxman-Smits model were converted into resistivities and are graphed in Table 3.5 with the sediment resistivities that were obtained from laboratory analysis. The relation seen between the predicted and the actual resistivities is close, indicating a good choice of assumptions for the Waxman-Smits model and validity of the model in general.

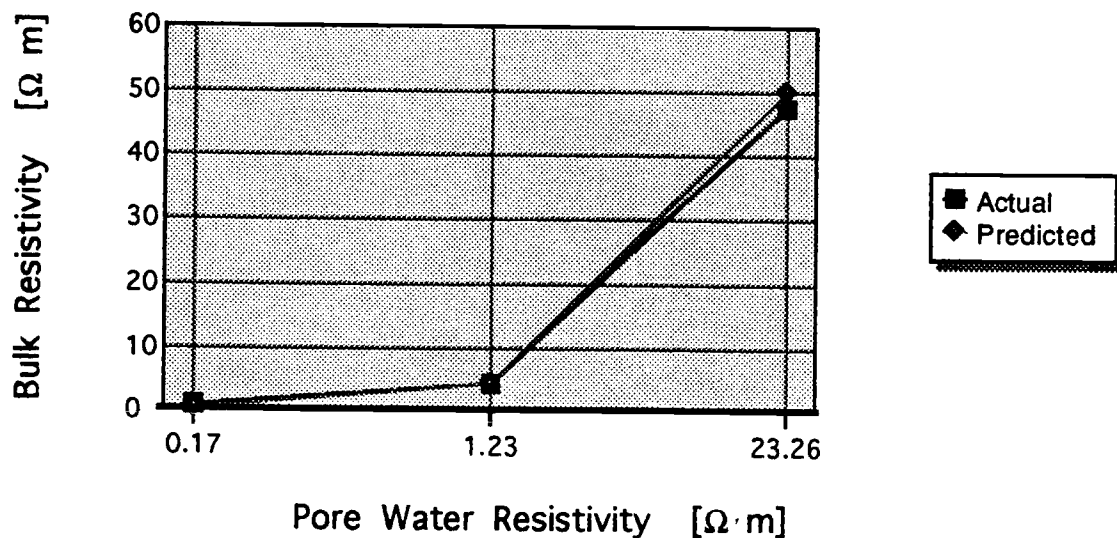


Table 3.5. Graph of bulk resistivities determined from actual laboratory measurements and predicted by the Waxman-Smits equation Vs pore water resistivity.

Expected Results

Rock Properties Measurements

The in-lab rock properties measurements show that the resistivity of the soil, when saturated with the water to be injected (tap water), should be approximately 40 Ω -m to 60 Ω -m, shown in Table 3.2. As the salinity of the water saturating the sample increases (as more salt is added), the bulk resistivity of the soil decreases, down to less than 1 Ω -m when the salinity is increased 100 times. Based on these results, I would expect to see soil resistivities in the 40 Ω -m to 60 Ω -m range where the tap water is saturating the soil with unaltered salinity. Accordingly, I would expect to see lower soil resistivities, around 20 Ω -m to 40 Ω -m, where the injected water has acquired salt from the surrounding soil, thereby increasing its salinity and decreasing the bulk resistivity of the soil.

These in-lab rock properties measurements also indicate that the chargeability of the soil saturated with tap water should be around 10 ms (Table 3.3). As the salinity of the injected water increases, the chargeability decreases, down to about 0.2 ms when the salinity is increased 100 times. I would therefore expect the IP values to be around 10 ms in the areas saturated by the injected tap water with its original salinity. Where the salinity of the injected water has increased due to the presence of dissolved salts from the soil, I would expect the soil chargeability to decrease to a range of 5 ms to 10 ms.

EM39 Logs

During the injection experiment at the Avra Valley Geophysical Test Site, the 25 monitor wells in the basin shown in Figure 3.4, separate from the four wells used in

the resistivity surveys, were logged before, during, and after injection with EM39 logs (Sternberg, 1993).

A Geonics EM39 induction probe was used to measure the resistivity of the surrounding rock. The instrument operates at a frequency of 39.2 KHz and has a coil separation of 50 cm. A total of 96 EM39 logs were taken from July 30 to September 26, 1992. The resulting sections generated from measurements taken on August 17, September 5, and September 26, 1992, will be presented in this thesis for comparison with tomography data. These measurements were taken on dates closest to the dates that tomography data were collected in August and September. No EM39 data were collected in January. The resulting images generated from these measurements are shown as contoured cross-sections of apparent resistivity where all of the 25 wells surveyed are projected onto one line, shown in Figure 3.7. A complete background EM39 resistivity section taken August 17, 1992 is shown in Figure 3.8. A complete post-injection EM39 resistivity section taken on September 5, 1992 is shown in Figure 3.9. Finally, a partial post-injection EM39 resistivity section is shown in Figure 3.10.

Based on the EM39 data of Figure 3.9, background resistivities are expected to range from less than 25 Ω -m to greater than 60 Ω -m.

The post-injection resistivity section from September 5, 1992 of Figure 3.9 indicates that 7 days after the last injection of water, the wetting front, the region of low (20 Ω -m to 30 Ω -m) resistivities has descended about 3 m.

Twenty-eight days after the last injection of water, September 26, the resistivity section of Figure 3.10 indicates that the region of low resistivities, the wetting front, has not descended much more from September 5. The bottom edge of the wetting front still appears to be around 3 m depth.

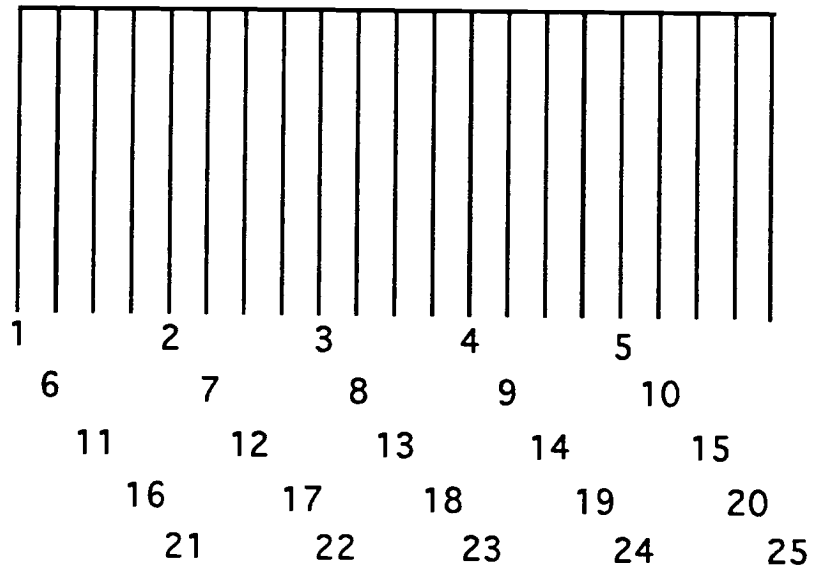


Figure 3.7 Monitor wells shown projected onto one line.

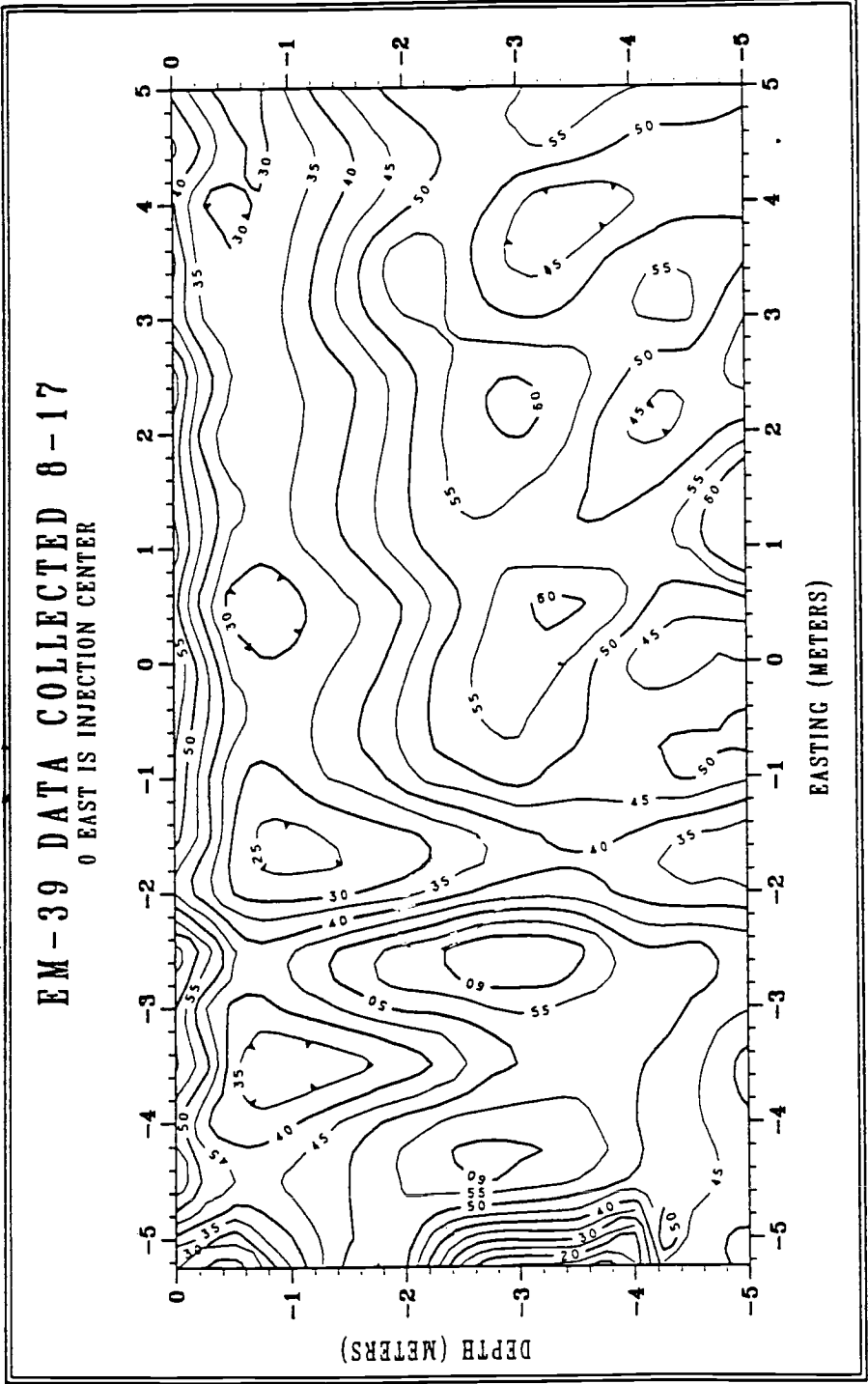


Figure 3.8. EM39 survey from August 17, 1992. Resistivity in Ω -m.

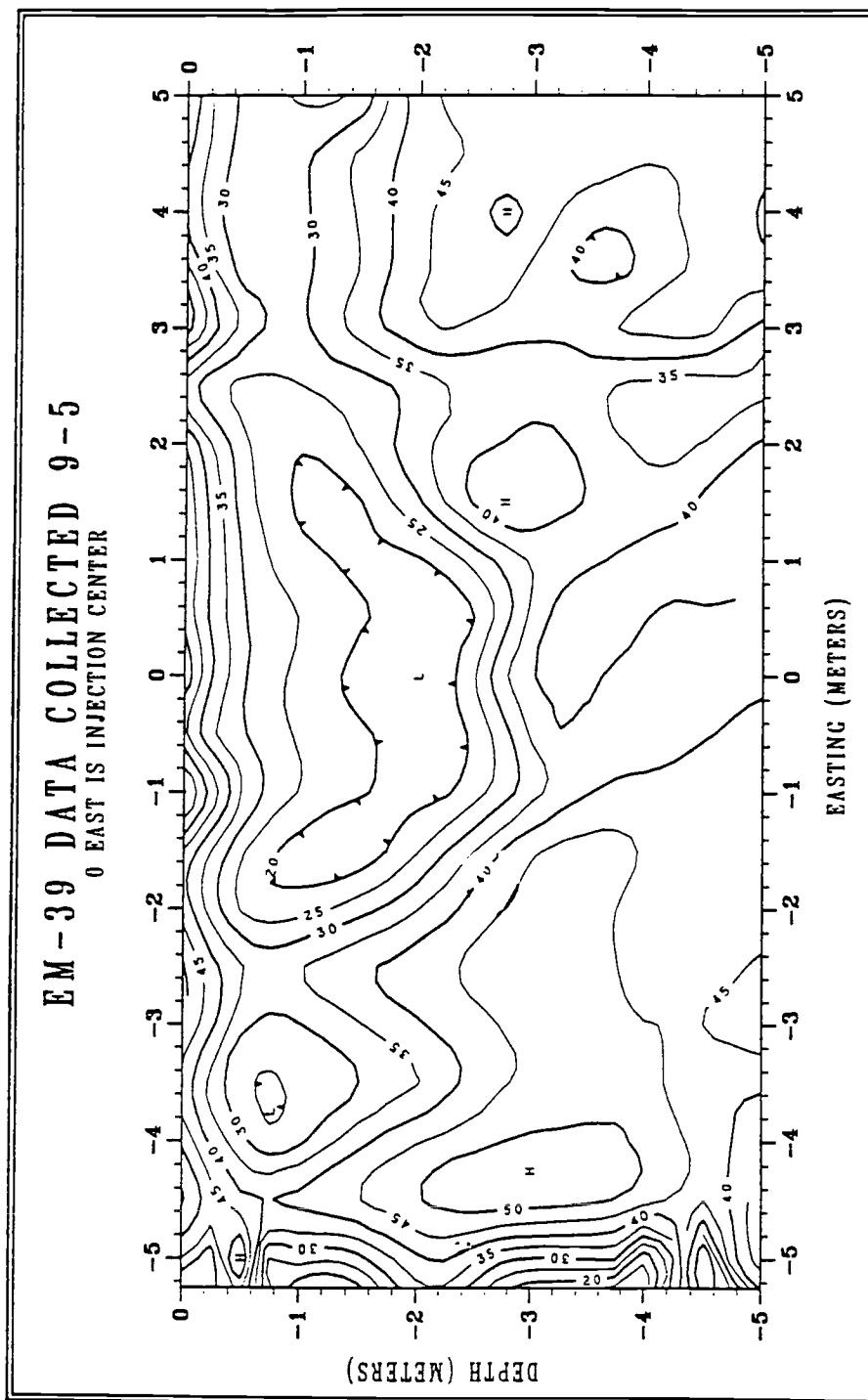


Figure 3.9. EM39 survey from September 5, 1992. Resistivity in Ω -m.

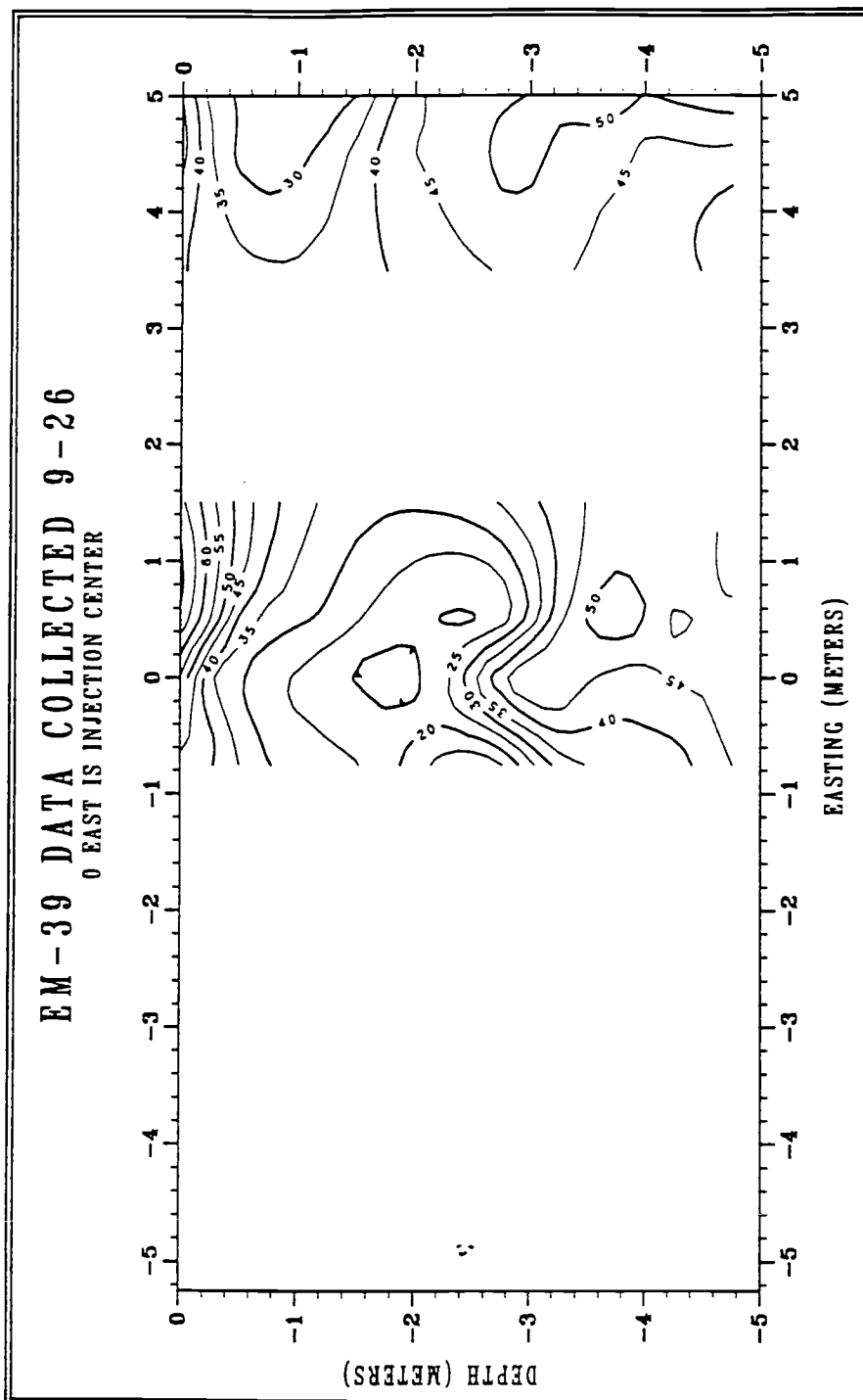


Figure 3.10. EM39 survey from September 26, 1992. Resistivity in Ω -m.

Results

Resistivity and IP image planes were generated between the four boreholes both before the injection, as background, and after the injection. The background measurements were taken August 17 and 18, 1992, and subsequent post-injection measurements were taken September 15, 1992 and January 28, 1993. In both the resistivity and IP images, there is slight vertical exaggeration, as each square pixel within borehole boundaries represents an actual area of 0.25 m in width, but only 0.23 m in depth.

Resistivity Reconstructions

Examining first the background resistivity tomography image in Figure 3.11, the subsurface between the four wells has a range in resistivity values from 20 Ω -m to 200 Ω -m. This image shows a range of resistivity values from 20 Ω -m to 40 Ω -m from the surface to about 1 m depth. This low resistivity range is likely due to the high moisture content of the soil near the surface due to water trapped below the clear plastic tarpaulin on the surface. There is a resistive layer (50 Ω -m to 100 Ω -m) in Well 1 between 1 m and 2.5 m depth that thickens and dips downward toward Well 4.

Generally, resistivity increases with depth. High resistivities reflect the low water saturation of the sediments in the vadose zone. The low resistivity area in the first 1 m depth of the image reflects the near-surface portion of the vadose zone that was partially saturated due to retention of moisture below the overlapping layers of plastic tarpaulin on the surface of the basin.

The existence of deeper layers could be the result of differences in soil compaction or loss of pore water. Sediments were replaced back into the basin by dumping soil from the northeast corner of the basin with bulldozers and heavy machinery, spreading soil throughout the basin. Due to the manner in which

sediments were refilled, from the northeast corner and spread outwards, layers are shallower at the northeast end of the basin, nearest Well 1, and deepest farther away from the point of entry of the sediments near Well 4.

The discontinuities of the contour lines near the wells are likely the results of borehole effects. Borehole effects are the erratic variations in resistivities seen immediately surrounding the borehole, caused by local resistivity changes at the electrode contacts and crosstalk between electrodes. The anomalously high resistivity area of about $200 \Omega\text{-m}$ at 4.75 m depth near Well 4 might be attributed to these same effects from Well 4.

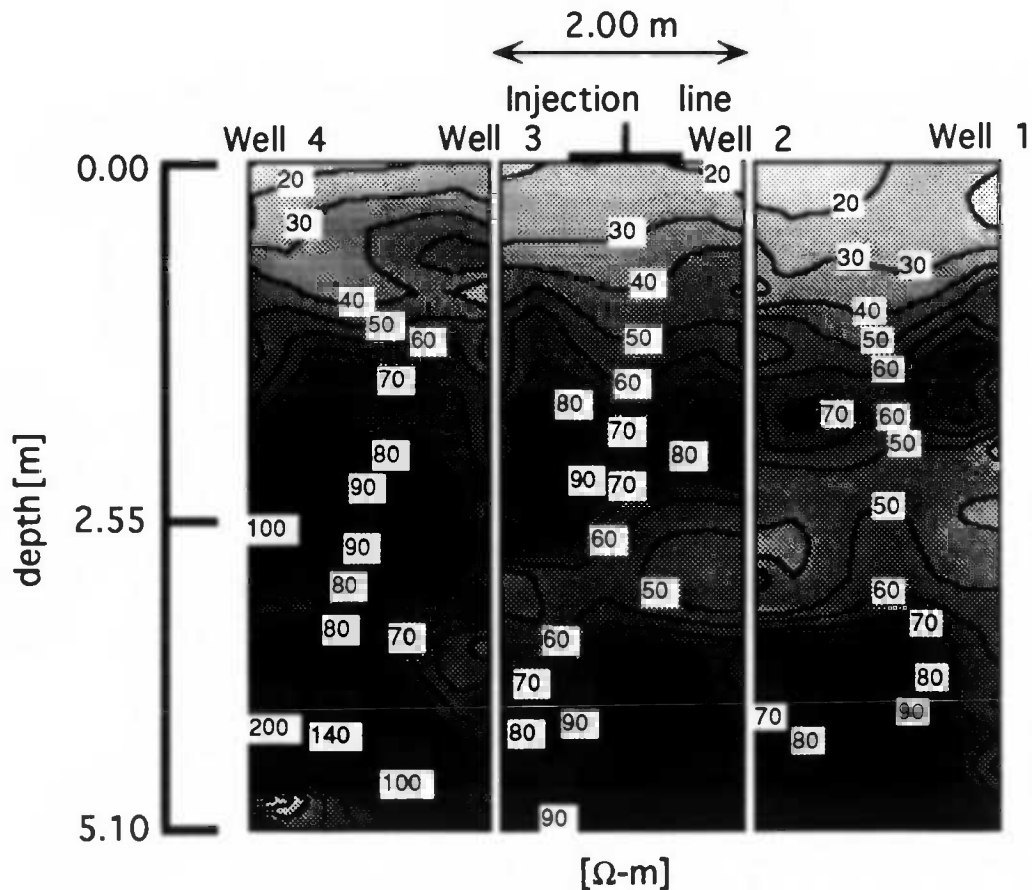


Figure 3.11. Background resistivity reconstruction, August 17 and 18, 1992.

In the post-injection resistivity tomography image from September 15, 1992, Figure 3.12, there is a dramatic change in the resistivity as compared to the pre-injection background. An area of low resistivity, $10 \Omega\text{-m}$ to $40 \Omega\text{-m}$, is seen at about 1 m depth near Well 1 and Well 4, and plunging down to about 3 m depth between Wells 2 and 3. Below this area, the resistivity values increase between $50 \Omega\text{-m}$ and $80 \Omega\text{-m}$, similar to the background values at this depth.

The zone of low resistivities starting at the surface and extending to 3 m depth in the center of the image appears to delineate the wetting front due to the infiltration of water. The injection lines runs perpendicularly between Wells 2 and 3, as shown in Figure 3.4. Water from this line source likely percolated in a downward direction

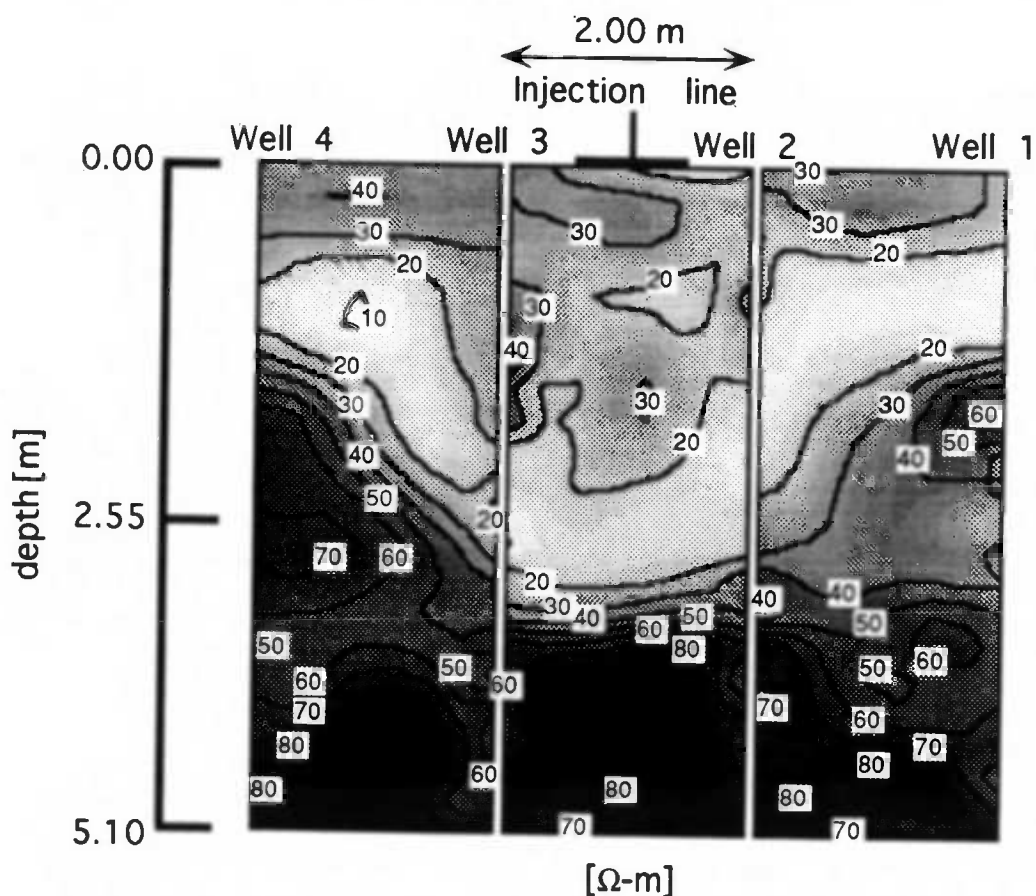


Figure 3.12. Post-injection resistivity reconstruction, September 15, 1992.

predominantly, with some lateral spreading. Accordingly, this now saturated area is more conductive/ less resistive. Based on the results of the pre- and post-injection images, the water had infiltrated the soil to about 3 m depth between Wells 2 and 3 by September 15, two weeks after injection was complete.

The post-injection image from January 28, 1993, Figure 3.13, shows the progress of the wetting front about five months after injection. The front has descended to a maximum depth of about 4 m, but has still not reached the bottom of the basin at 5.1 m.

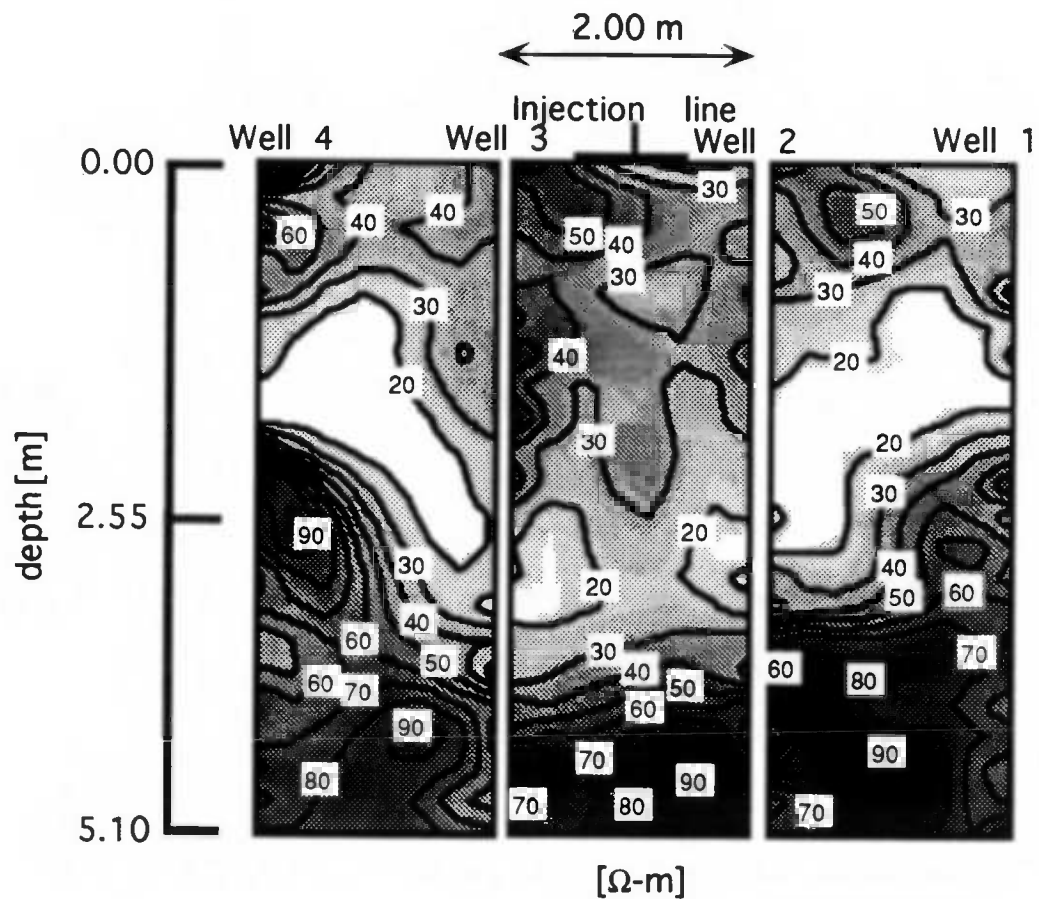


Figure 3.13. Post-injection resistivity reconstruction, January 28, 1993.

Percent Difference Images

The percent difference image for resistivity from September 15, 1992, Figure 3.14, illustrates the observed difference in resistivity values from pre- to post-injection. The percentage values were obtained using the formula

$$100 * \frac{(\text{post-injection resistivity} - \text{pre-injection resistivity})}{\text{pre-injection resistivity}}$$

Near the surface, to about 1 m depth, the percent difference values fluctuate but tend toward the low side, indicating a small difference between the background and post-injection data at this depth. This reflects the partial saturation already occurring in the pre-injection setting due to meteoric waters, comparable to the induced partial saturation resulting from the injection. The wetting front delineated by the resistivity image is reinforced in the percent difference image. The differences between the pre- and post-injection data within the wetting front are great due to the saturation from the water infiltration that was not present in the background. Below the wetting front, the percent differences are low, as the saturation level of the soil at these depths is virtually the same from pre- to post-injection.

The percent difference image from January 28, 1993, Figure 3.15, indicates that the wetting front has descended nearly to the bottom of the basin between Well 2 and Well 3. Near the top of the image, a layer of high percent differences represents the evaporation of water close to the surface.

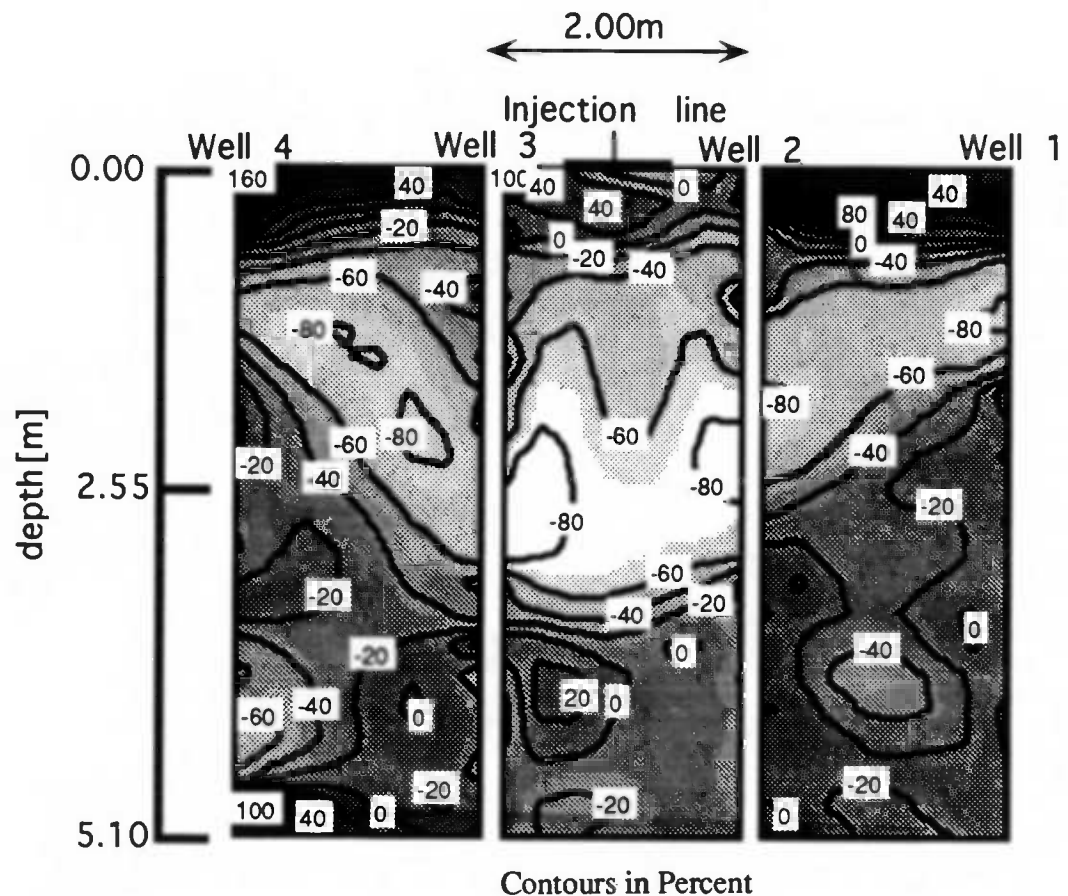


Figure 3.14. Percent difference of resistivity reconstruction, September 15, 1992.

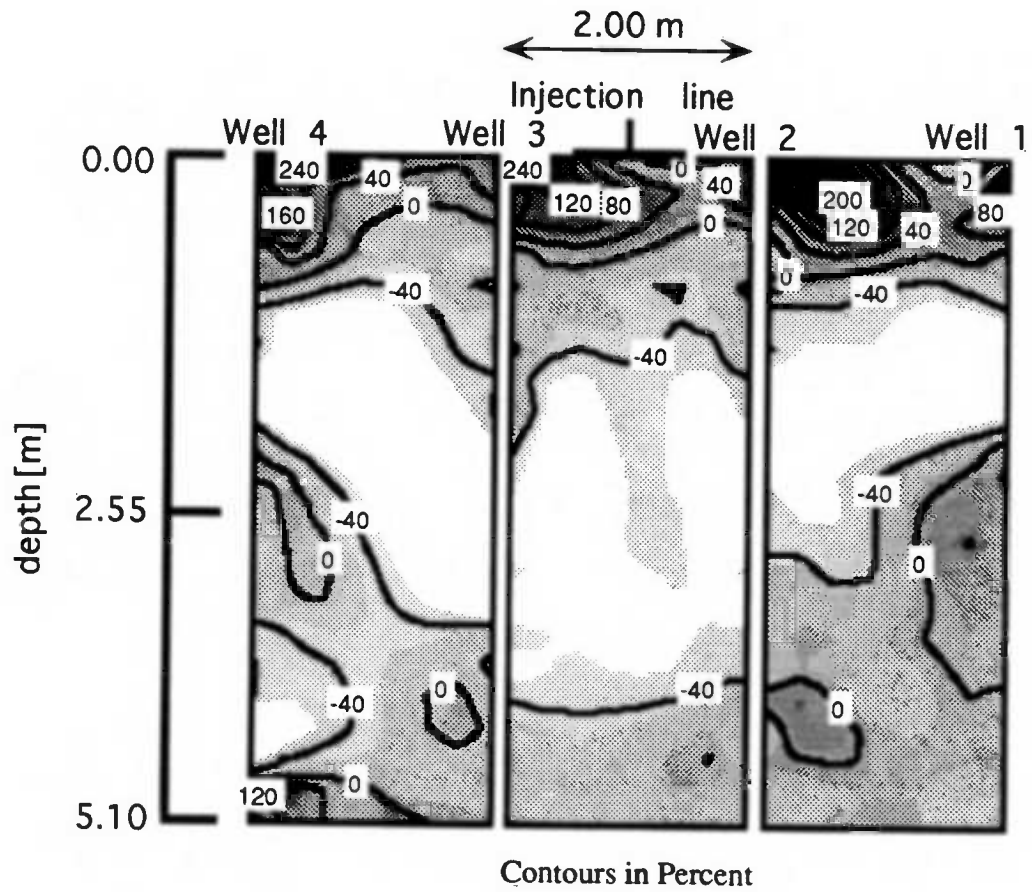


Figure 3.15. Percent difference of resistivity reconstruction, January 28, 1993.

Induced Polarization

IP in this study was measured as chargeability. The background IP image planes, Figure 3.16, illustrate the uniformity of chargeability of the unsaturated zone. Chargeability values range from 1 mV/V to 3 mV/V, with most values near 1 mV/V. A small area of 3 mV/V chargeability occurs in the upper right corner of the section, near Well 1, reflecting the higher moisture content of the soil near the surface. The uniformly low values of chargeability throughout the rest of the section indicate a homogeneously unsaturated zone. In both pre- and post-injection IP images, the noise estimations chosen for the inversions could have been slightly high. This has been shown to produce overly smooth images (LaBrecque et al., 1992).

After injection, the chargeability images, Figure 3.17, take on a dramatically new look. Higher chargeability values exist in the areas delineated as the zone of saturation from the resistivity images. Chargeabilities begin at high values near the surface (8 mV/V), and gradually decrease to low values at the edge of the wetting front. Below the front, the chargeabilities once again assume the background values near 1 mV/V.

The area of high chargeability appears to sit on top of the area of low resistivity from Figure 3.12. High chargeabilities near the top of this area probably reflect the flushing of salts out of the soil by the infiltrating water. At the surface, chargeabilities approach those of the lab results for tap water in saturated sediments (Table 3.3). At depth, chargeabilities gradually decrease as the zone nears the edge of the wetting front, where infiltrated water has possibly ponded and is still saline. Thus, while the resistivity image from post-injection clearly resolves the edge of the wetting front, the chargeability image appears to delineate the levels of salinities occurring in the section.

The IP image from January 28, 1993, Figure 3.18, reinforces the correspondence between the IP and resistivity tomographic images. Chargeability is high in the areas where salts have been flushed from the soil, and low at the edge of the wetting front, now down to about 4 m depth. From the surface, the chargeability values begin at about 9 mV/V, increase to a wide band of 10 mV/V, and then gradually decrease to 2 mV/V as depth increases. The wide band of 10 mV/V chargeabilities possibly reflects the leaching of salt from the soil in this area. Slightly lower chargeabilities exist above this band possibly where salts have been replaced by rain water that moistens the surface. Chargeabilities gradually decrease below this band where water from the injection still remains ponded in the subsurface, bearing salts.

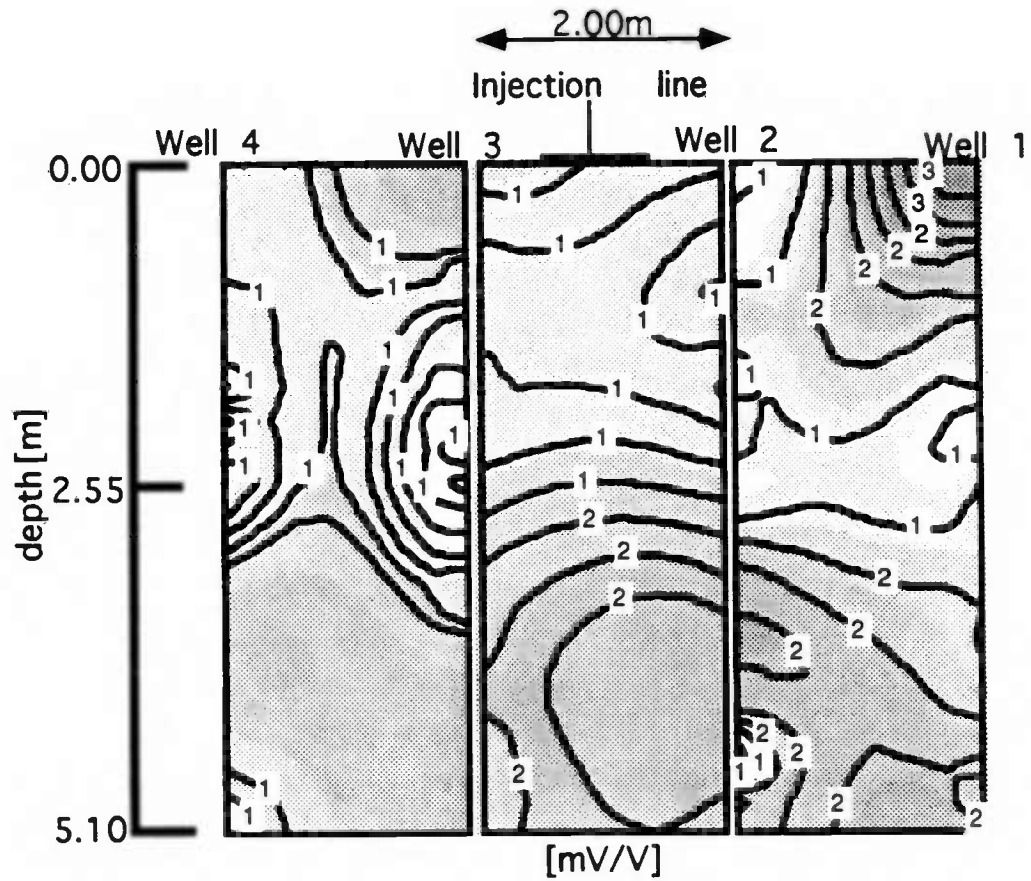


Figure 3.16. Background IP reconstruction, August 17 and 18, 1992.

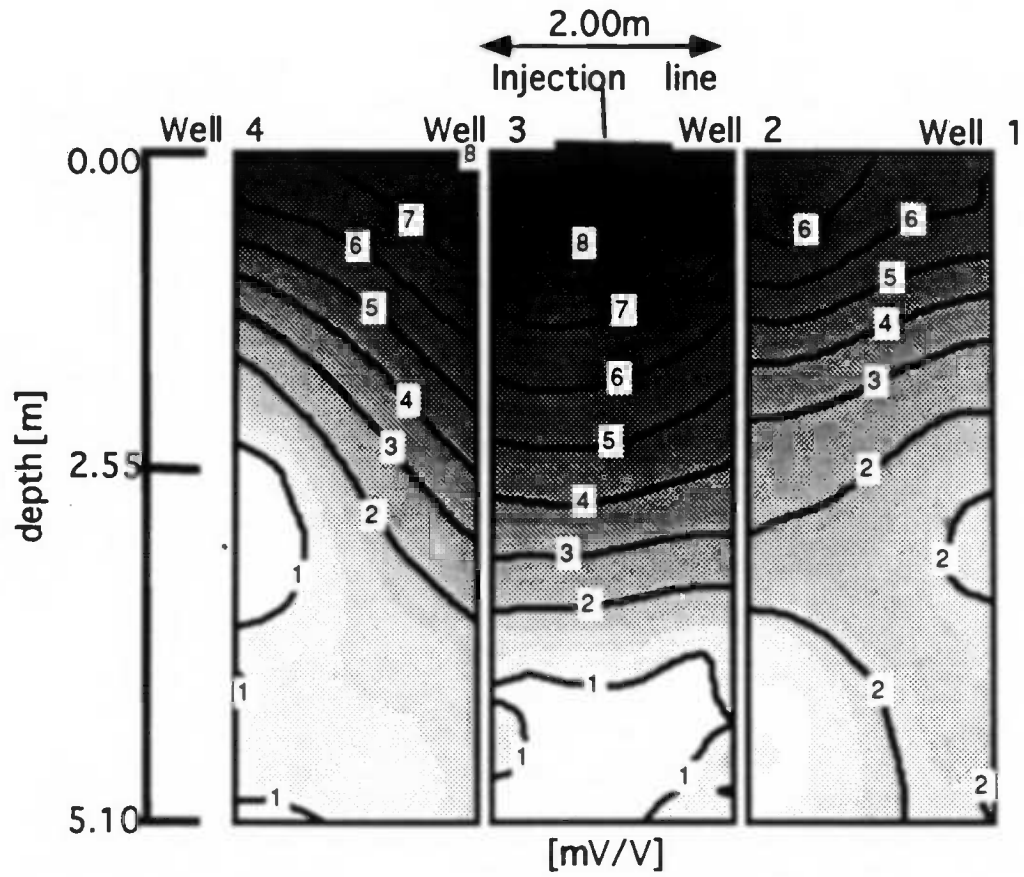


Figure 3.17. Post-injection IP reconstruction, September 15, 1992.

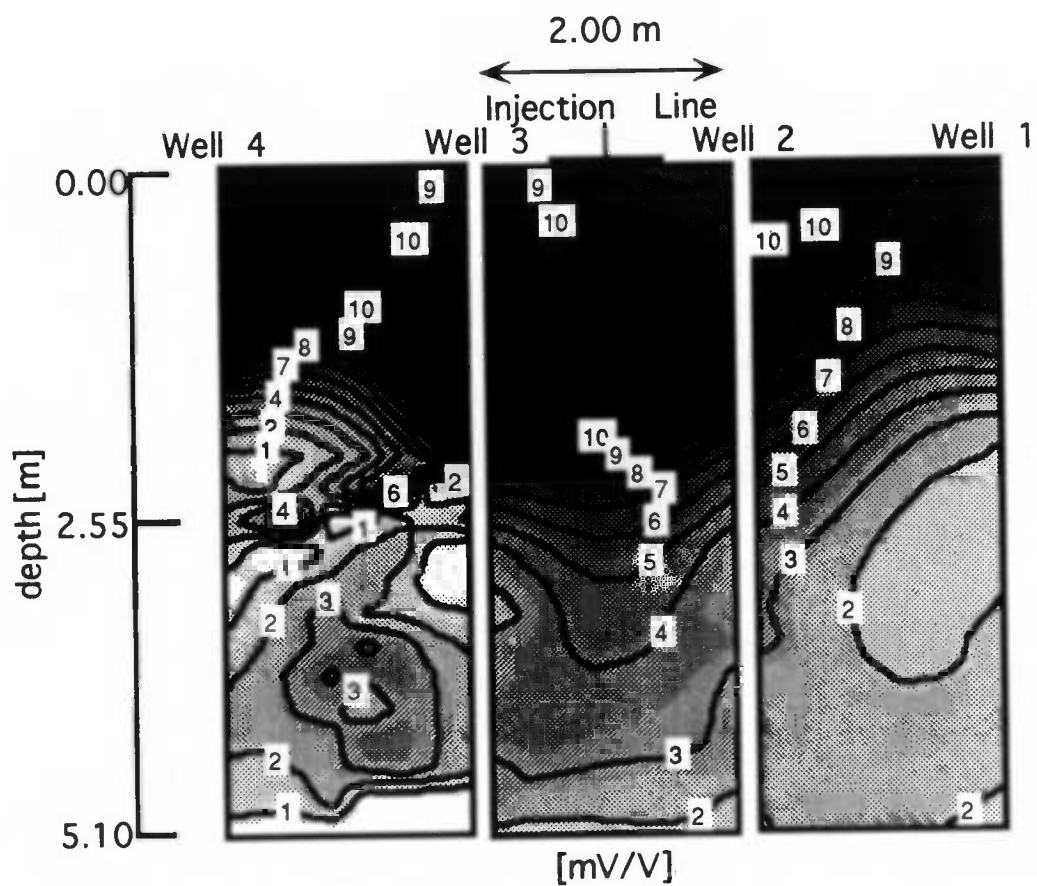


Figure 3.18. Post-injection IP reconstruction, January 28, 1992.

Conclusions

The findings from this study support the expected results for resistivity and IP tomography. The results of the resistivity images from pre- to post-injection illustrate the ability of resistivity tomography to clearly resolve the boundaries of the wetting front produced by the line source injection. IP images, on the other hand, are better suited to indicating the salinity levels encountered in the infiltrated areas. The results from this study indicate to me that resistivity tomography is a useful technique for defining areas saturated by the injected water, and IP tomography is also an effective technique for revealing the salinity levels of a saturated zone.

Hydrologic models of water injection from a line or point source have predicted a flow pattern in a tear-drop shape from the point of injection. However, given the hydrologically complex nature of the field scale site in Avra Valley, the results from this study propose a somewhat different scenario. In this study, water is shown to substantially infiltrate the vadose zone not only in the downward direction, but also laterally. Therefore, I have concluded that resistivity and IP tomography is an effective technique for delineating water flow patterns where hydrologic models fall short.

CHAPTER 4
FLORENCE, OREGON

Introduction

Air sparging is a relatively new technique for the remediation of ground water contaminated with volatile organics, such as petroleum hydrocarbons. In this technique, clean, compressed air is injected below the water table via a well. As the air rises through the contaminated soil, hydrocarbons partition into the vapor. The contaminant-bearing air is then removed by a vapor extraction well. This process is depicted in Figure 4.1.

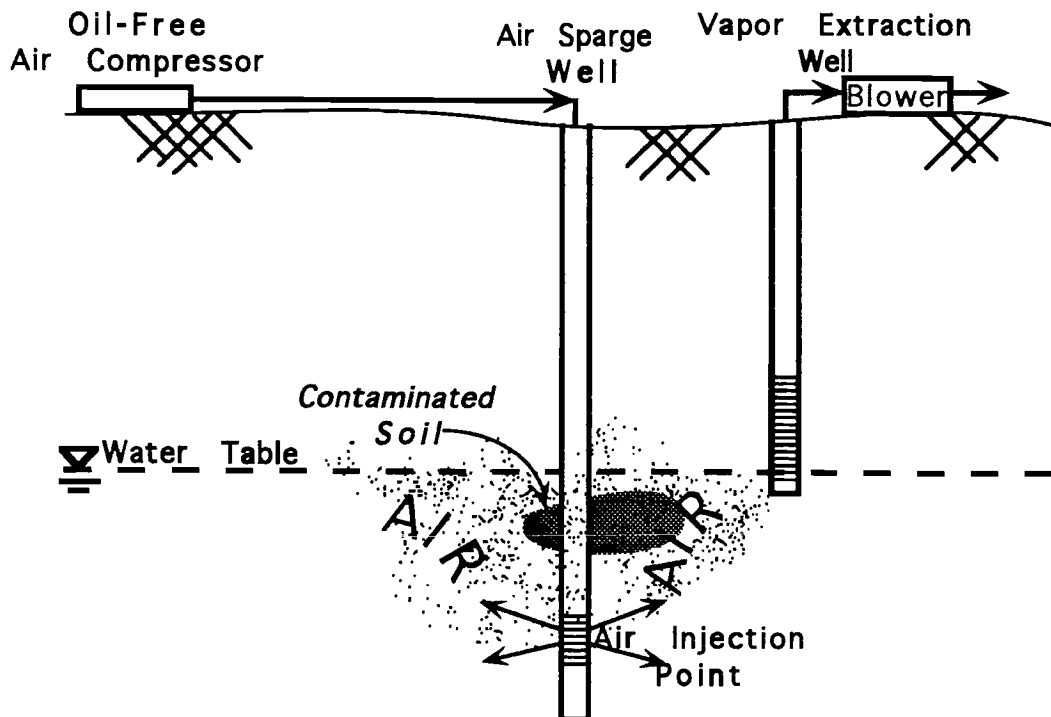


Figure 4.1. The process of air sparging.

While air sparging has recently been the focus of laboratory experiments (Ji et al., 1993) and computer simulations, (Lundegard and Anderson, 1993), little direct field data exists on the distribution of the air injected beneath the surface. There are two current theories describing the flow of air during sparging. One states the air becomes channeled on its way through the saturated zone (Ji et al., 1993), and the second describes air traveling as discrete bubbles (Nyer, 1993). A clear understanding of the mode of travel of the air as well as the size and geometry of the region of air flow is essential for improving air sparging technology.

Cross-borehole resistivity surveys were carried out in an attempt to gain such an understanding at an air sparging site in Florence, Oregon in July 1993. The resistivity measurements were made using six 40 ft (12.19 m) deep wells, one of which was the air sparge (air injection) well. Data were collected over a two week period during and after several sparge events. Tomographic resistivity reconstructions were generated between wells using an algorithm that assumes axially symmetric structures.

The movement of air throughout time is clearly defined by high resistivity regions. During the early sparge times, is narrower near the well screen, about 3 ft (0.91 m), and widens up towards the water table, where it is about 9 ft (2.74 m) in radius. Long after sparging is discontinued, a residue of entrained air remains in the saturated zone, as indicated by a zone of 60% to 80% saturation.

Site Description

Florence, Oregon is between the Coast Range and the Pacific Ocean on the northern bank of the Siuslaw River, shown in Figure 4.2. The study site is a former UNOCAL service station located along Highway 101, approximately 1000 ft (304.79 m) west of Munsel Creek which discharges into the Siuslaw River, 2500 ft (761.96 m) south of the site. The Siuslaw River discharges into the Pacific Ocean, about 4 mi

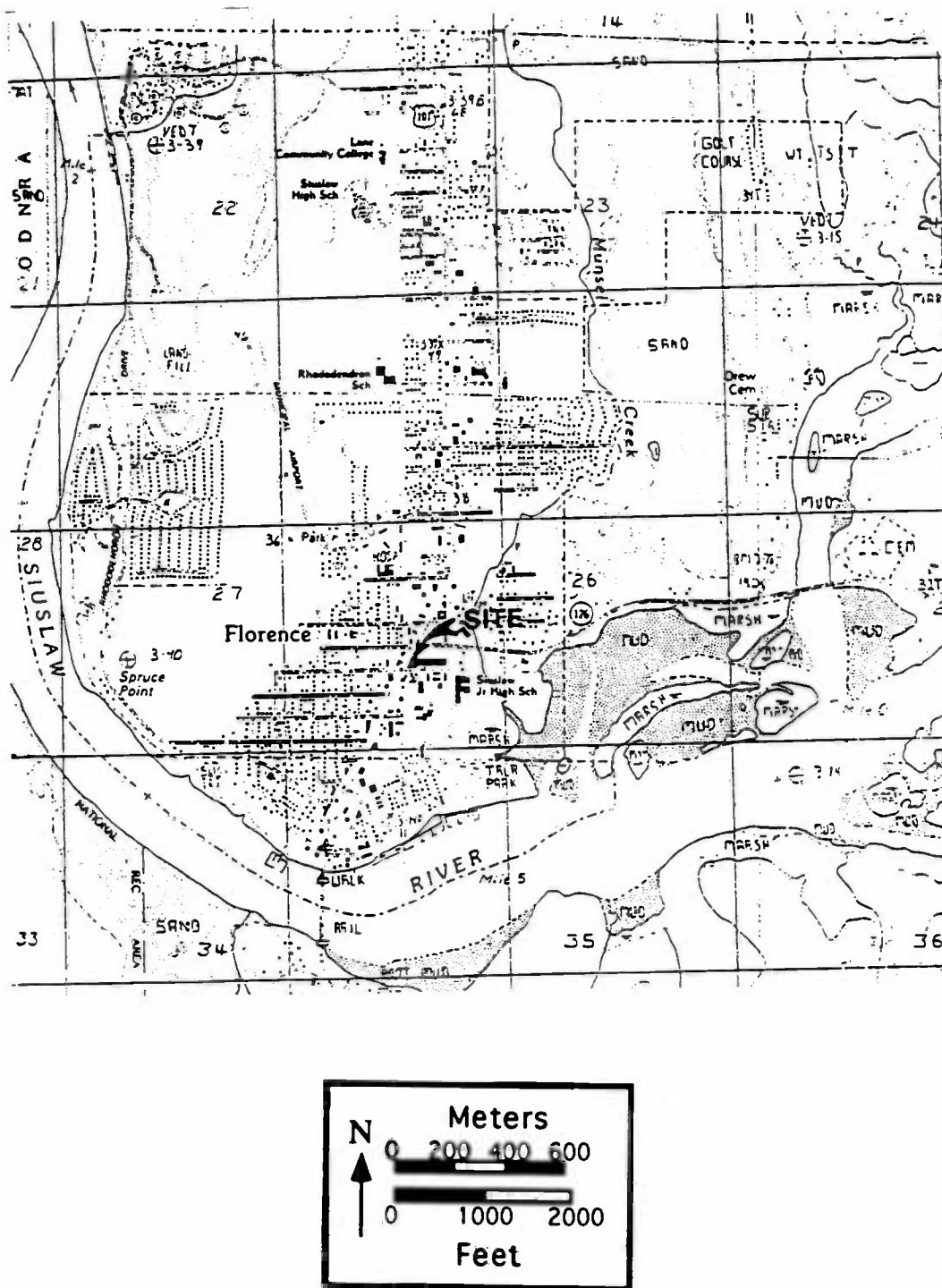


Figure 4.2. Map view of field site in Florence, Oregon.

(6.44 km) northwest of the site. The site is bounded on the east by the eastern boundary of Section 27, Township 18 South, Range 12 West, Willamette Meridian. The site is at an average elevation of 30 ft (9.1 m) above mean sea level.

The Florence area is underlain by Quaternary Age, unconsolidated dune sand, occurring in thicknesses from 100 ft to 200 ft (30.48 m to 60.96 m). The dune sand is likely underlain by Tertiary Age Tyee formation, a sandstone. The surficial fill which extends to a maximum depth of 2.5 ft (0.76 m) consists of sand with gravel, or gravelly sand. The area's low, undulating surface slopes upward from the ocean to the base of the Coast Range. The climate is temperate marine, with an average annual precipitation of 65 in (165.10 cm), 75% of which falls during the autumn and winter seasons.

In Florence, groundwater occurs in the native dune sand at shallow depths and flows southerly, toward the Siuslaw River. The water table is encountered between depths of 17 ft (5.18 m) and 22 ft (6.71 m), with seasonal fluctuations of 2 ft to 2.5 ft (0.61 m to 0.76 m). The groundwater is potable and supplies water for the city. The porosity of the dune sand varies between 36% and 40%, while permeability ranges from 270 to 600 gallons/day/foot² (0.02 cm/s average). The subsurface in this area appears to be free of any low permeability layers in the study zone that would prevent the effective operation of the air sparging technique or vacuum extraction.

The former service station is registered with the Oregon Department of Environmental Quality as an underground storage tank facility. Records show that the property was occupied by service station facilities since 1966 or earlier. Underground storage tanks (UST's) were used for various petroleum products and wastes. The service station was dismantled, and all remaining UST's and product lines were removed in 1990. Subsurface characterization surveys revealed the presence of petroleum hydrocarbons in the soil and ground water from locations on the site. Most

of the contaminated soil was remediated by biotreatment mounds, although ground water contaminated by gasoline had been found in one monitoring well along the southern property boundary. Figure 4.3 shows a plan view of the former service station, indicating locations of previous UST's.

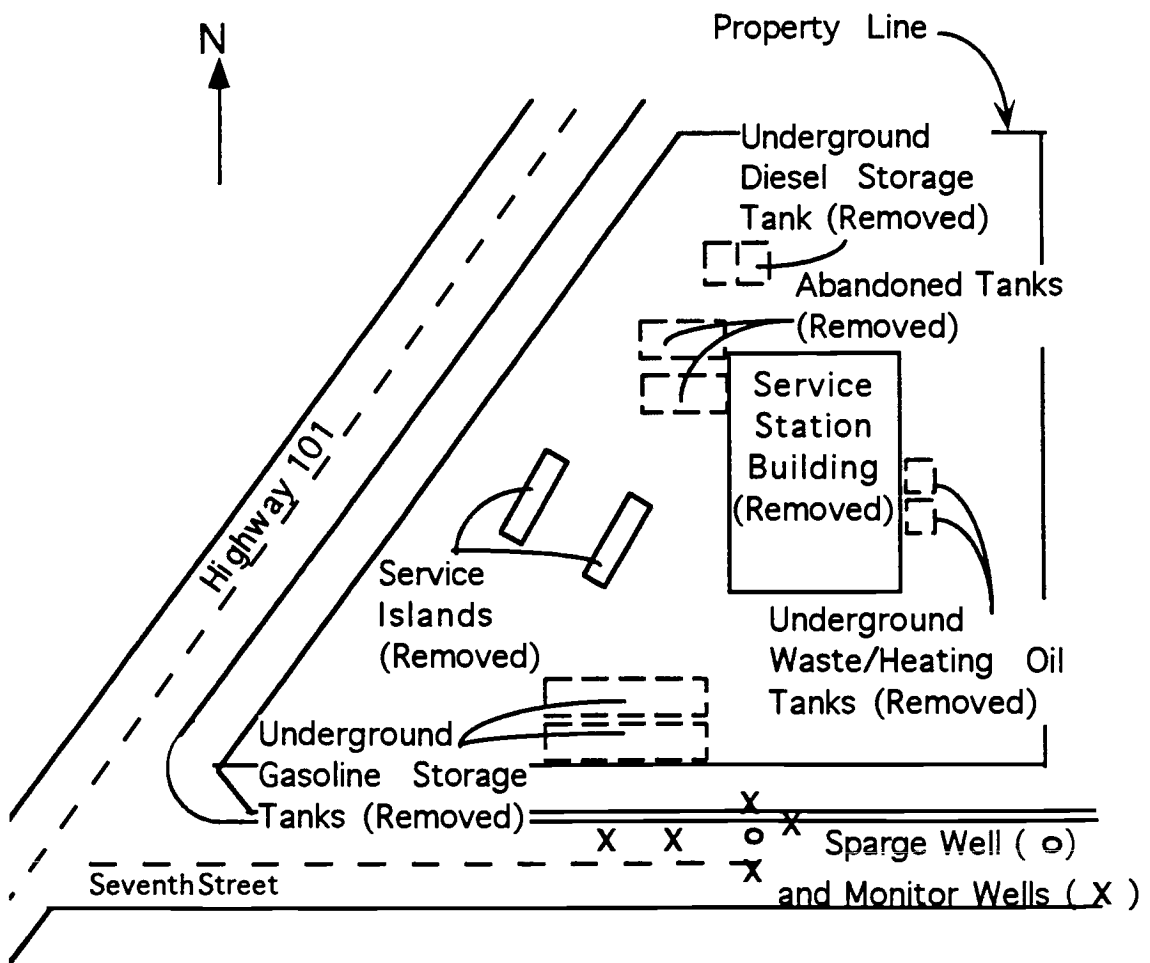


Figure 4.3. Plan view of field site in Florence, Oregon.

Purpose

Cross-borehole measurements were made at the air sparge site in an attempt to better understand the process of air sparging. The purpose of the study was to provide two and three dimensional images of air distribution within the subsurface resulting from air sparging, to correlate anomalies in the subsurface with the injection of air, to track the air flow through time, and to determine what if any lasting effects to the subsurface occur as a result of sparging.

For broader applications, this study was meant to provide information on air sparging on a field scale. Up until this time, almost all studies to monitor air sparging were in-lab experiments or computer simulations. This study was among the first to generate real data from a site. The results from the study will supply needed information on the behavior of the air to improve this technology for future remediation efforts.

Data Acquisition

Field Measurements

Cross-borehole resistivity surveys were carried out at the contamination site from July 13 through July 22, 1993. The study encompassed background measurements, several sparge events originating from two different wells (the Sparge Well and Well 3), the vacuum extraction process, and data after sparging had ceased.

To obtain two-dimensional images of the air sparging process, two boreholes were used: the air sparging well itself and an adjacent well. A radial array of wells around the air sparging well was used to obtain a three-dimensional picture of the process. This would help determine whether or not the air followed a symmetric path around the point of injection.

For the survey, six wells were equipped with electrodes at the site around and including the well used for air sparging. A plan view of the well locations is shown in Figure 4.4.

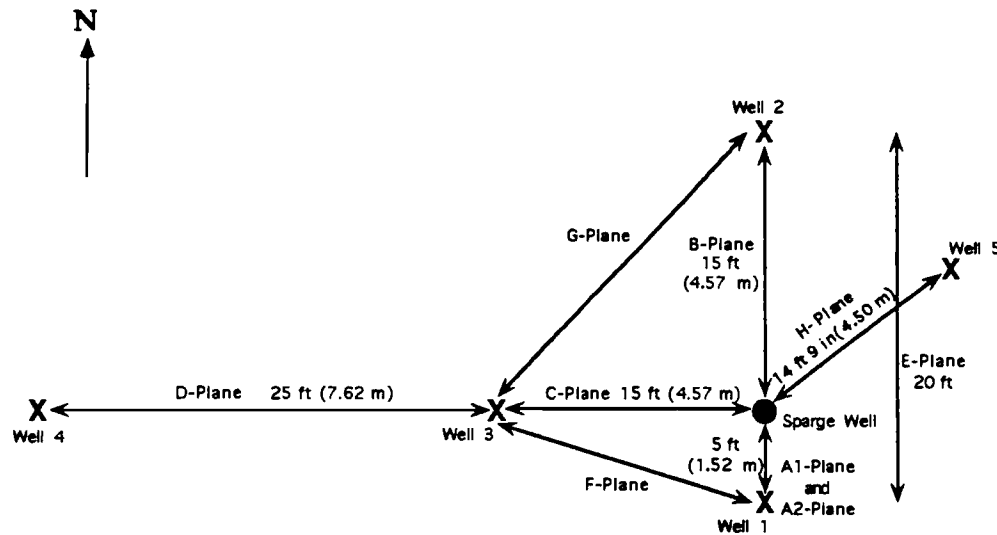


Figure 4.4. Plan view of well locations in Florence, Oregon.

Each well was equipped with 15 or 20 electrodes. The Sparge Well and Well 1 were equipped each with 20 electrodes on the outside of the casing, 15 of which were spaced at equal intervals of approximately 2.67 ft (0.81 m), and 5 of which were placed in between the electrodes near the point of air injection. Well 2, Well 3, and Well 4 each contained 15 electrodes spaced evenly at approximately 2.67 ft intervals. The Sparge Well and Wells 1 through 4 all extended to depths between 41 ft (12.50 m) and 42 ft (12.80 m) below the surface. Well 5 was a 25.5 m deep vacuum extraction well already present at the site that was temporarily equipped with 7 electrodes inside the well casing at equal spaces of 16 in (0.41 m). Three additional

electrodes were buried at the surface in a line extending out from the top of Well 5, completing a total of 10 electrodes for Well 5.

The monitoring Wells 1 through 5 were drilled with an 8 in (20.32 cm) stem hollow auger, and the Sparge Well was drilled with a 12 in cable tool. The casings were made of 2 in (5.08 cm) Schedule 40 PVC. A mixture of Portland cement and 2% bentonite grout was used as an annular sealant around the casing along its entire length, except for the short filter pack at the injection point in the Sparge Well. Each well was topped with a steel surface monument and a concrete seal.

In-lab rock properties measurements were made on the cement and bentonite grout to determine the resistivity. The measurements indicated a resistivity of about 8.51 Ω -m, indicating that the grout is conductive.

Each electrode was constructed of 0.021 in thick copper sheet. The copper electrodes in Wells 2, 3, and 4 were each 8 in long. The electrodes in the Sparge Well near the injection point were 4 in long, and 8 in long outside of the filter pack area. The electrodes in Well 1 followed this same pattern, because one type of data plane collected between Well 1 and the Sparge Well involved using all of the closely spaced 4 in (0.10 m) long electrodes in both wells for a finer configuration at the point of injection. The electrodes were linked to a connector at the well head by a multiconductor cable. A cross-sectional image of each well showing the electrode arrangements and grout fill can be seen in Figures 4.5, 4.6, 4.7, 4.8 and 4.9, for the Sparge Well and Wells 1 - 5, respectively.

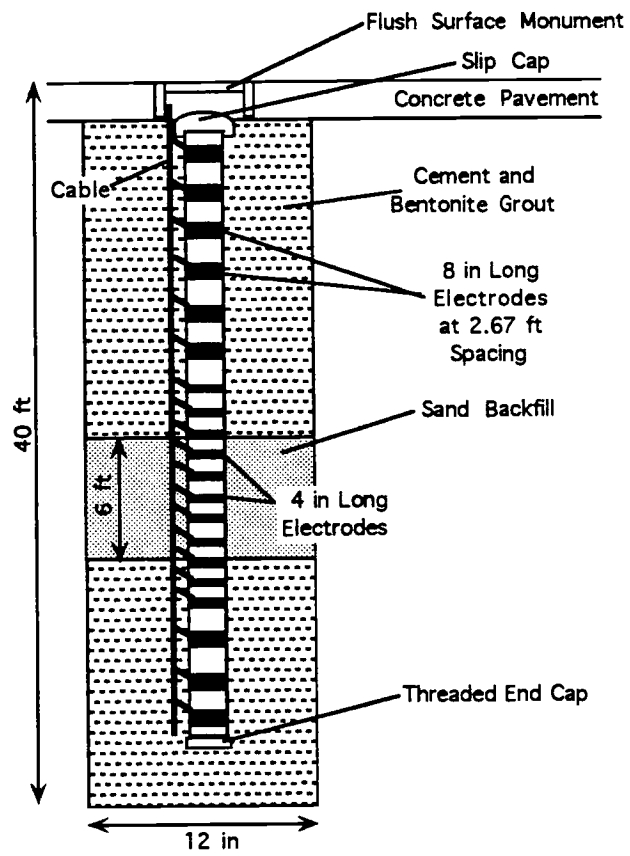


Figure 4.5. Cross-section of Sparge Well.

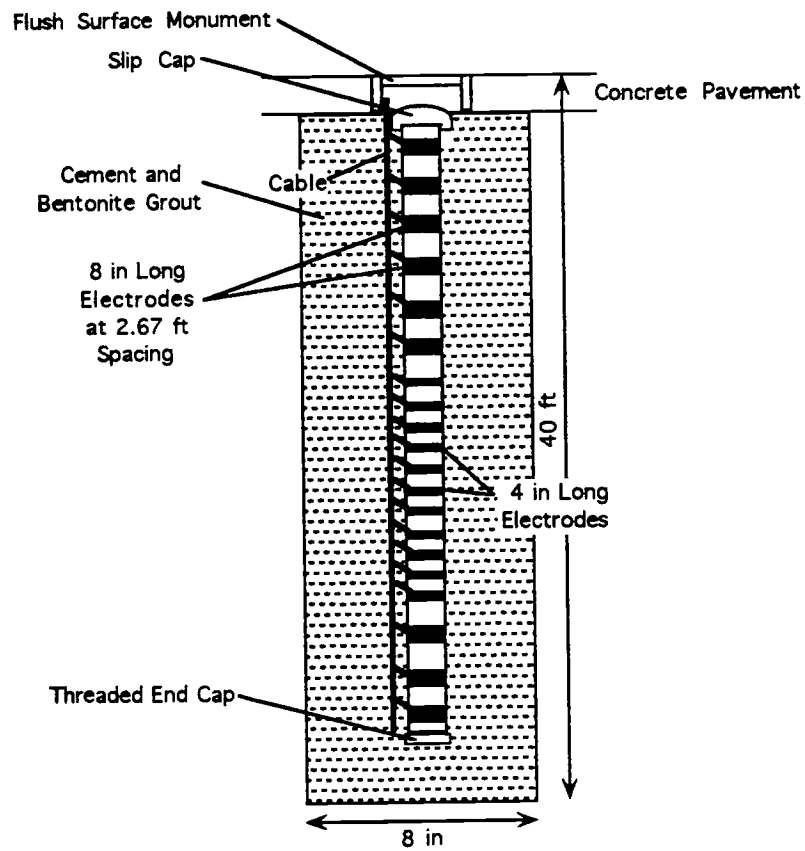


Figure 4.6. Cross-section of Well 1.

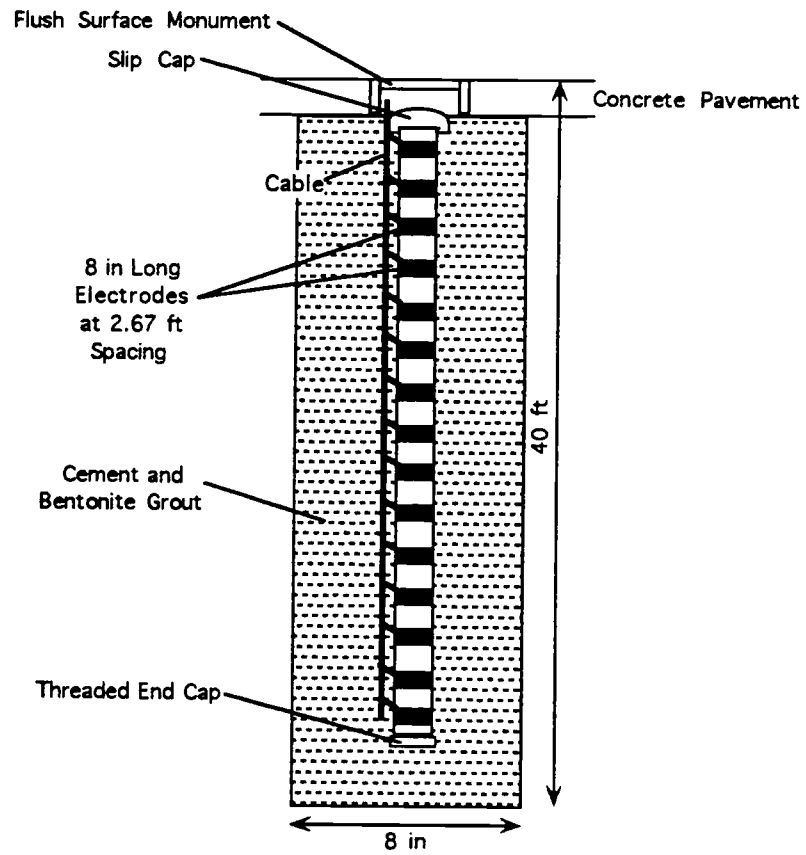


Figure 4.7. Cross-section of Wells 2 and 4.

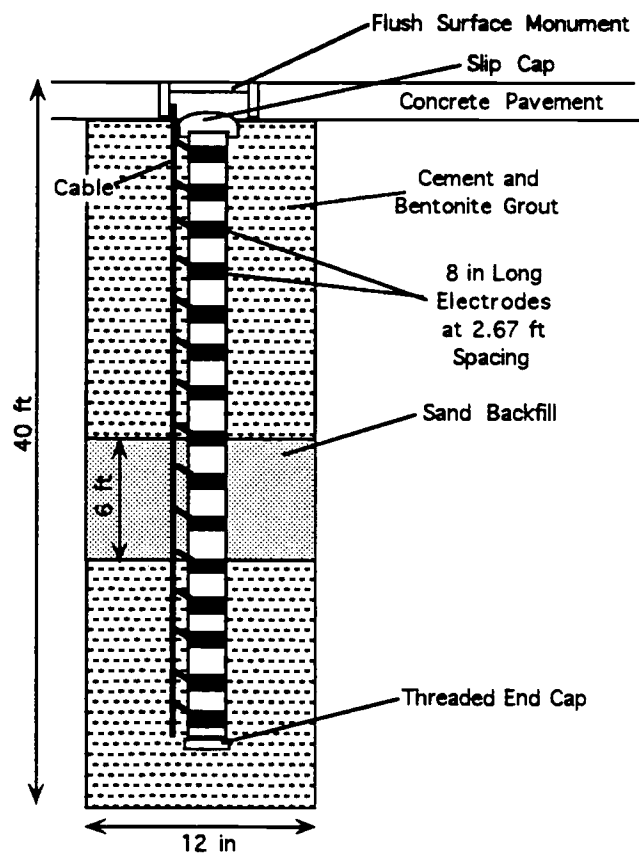


Figure 4.8. Cross-section of Well 3.

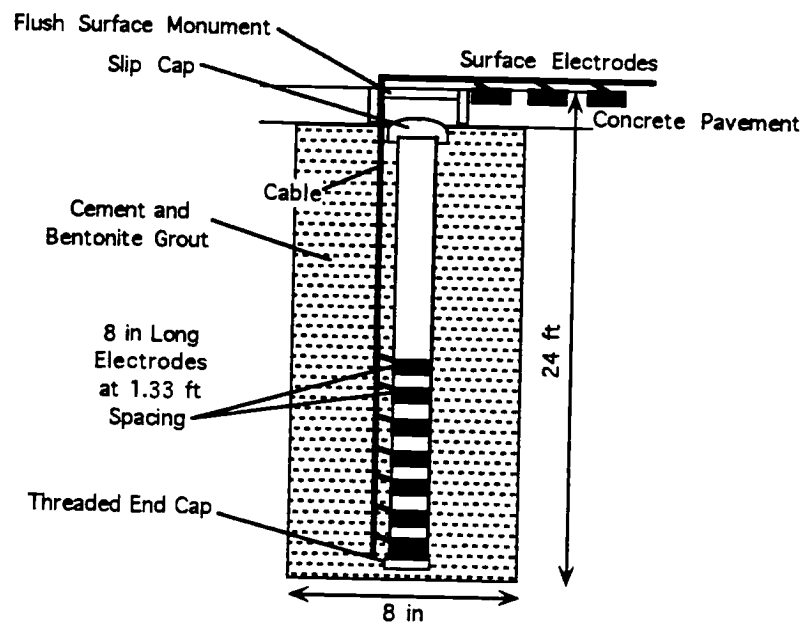
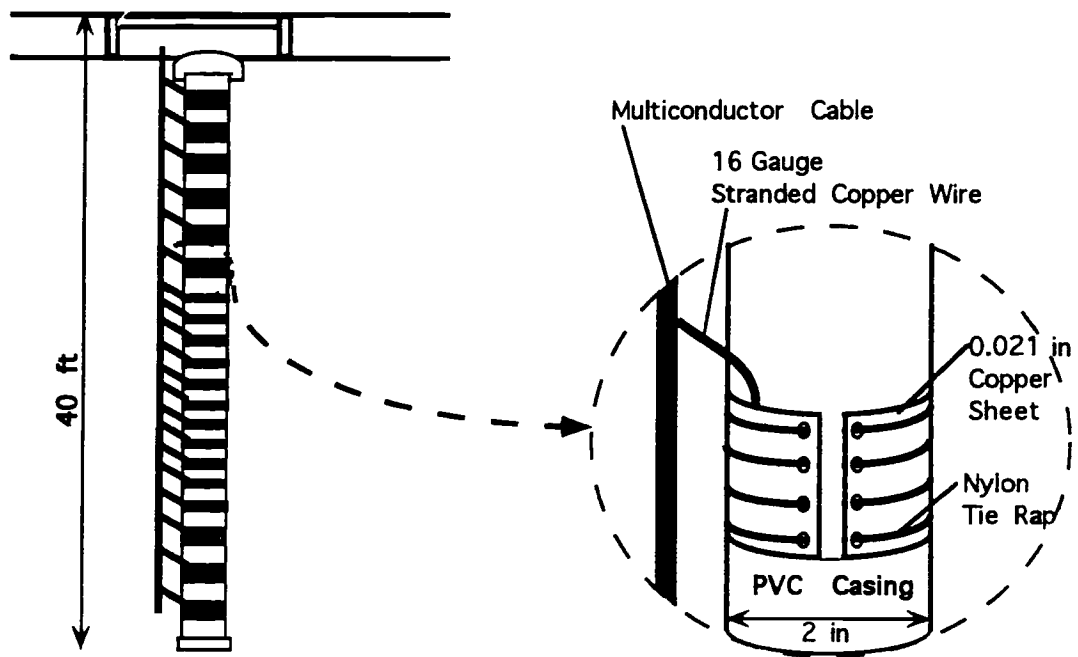


Figure 4.9. Cross-section of Well 5.

Each electrode was wrapped around the well casing and secured in place with nylon tie raps. Additionally, perforations were made in the copper sheet to create a friction surface against the well casing. The detail of the electrode is shown in Figure 4.10.



(Not to scale)

Figure 4.10. Detail of electrode.

To conduct this study, DC resistance together with induced polarization measurements were made using a computer controlled switch system. The induced polarization data were not interpreted for this thesis. A dipole-dipole array was used where every other electrode was used in alternate pairs. For example, a typical measurement would entail electrodes 1 and 3 transmitting in one well, and electrodes 4 and 6 receiving in another well. Cross-borehole measurements were made between the Sparge Well and Wells 1 through 5, and common well measurements were made in the Sparge Well.

The data were collected in planes between two boreholes and within one well and then interpreted tomographically to generate a resistivity image of the subsurface. The resistivity images were compared with background resistivity images and percent change images were produced. Saturation images were also calculated for the portion of the image below the water table.

Background measurements were made for each plane on July 13, 1993. Data were then collected through July 22, 1993 before, during, and after several sparge and vacuum extraction events. A schedule of the air sparge and vacuum extraction events is shown in Table 4.1.

Air Sparging Process

For the sparging process, air was injected with an oil-free compressor at an initial pressure of 8.5 psig (pounds per square inch gauge) (58.57 kPa) which leveled off at a steady state of 6.0 psig (41.35 kPa) after about one hour. The flow rate began at 10.6 cfm (cubic feet per minute) (0.30 m³/min) and reached an average of 18.7 cfm (0.53 m³/min) at steady state. The air was filtered prior to injection to remove any particulate matter. Helium was added as an inert tracer gas in low concentrations (1000 ppm) to the stream of air for tracing the flow of injected air. The Sparge Well

and Well 3 were each equipped with a screened section surrounded by a sand pack from about 30 ft to 33 ft (9.14 m to 10.06 m) depth and 21 to 24 ft (6.40 m to 7.31 m) depth, respectively, where the air entered the formation.

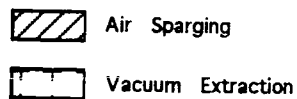
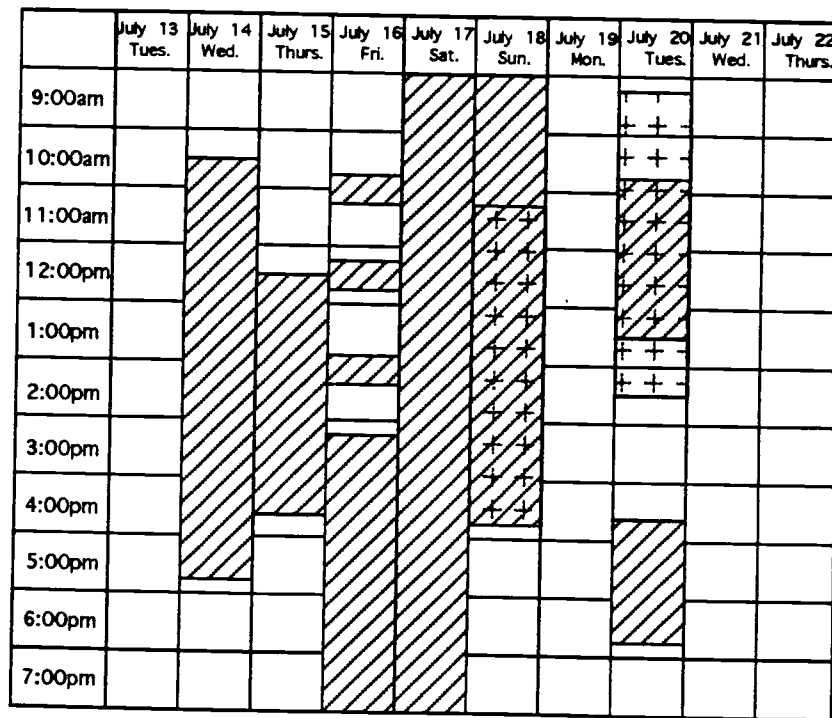


Table 4.1. Schedule of air sparge and vacuum extraction events.

Expected Results

Previous Studies

A previous study involving air sparging was conducted by Brown, et al., 1991. Several sparge tests were conducted, in which air was injected at pressures of 10 psi, 15 psi, and 20 psi in a geologic setting consisting of a granodiorite basement overlain by Quaternary sediments, not vastly different from the Quaternary dune sand setting in my study. I examined the results from Brown, et al where air was being injected at 10 psi (68.91 kPa), the closest pressure to the average 6.0 psig (41.35 kPa) at which air was being injected for my study in this thesis. The results from Brown, et al. suggest that the sparged air has a radius of influence of 72 to 78 ft (21.94 m to 23.77 m) when injected at 10 psi at a depth between 30 ft and 33 ft (9.14 m to 10.06 m). Based on these results, I would expect to encounter a similar radius of influence of the sparged air in my study.

Previous in-lab studies also indicate air flow paths resulting from sparging occur either in channels or bubbles. However, early reports showing air moving as bubbles in saturated media have almost been entirely discounted, due to a lack of understanding of the physics involved. According to Johnson et al., 1993, the air will usually not occur as bubbles in saturated porous media, but rather as continuous channels. A study by Ji et al., 1993, reaffirms the channel theory as being the most probable flow pattern for the sparged air. With these studies in mind, I might expect to encounter channeling of air during the sparging process, but probably not any air flow in the form of bubbles.

The distribution of bulk resistivity with increasing water saturation was calculated based on a Waxman equation for unconsolidated sands. Table 4.2 is a graph showing the varying of bulk resistivity with saturation. With the injection of air into the

saturated zone, percent water saturation may become as low as 20 % in the areas of highest air concentration. This corresponds to resistivity values up to about 4200 Ω -m. I would expect to see resistivities this high in the saturated zone during the sparging process.

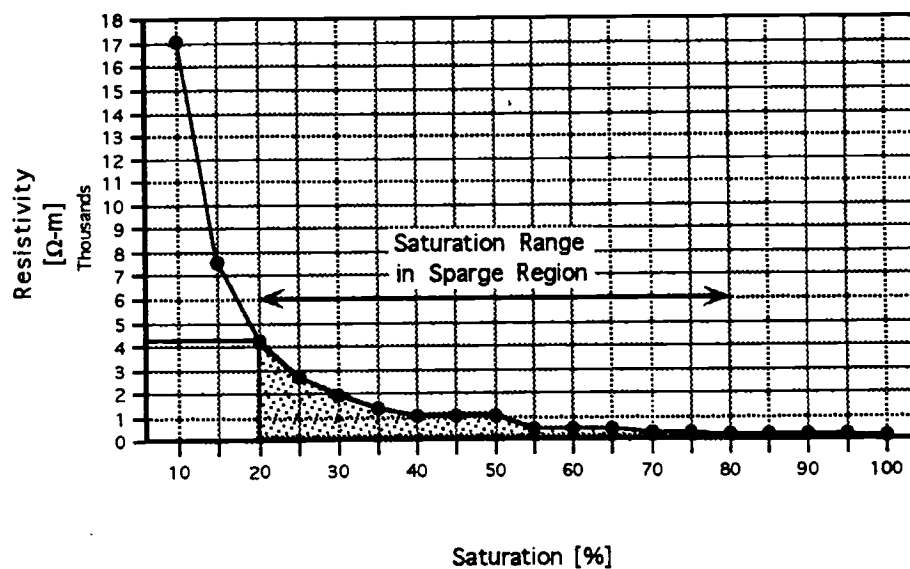


Table 4.2. Graph of water saturation Vs resistivity.

Results

Resistivity Reconstructions

Data were collected along Planes A through H, shown in Figure 4.4. Data were interpreted, however, for Planes C, B, and H only. Time constraints and complications arising from the code used for interpretation did not allow for the remaining planes to be interpreted within this thesis. Furthermore, data interpretation was only done for the sparge events in which the air injection originated from the Sparge Well, and not for the sparge events in which the air injection originated from Well 3, which occurred on July 19.

C Plane

The images generated in the C Plane, between the Sparge Well and Well 3, are discussed here. The background resistivity image from July 14, 1993 is shown in Figure 4.11. The subsequent tomographic reconstruction images in Figures A1-A20 display the large increases in resistivity at the point of air injection at various times after the flow of air had commenced, and can be found in the APPENDIX.

In the background image, resistivity values in the saturated zone, below the water table, range from 200 to 400 Ω -m. These values should be uniformly 400 Ω -m. In the unsaturated zone, the range in resistivity extends up to 1600 Ω -m. These higher resistivities indicate the presence of unsaturated sand above the water table, and should be uniformly 1600 Ω -m.

These uniformities are not seen due to interference from the grout that surrounds the wells. The conductive grout can be seen along the Sparge Well in the images of Figures 41 - 60. Unfortunately, the conductive grout in Well 3 is not modeled correctly by the program for axially symmetric interpretation. Thus the grout is "smeared out," making the right side of the images appear more conductive than they

should. This is particularly noticeable in the vadose zone. Whereas the water table would realistically be represented by a flat boundary between the saturated and unsaturated zone, it is shown in the images to be uneven.

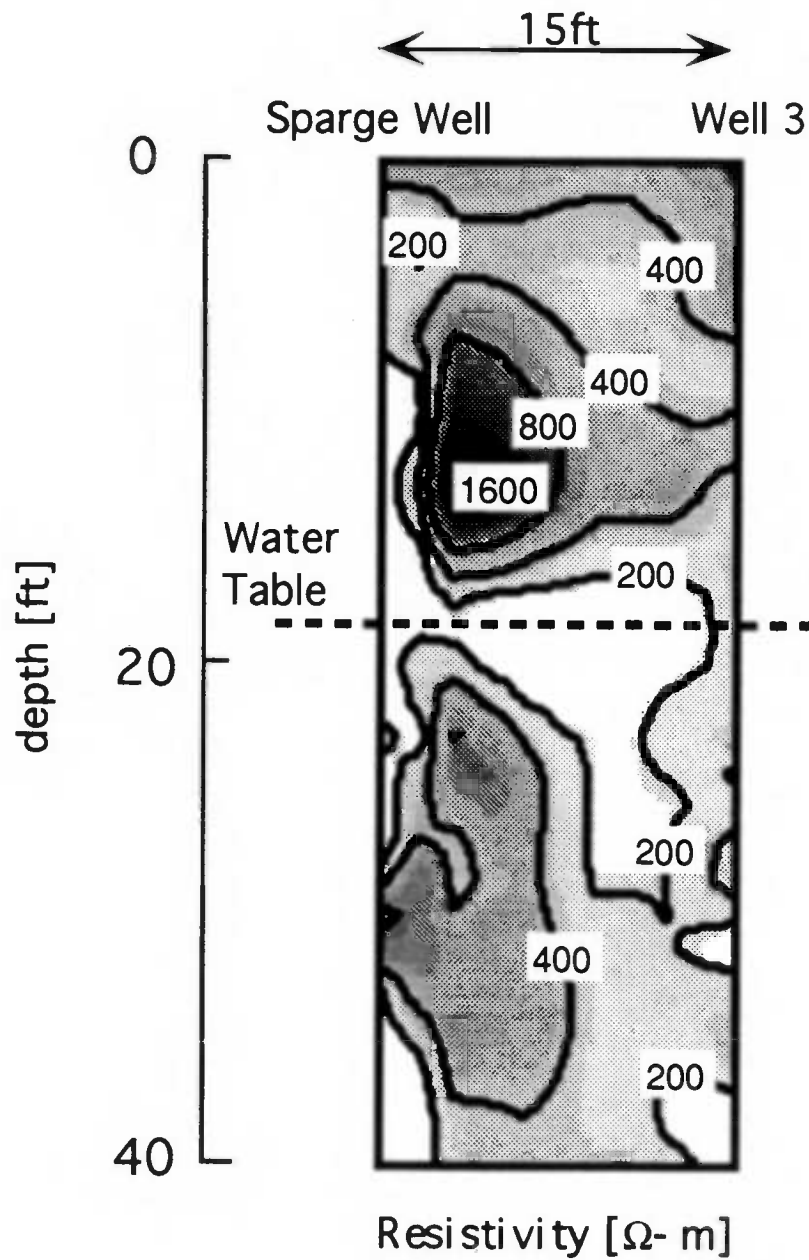


Figure 4.11. Resistivity reconstruction, C Plane, Background, July 14, 1993.

After 20 minutes from the beginning of the sparge event, Figure A1, a 3200 Ω -m resistivity region has formed, extending out about 2.5 ft (0.76 m) from the Sparge Well and up about 2.5 ft (0.76 m) above the point of injection. The air actually entered the formation not in the screened interval, but rather at the top of the filter pack that surrounded the screening. Thus the "point of injection" of air referred to is this point at the top of the sand pack. The 3200 Ω -m area is thought to be a region where air has displaced nearly all of the formation water. A highly resistive zone of air, 1600 Ω -m, extends upwards and slightly outwards from this indicating the presence of air saturation but to a lesser degree than the 3200 Ω -m zone. After 1 hour, Figure A2, the 3200 Ω -m resistive area remains the same lateral distance away from the injection point, but has a 1600 Ω -m peak extending in the direction of flow (upwards) indicating an increase in the area where air has displaced water.

Three hours after the sparge began, Figure A3, the 1600 Ω -m area has increased in resistivity to 3200 Ω -m, indicating that the air may be creating a pathway up to the vadose zone. In Figure A4, four hours and twenty minutes after sparging began, the shape of the highly resistive zones remains virtually the same. The sparge was shut off, and the first image generated for the C Plane is one hour after shut off, Figure A5. The resistivities below the water table have reduced considerably, with a high of 1600 Ω -m occupying a small region near the injection point. The pathway above the injection point has reduced to 800 Ω -m. Nearly two hours after shut off, Figure A6, the image appears almost the same, indicating possible entrained air lingering in the saturated zone.

A second sparge event was initiated on July 15, preceded by a background image, shown in Figure A7. The only changes between this image and the last image generated on July 14 after shut off should be a decrease in resistivities as water in the saturated zone replaces the air injected. However, the image of Figure A7 shows an unusual highly resistive zone around the point of injection due either to borehole effects or possible seepage of air from the injection point. About one hour after the sparge began, Figure A8, the region extending from the injection point to the vadose zone has already reached a high of 3200 Ω -m, suggesting that the first sparge event may have facilitated a pathway for the air to flow. Two hours after sparging, Figure A9, the 3200 Ω -m region has increased in size. Three hours after sparging, Figure A10, the image remains virtually the same, however the 3200 Ω -m region has moved up toward the water table slightly. The sparge was shut off, and the image in Figure A11 was created, showing the results after about one hour. Here, the resistivities below the water table have reduced to a high of 800 Ω -m in the areas where some air still remains.

A series of half-hour sparge events were cycled on July 16. The first image, Figure A12, for the plane between the Sparge Well and Well 3 was a background before any cycles. This image is almost identical to the image of Figure A11, confirming that the saturated zone had already reached a stable state by the time the data were collected in Figure A12. Figure A13 is the image after three half-hour sparges, about two hours into the start-up of a long lasting sparge event. The 3200 Ω -m regions near the injection point and above it are smaller than during previous sparge events, but in the same areas as previous events. On July 17, the image of Figure A14 was generated, showing the nature of the saturated zone after sparging had been on for over twenty hours. Interestingly, the 3200 Ω -m zone of highest air

saturation is located above the injection point, and is thinner laterally than in previous sparge events. The image generated from July 18 after nearly 42 hours of sparging, Figure A15, is nearly the same shape as Figure A14, except there is now a highly resistive 3200 Ω -m zone at the injection point.

The vacuum extraction system (VES) was turned on while the sparge was still running on July 18. Subsequent resistivity images were generated, beginning with Figure A16 taken about one hour, twenty minutes after the VES was turned on, and Figure A17 taken about two hours, thirty minutes after the VES was turned on. Both images reflect the unchanging lateral extent of the air path. A noticeable lengthening of the path toward the water table as compared to before VES was turned on is indicative of the vacuum extraction drawing air upwards. The images generated from July 20, 21, and 22, Figures A18, A19, and A20, respectively, all show the long term effects of air sparging on the saturated zone. In Figure A18, nearly 36 hours after sparging had been off, the resistive regions that appear in the air flow paths from previous sparges represent air entrained in the subsurface. Figures A19 and A20 also display air entrapment.

H Plane

The H Plane was collected between the Sparge Well and Well 5, a monitor well that was equipped with 7 downhole electrodes and 3 surface electrodes. Because the electrodes in Well 5 were not constructed with an outer layer of grout and bentonite, measurements were only made on July 20 during the vacuum extraction process when the level of the water table had risen enough to create a contact for each electrode. The following is a discussion of the resistivity images generated from July 20 for this plane. These images, Figure A21 - A27, can be found in the APPENDIX.

The background image taken before air sparging began, Figure A21, shows a highly resistive area near the injection point, 2000 Ω -m, due to previous sparge events. A 1000 Ω -m region extends upwards from the injection point towards the now elevated water table. After ten minutes from the beginning of sparging, Figure A22, the region near the injection point has increased in resistivity to 3000 Ω -m, and the area extending upwards has increased to 1500 Ω -m, indicating the pathway where air is replacing water. After twenty minutes, Figure A23, the region of 3000 Ω -m remains the same in size near the injection point, and a more continuous path now exists of 1500 Ω -m extending out from this. After one hour, 30 minutes, Figure A24, the pathway extending upward has become more saturated with air, as indicated by an increase in resistivity to 3000 Ω -m. Figure A25, two hours, twenty minutes after sparging began, shows an increase in the size of the highly resistive zone near the injection point, and a lateral thinning of the 3000 Ω -m zone above this.

After the sparge was shut off, the resistivities have decreased to nearly background values as seen in Figure A26, ten minutes after sparge shut off, and Figure A27, twenty minutes after sparge shut off. This indicates the ability of the

saturated zone to quickly replace the air filled areas with water to an allowable extent, leaving some entrapped air.

B Plane

The resistivity data discussed here are from measurements between the Sparge Well and Well 2, the B Plane. This data plane is stricken with severe borehole effects, and thus is not interpreted in great detail. Figures A28 - A30 can be found in the APPENDIX.

A background image was generated on July 13, before any sparge events, shown in Figure A28. The resistivities are low, similar to the resistivities generated in the background from the C Plane in Figure 4.11. However, a second background measurement was made on July 14, also before any sparge events, Figure A29, and two 3200 Ω -m regions appear near the injection point and in the vadose zone, obvious results of borehole effects. After one hour, thirty minutes since the sparge began, Figure A30, the highly resistive region remains channeled against the Sparge Well and extends into the vadose zone.

All of the remaining images for this data plane show this "channeling" of high resistivities up against the Sparge Well, indicating borehole effects and diminishing the usefulness of these data.

Percent Difference Images

Percent change images are useful for reducing borehole effects and gaining a clearer understanding of the changes from the background. A representative sampling of resistivity images was chosen for generating percent change images to illustrate the most important points of this study. Percent change images were created by finding the percent difference between a chosen resistivity image and a background image of the same data plane, using the following formula:

$$100 * \frac{(\text{post-injection resistivity} - \text{pre-injection resistivity})}{\text{pre-injection resistivity}}$$

C Plane

Twenty minutes after the first sparge on July 14, the greatest percent changes occur at the point of injection, 1500%, and in a zone of 200% extending about 8 ft upward from this and about 2 ft outward, Figure 4.12. The percent change after one hour of sparging indicates the point of injection as still being the most highly resistive, and the region above it now increased in intensity and size, reaching the water table, as shown in Figure 4.13. After three hours of sparging, Figure 4.14, resistivity at the injection point has decreased to 50% of the background, but the resistivity above it has increased to 500% greater than background and has grown in size. The 300% and 200% contours that flank the 500% zone have moved upward and outwards as well.

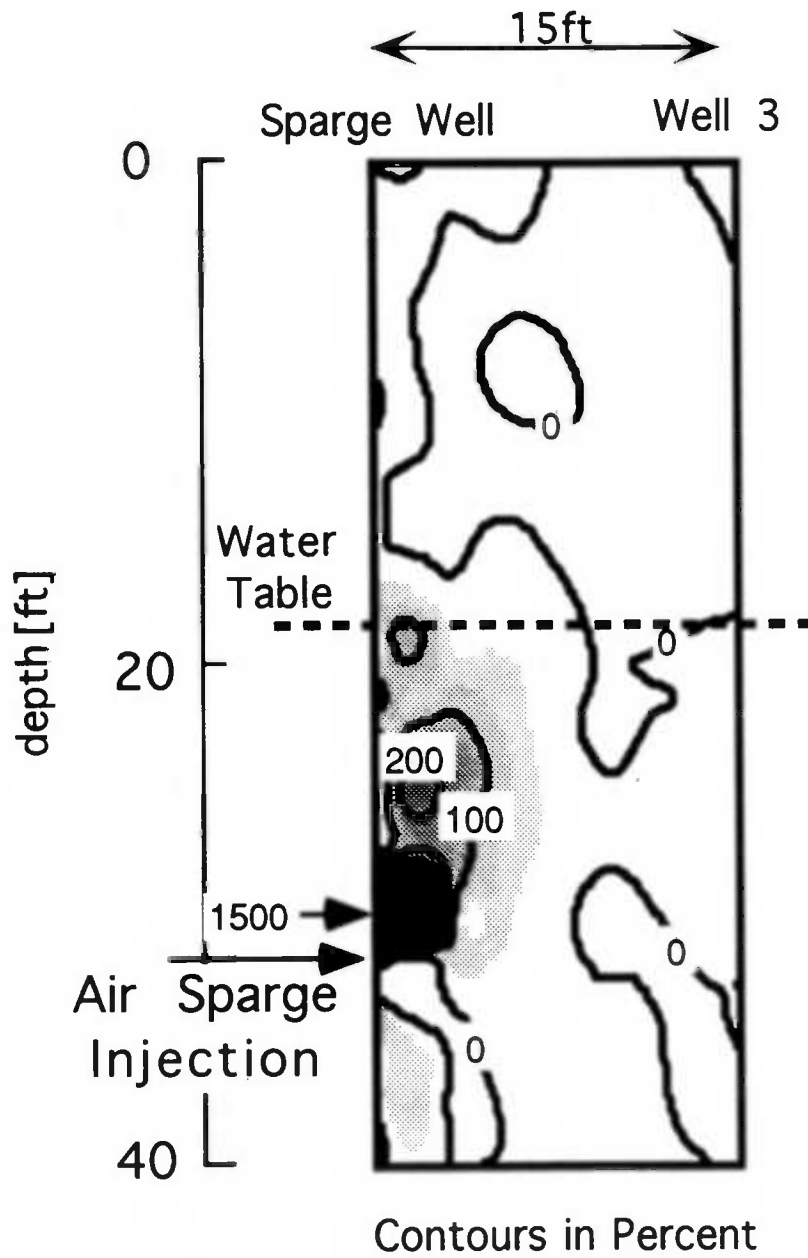


Figure 4.12. Percent difference reconstruction, C Plane, 20 minutes after sparge began, July 14, 1993.

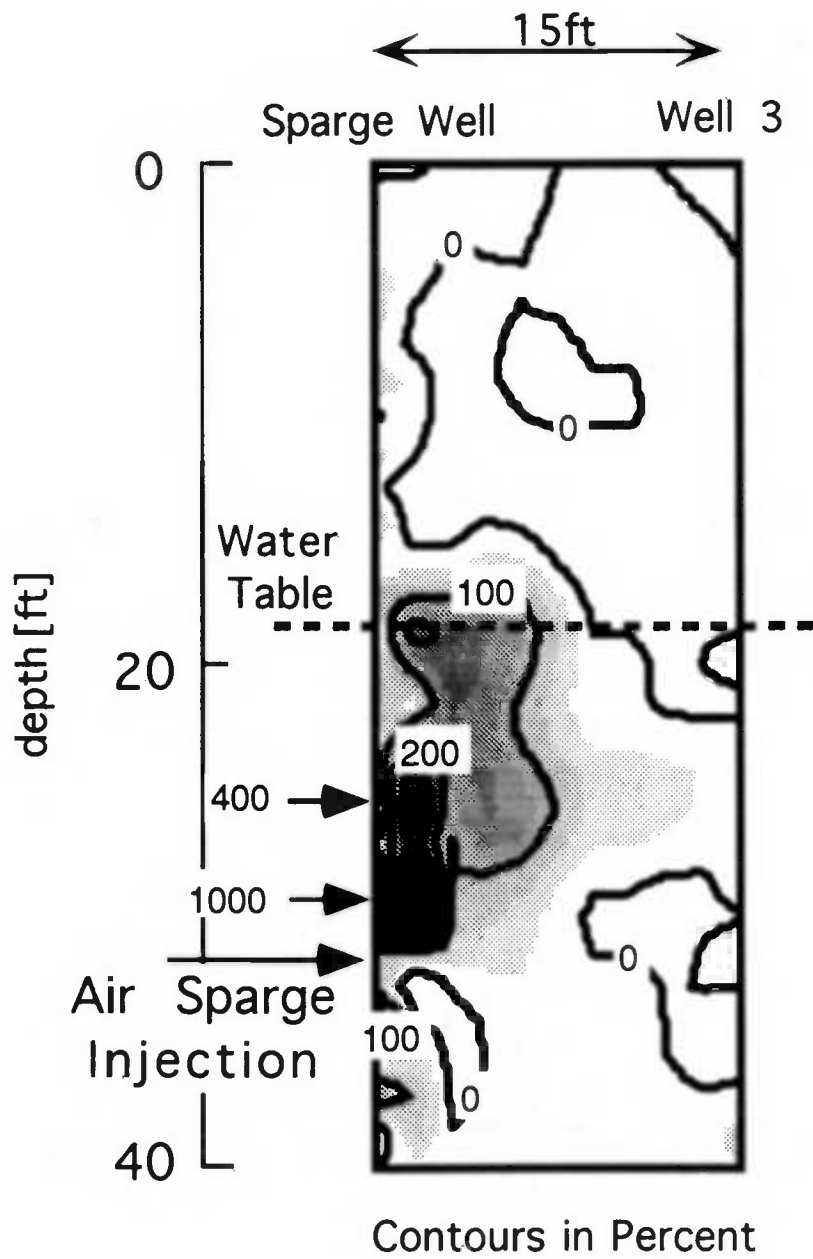


Figure 4.13. Percent difference reconstruction, C Plane, 1 hour after sparge began, July 14, 1993.

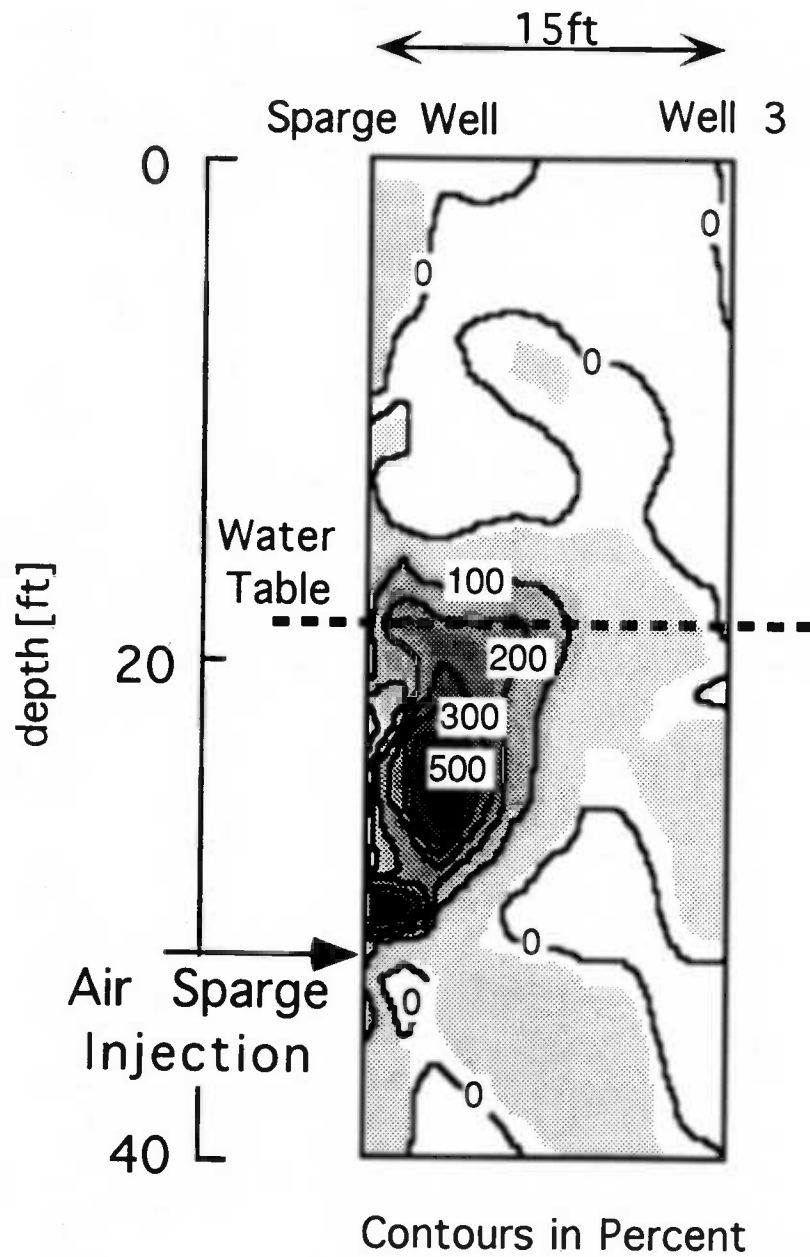


Figure 4.14. Percent difference reconstruction, C Plane, 3 hours after sparge began, July 14, 1993.

One hour after the first sparge event was shut off, Figure 4.15, the subsurface has returned close to the background resistivity. The regions that were occupied by air during the sparging have mostly been replaced by water in the saturated zone. A 100% change still exists near the point of injection, where refilling may be taking the longest time. Also a 100% change still occurs in a small zone at the water table, evidence of air entrapment. Figure 4.16 shows a conceptual model of the zone of influence of the injected air after 48 hours of continuous sparging. These results are for near steady state conditions; the air region assumes an inverted cone shape, tapered at the point of injection, and widening until it reaches the water table. The proposed cone shape would extend three-dimensionally around the Sparge Well, as shown in the conceptual drawing. Figure 4.17 shows the residual changes due to long term sparging about 36 hours after sparging stopped. Note there is a substantial amount of air entrained in the saturated zone, especially just below the water table. For the most part, though, the vadose zone resistivities have not changed.

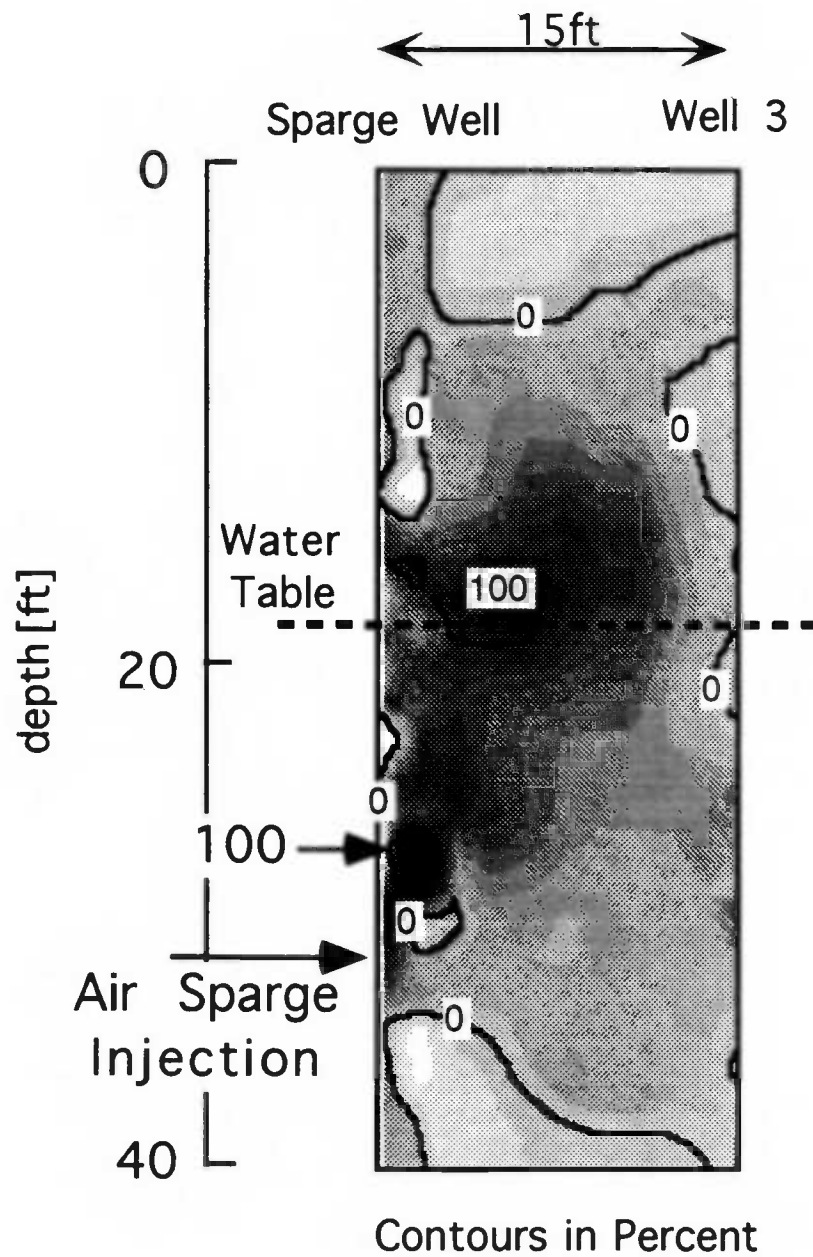


Figure 4.15. Percent difference reconstruction, C Plane, 1 hour after sparge shut off, July 14, 1993.

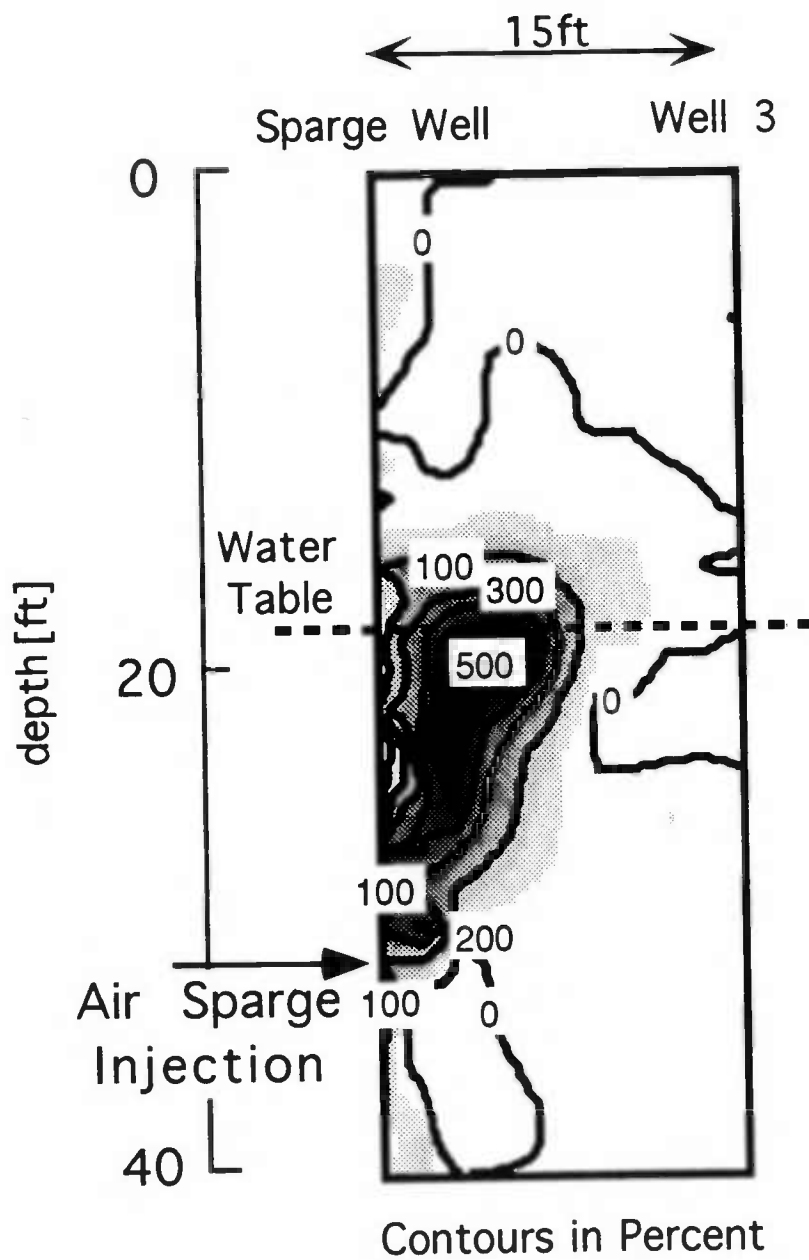


Figure 4.16. Percent difference reconstruction, C Plane, after 48 hours of continuous sparging, July 18, 1993.

H Plane

Similar to the previous plane discussed, the greatest percent changes during early sparge times are at the point of injection and extending up from it. All figures for the percent differences of the H Plane are found in the APPENDIX. Figure A31 shows the percent change ten minutes after sparging began. After twenty minutes of sparging, Figure A32 the greatest changes are seen along the Sparge Well above the injection point, where air is migrating upward. Figures A33 and A34 show the growing lateral extent of changes one hour, thirty minutes after sparging began and two hours, twenty minutes after sparging began, respectively. After ten minutes and then twenty minutes since sparge shut off, Figures A35 and A36, respectively, the percent changes have decreased, but some residual changes exist where water has not yet completely replaced the air.

The results from the percent change analysis illustrate two major points. The first is that the zone of influence resulting from continuous sparging assumes a cone shape, narrow at the injection point and wide at the water table. The second is that the areas of the subsurface affected most by air sparging are not the areas at the injection point, but rather above this, in the flow path of the air, where air has likely become entrapped and unable to be replaced again by formation water. There were virtually no changes in the vadose zone during all of the sparge cycles, except for the slight mounding seen just above the water table, as was expected with the air displacement.

Water Saturation Images

Percent saturation images were generated for the saturated zone using an Archie type equation for clean sands. The equation is as follows, assuming the background is 100% saturated and a saturation exponent of 2:

$$\text{Saturation} = \sqrt{\frac{\text{Observed Resistivity}}{\text{Background Resistivity}}}$$

This formula assumes that air is uniformly distributed throughout a finite element pixel, about 1.3 ft by 1.3 ft. However, it may be questionable how accurate the pixels are if the air is distributed in small channels rather than uniformly. Applying a mixing model such as Maxwell's model for small, thin, resistive parallelepipeds in a homogeneous background (Maxwell, 1891), the resistivity effect is reduced from that of Archie's Law. Thus the saturation percentages in Figures 4.18 - 4.23 give the minimum value of the average saturation as the contour interval. They show that although the air may be moving in channels, the formation water has been displaced over a relatively large volume.

A progression of saturation images is shown in Figures 4.18 - 4.23. Percent saturation images were only calculated for the images in the plane between the Sparge Well and Well 3, the C Plane. In these saturation images, 100% is full water saturation.

During the initial phases of air injection, Figure 4.18, the saturation is seen to have decreased greatly, to 30%, at the injection point, with lesser changes occurring

above this. After one hour, Figure 4.19, the change in saturation is still the greatest at the injection point, with changes of 80% below the injection point, and changes extending farther out laterally above the injection point. Here, it is likely that the air was forced into the formation with a pressure great enough to have displaced water in the downward direction. Later saturation images, Figures 4.20 - 4.23, indicate that the zone of lower water saturation, now 60% to 80%, remains not at the point of injection, but above this, near the water table.

The percent saturation images support the results seen in the percent change images of Figures 4.12 - 4.17. Systematic changes do occur through time beginning with the largest concentration of air saturation at the injection point, and ending with formation of a cone of air saturation, the highest concentration now being above the injection point.

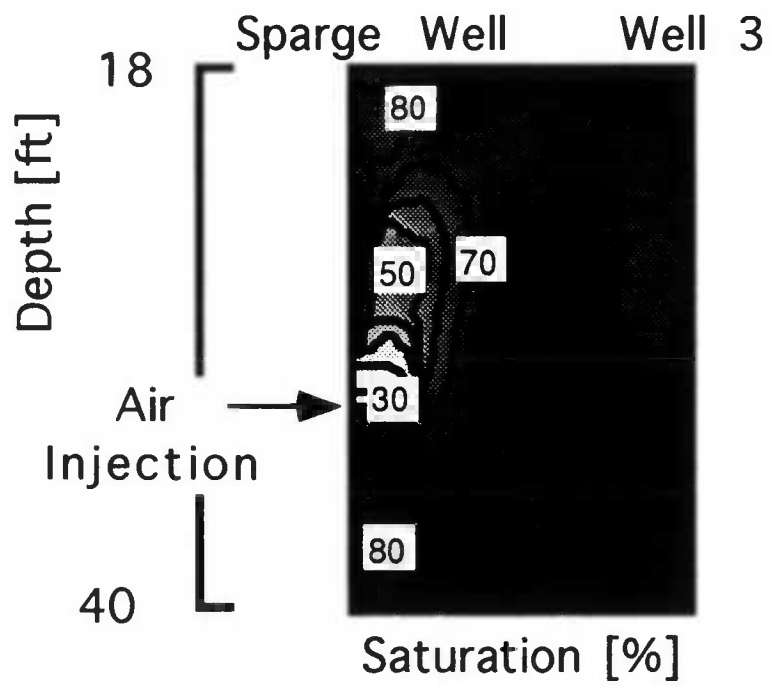


Figure 4.18. Percent saturation reconstruction, C Plane, 20 minutes after sparge began, July 14, 1993.

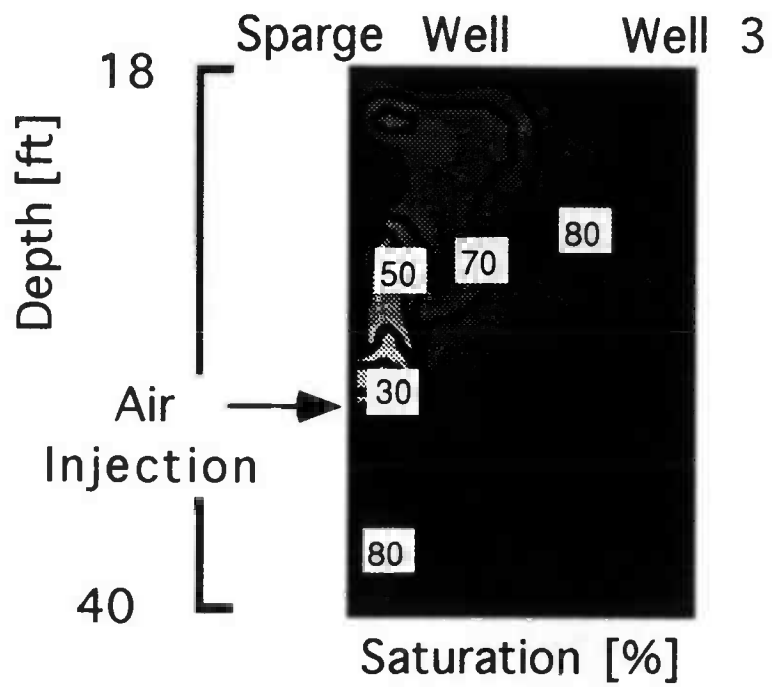


Figure 4.19. Percent saturation reconstruction, C Plane, 1 hour after sparge began, July 14, 1993.

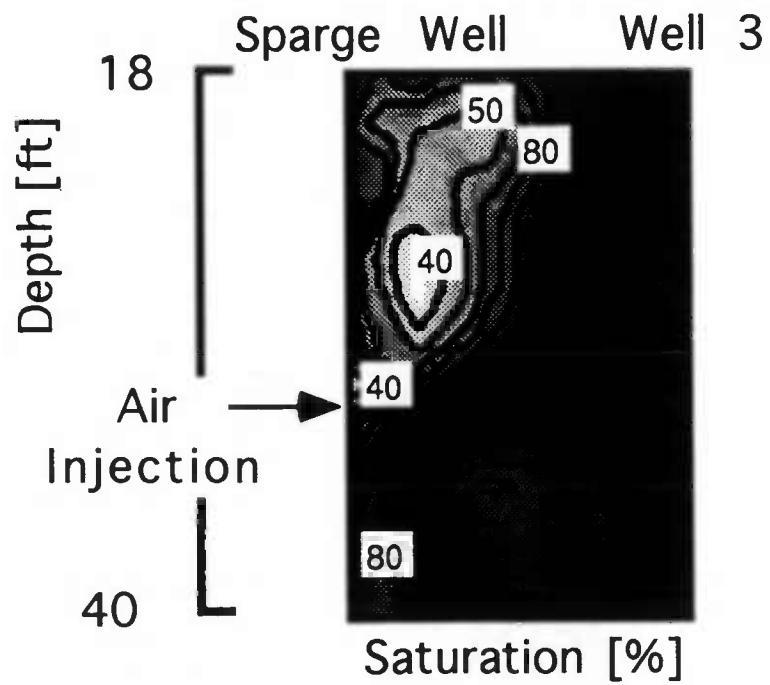


Figure 4.20. Percent saturation reconstruction, C Plane, 4 hours, 20 minutes after sparge began, July 14, 1993.

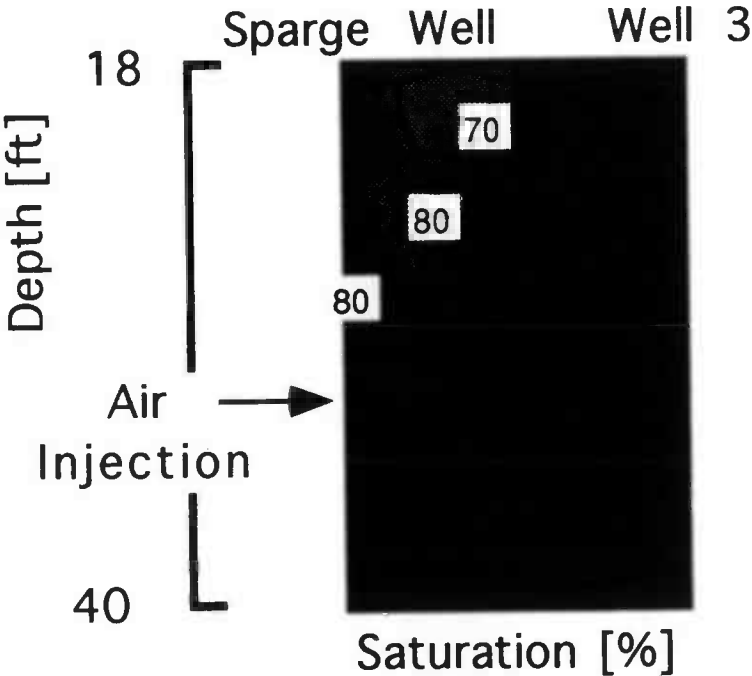


Figure 4.21. Percent saturation reconstruction, C Plane, after second sparge began, July 16, 1993.

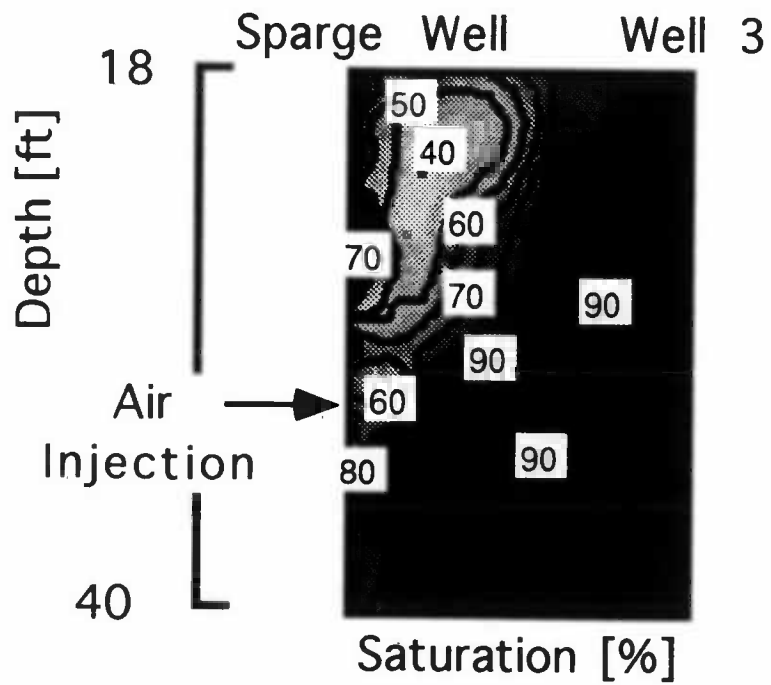


Figure 4.22. Percent saturation reconstruction, C Plane, 48 hours after continuous sparging, July 18, 1993.

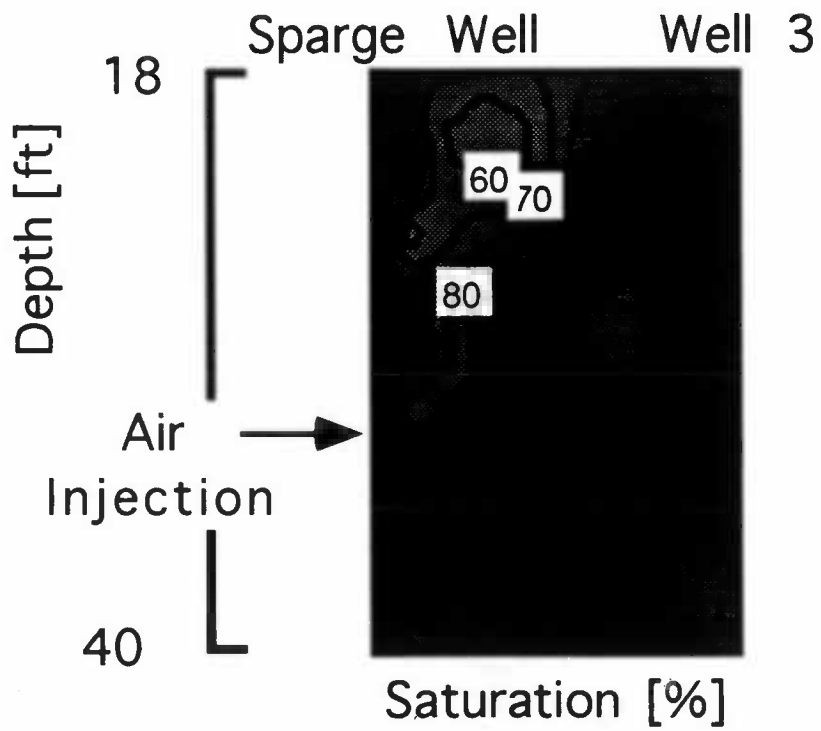


Figure 4.23. Percent saturation reconstruction, C Plane, long term effects, July 20, 1993.

Conclusions

The anomalies that are generated in the subsurface as a result of the air sparging are best seen in the percent change images, Figures 90 - 100. The results indicate that after one hour of sparging, the air has a lateral extension from 3 to 9 ft from the point of injection, somewhat smaller than indicated in previous literature (Brown, 1991). After a long period of several sparge events, the data show that lasting changes to the saturated zone have occurred by the presence of residual entrapped air.

I have concluded through these preliminary findings, that resistivity tomography provides an excellent means of monitoring the flow of air through time around a sparge well. The results from near steady state sparging indicate that systematic changes do occur through time, ultimately producing a cone that fans out to the water table. The air saturation zones resulting from air sparging travel in somewhat continuous regions that are narrower than previously thought, based on the results of this study. Furthermore, these regions of air are quickly refilled by water to a large degree after sparging stops. This shows that cycling the sparging on and off should be an effective means of remediating a large volume of ground water. The presence of entrapped air, however, indicates that the saturated zone does experience long term effects from air sparging. The pattern of air flow observed here is similar to that seen in laboratory experiments (Ji et al., 1993) and simulations of homogeneous materials (Lundegard and Anderson, 1993).

CHAPTER 5

SUMMARY

Geophysical imaging of the subsurface is fast becoming recognized as an effective tool for monitoring environmental remediation sites. In this thesis, I explore the benefits of cross-borehole resistivity and IP tomography as a reliable imaging technique for environmental applications.

In the first study, cross-borehole resistivity and IP surveys were carried out at Avra Valley to track a line-source water injection. The injection was fully contained in a 30 m by 30 m by 5.9 m deep lined basin filled with unconsolidated sediments representing the vadose zone. Resistivity measurements were taken between four wells, each with 12 electrodes, before and after the injection of Tucson tap water, which totaled 24,000 L. Resistivity and IP distributions were reconstructed using a non-linear, two-dimensional inversion of a finite element forward solution of Laplace's equation.

After injection, images showed a distinct decrease in resistivity through time which outlines the zone of increased saturation. A significant increase in IP was observed in these zones as well. Preliminary laboratory studies show similar IP increases resulting from the leaching of salts from the soil by tap water, indicating the possible ability of IP to describe soil salinity. Based on the results of this study, I feel that resistivity and IP tomography is an excellent technique for subsurface imaging that can be used in conjunction with remediation efforts. The complex nature of plume movement demands methods with accuracy and high resolution for detection. The combination of IP and resistivity tomography effectively fulfill this criteria.

In the second study, cross-borehole resistivity surveys were conducted in Florence to monitor air sparging in the saturated zone. Air sparging is a relatively new

technique for the remediation of ground water contaminated with petroleum hydrocarbons in which air is injected below the contaminated area. As the air rises, hydrocarbons in the soil partition into vapor which is removed by vacuum extraction. Because air sparging has only recently been applied to field scale studies, little is known of the distribution of the air underground during the process.

In the survey, resistance measurements were taken between the sparge well and several wells radially surrounding it during and after periods of sparging. Resistivity distributions were reconstructed using an inversion of Poisson's equation that assumes axial symmetry about the sparge well. The resulting images show clearly the regions of the saturated zone occupied by air as high resistivity areas. After steady state sparging, the injected air assumes an inverted cone shape around the sparge well. These results reinforce the findings from the Avra Valley study: that resistivity tomography provides an effective means of imaging the subsurface.

Closing Remarks

Electrical resistivity tomography is in the forefront of technology for environmental monitoring. The studies conducted in this thesis were some of the first of their kind to be carried out in the field. I believe that the results obtained from this work demonstrate the usefulness of resistivity and IP tomography for accurate subsurface imaging.

The potential for future work in resistivity tomography is vast. An improved data acquisition system would have the capability to acquire measurements from more than just one plane at a time, and collect data quicker. Capabilities such as these enable a larger sampling of images to be generated for monitoring time-varying changes. Resistivity and IP tomography is a promising tool for future environmental monitoring that will be refined as it becomes more widely used.

APPENDIX

Resulting Images from Florence, Oregon

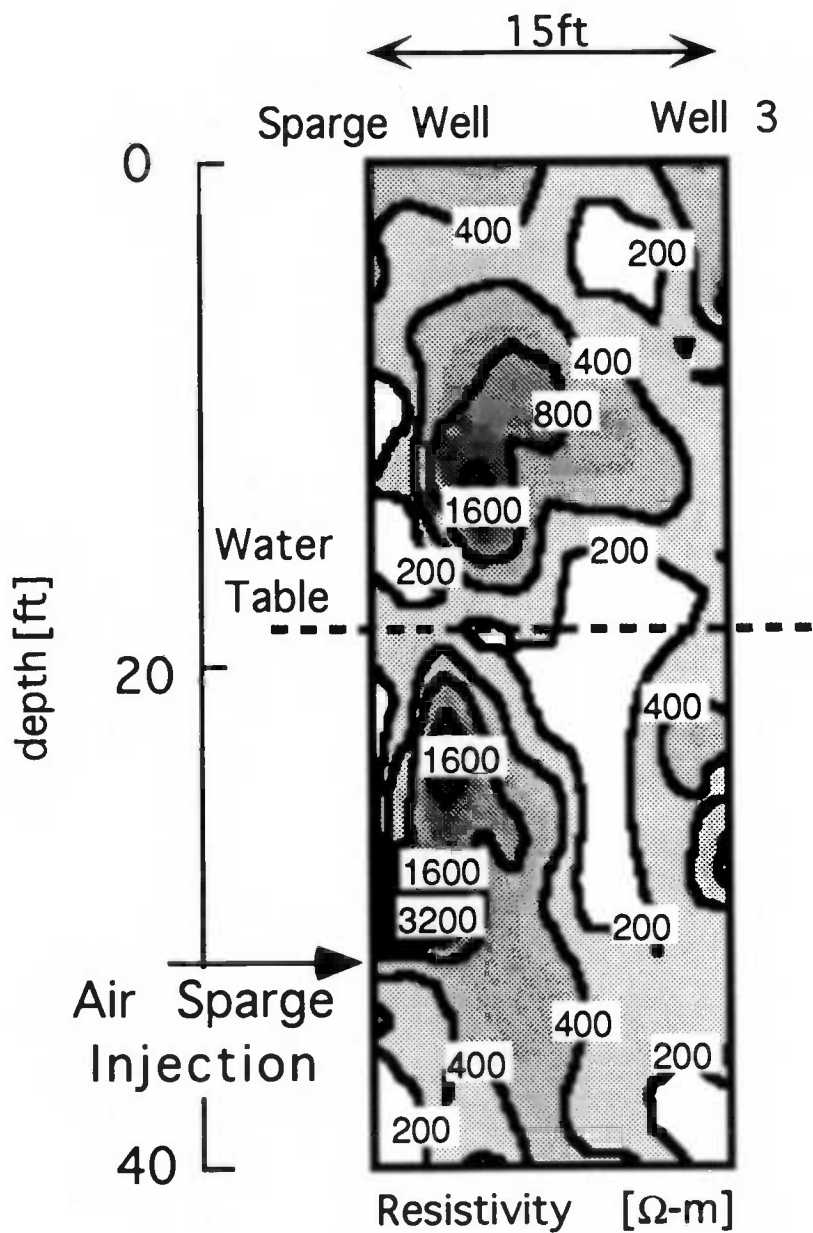


Figure A1. Resistivity reconstruction, C Plane, 20 min after sparge began, July 14, 1993.

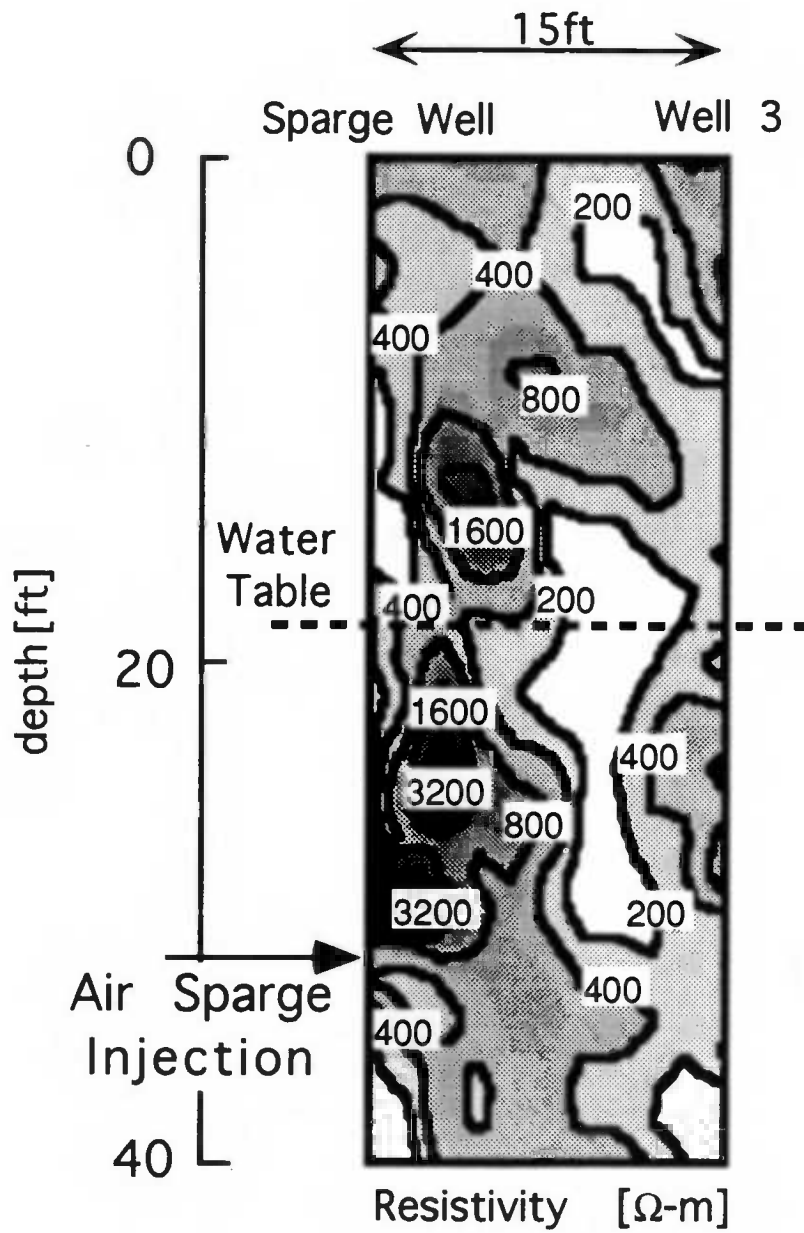


Figure A2. Resistivity reconstruction, C Plane, 1 hr after sparge began, July 14, 1993.

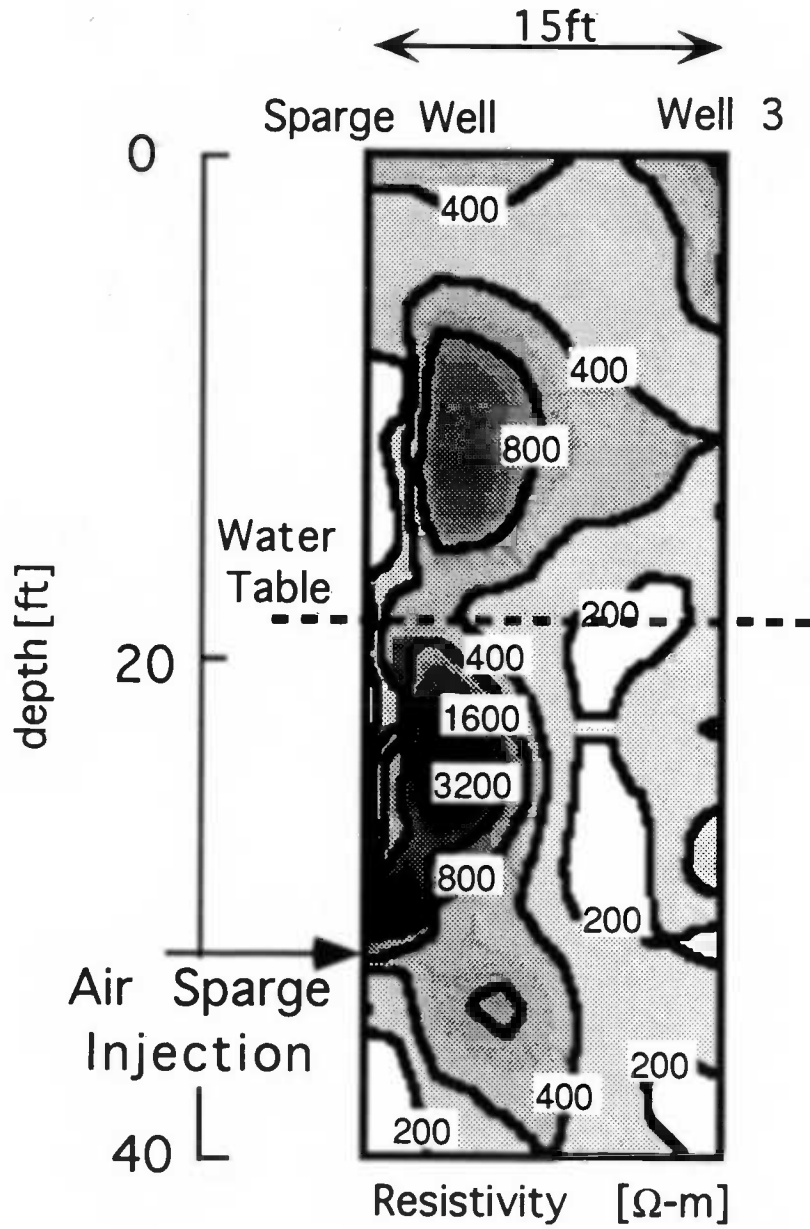


Figure A3. Resistivity reconstruction, C Plane, 3 hr after sparge began, July 14, 1993.

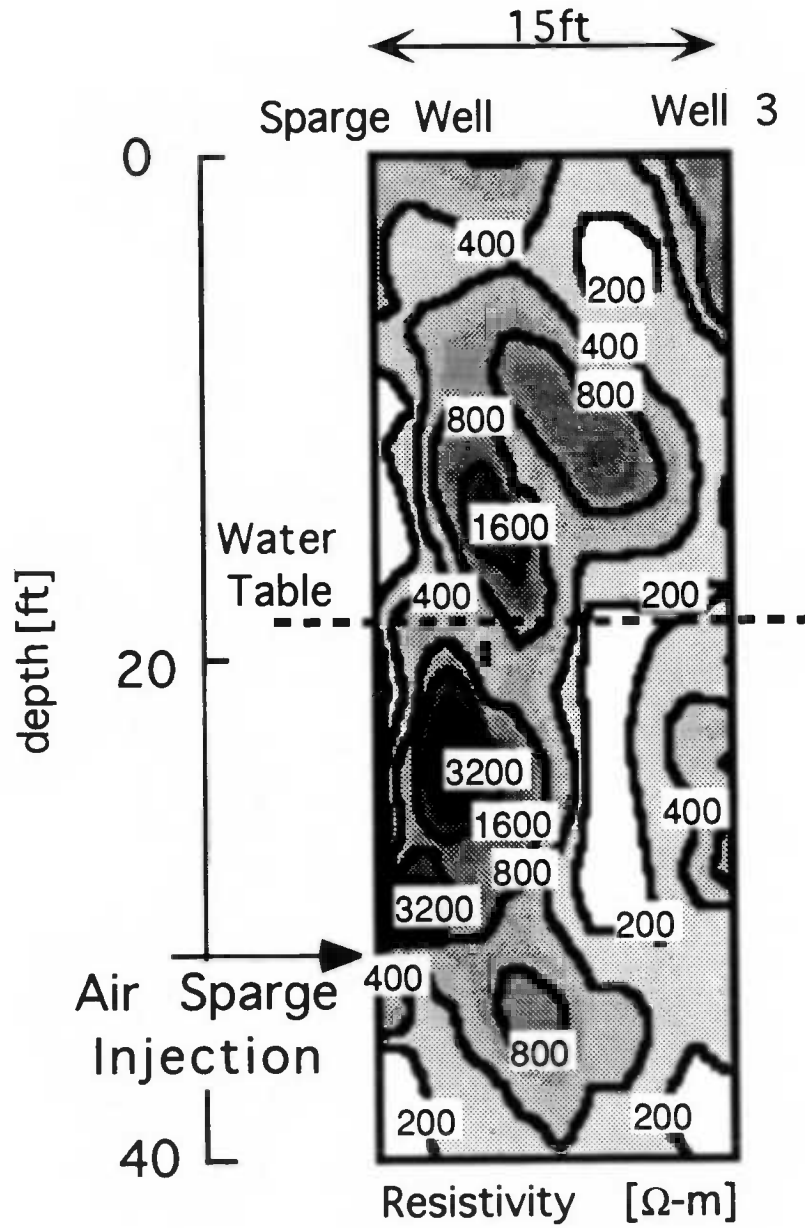


Figure A4. Resistivity reconstruction, C Plane, 4 hr, 20 min after sparge began, July 14, 1993.

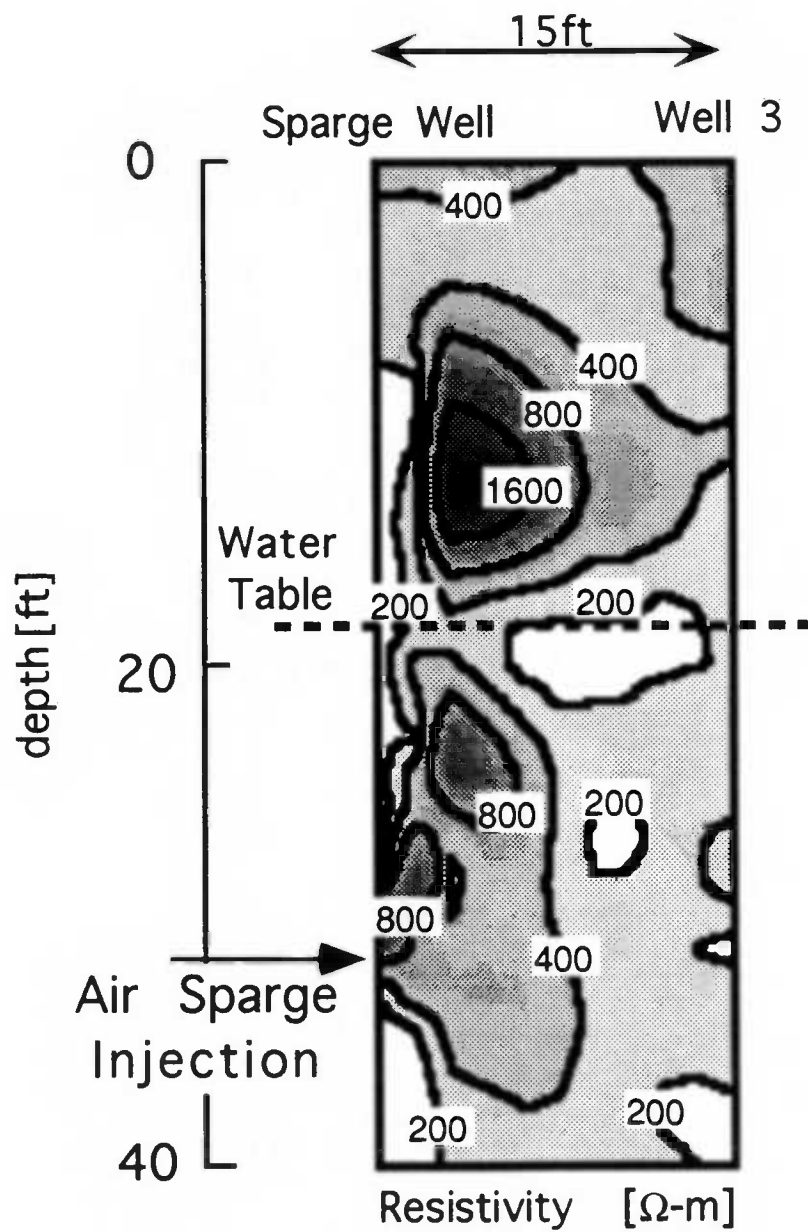


Figure A5. Resistivity reconstruction, C Plane, 1 hr after sparge off, July 14, 1993.

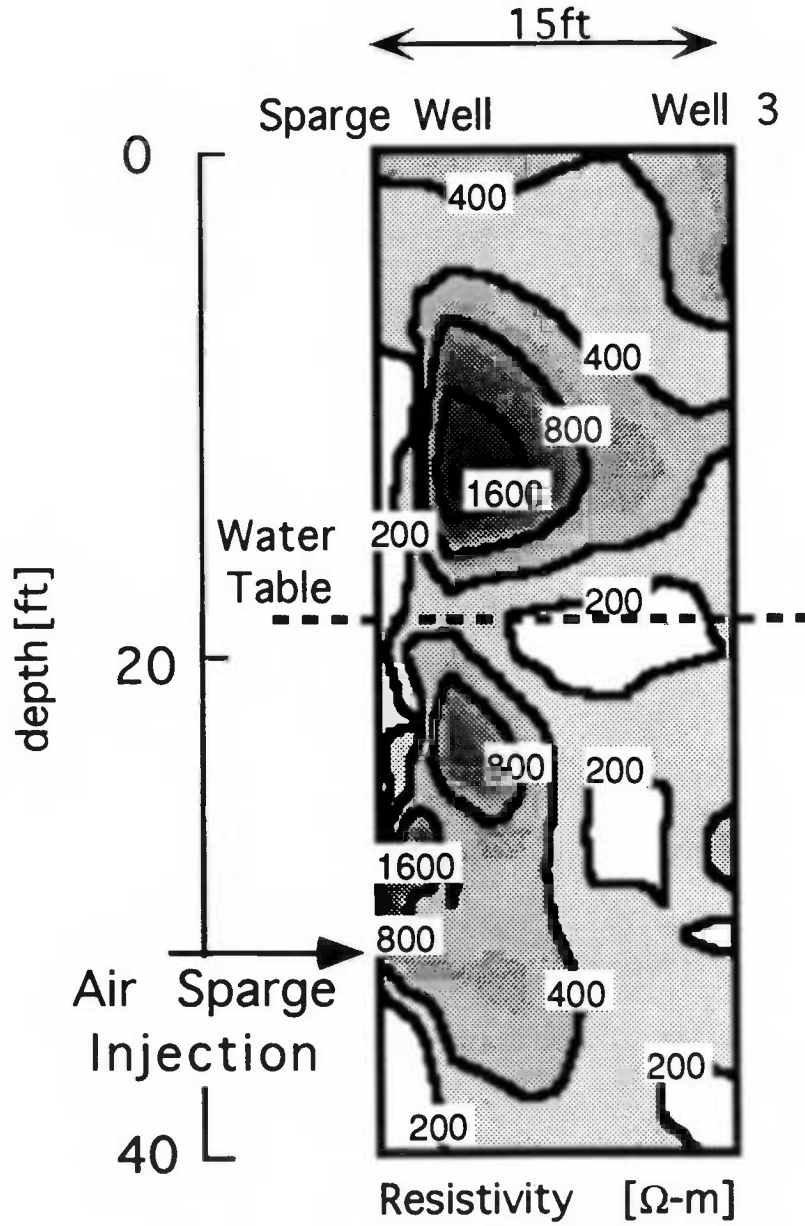


Figure A6. Resistivity reconstruction, C Plane, 2 hr after sparge off, July 14, 1993.

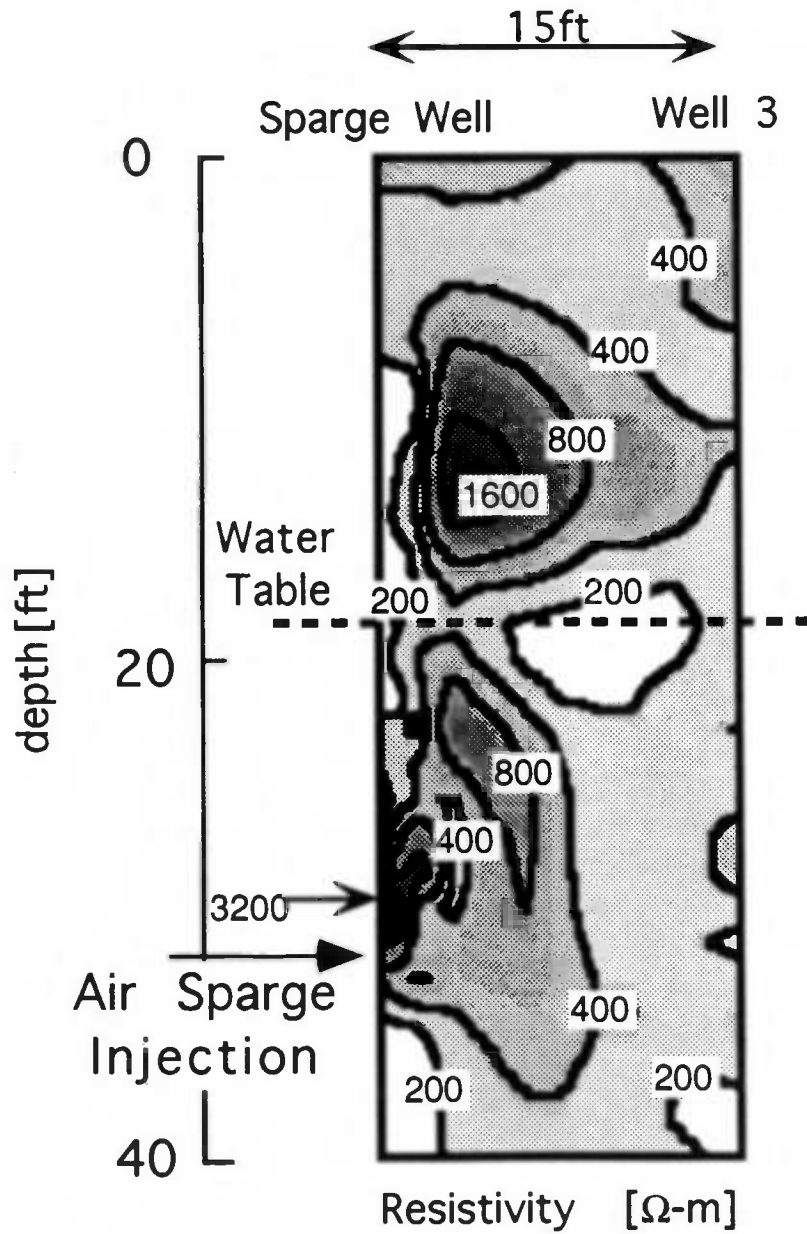


Figure A7. Resistivity reconstruction, C Plane, Background, July 15, 1993.

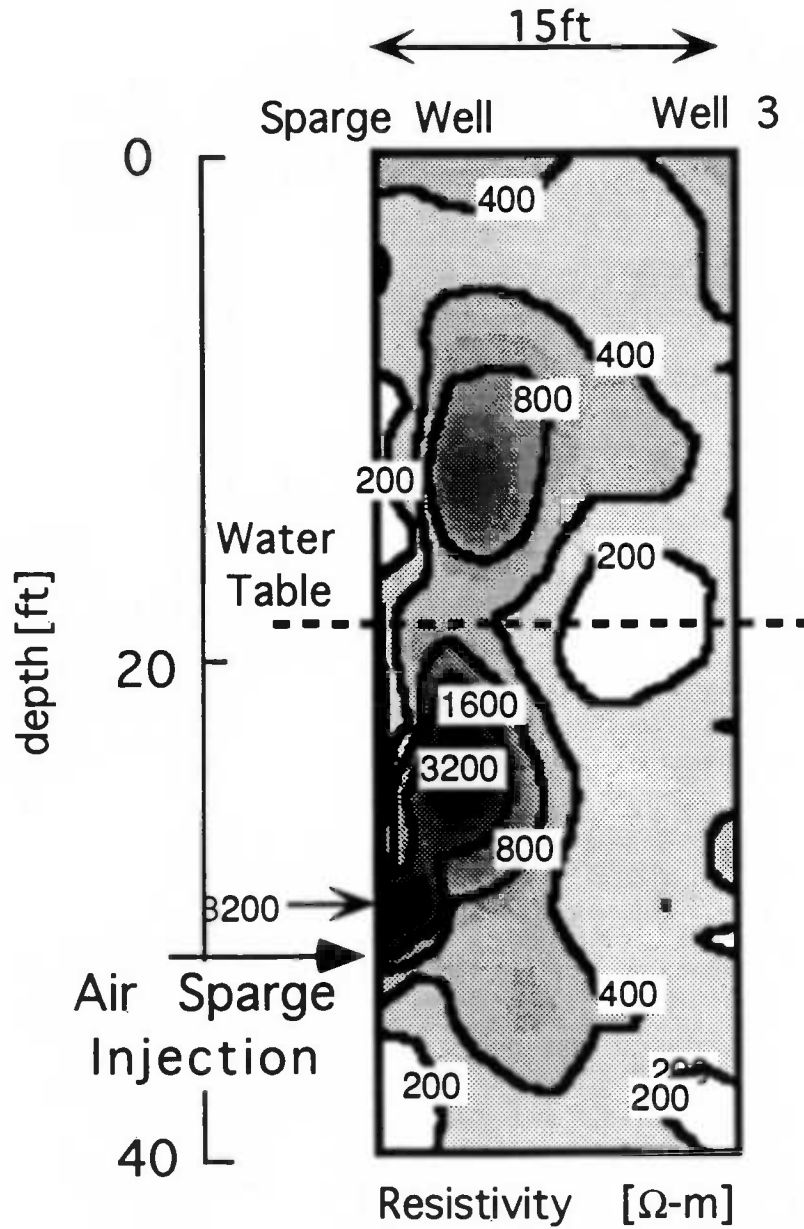


Figure A8. Resistivity reconstruction, C Plane, 1 hr after sparge began.
July 15, 1993.

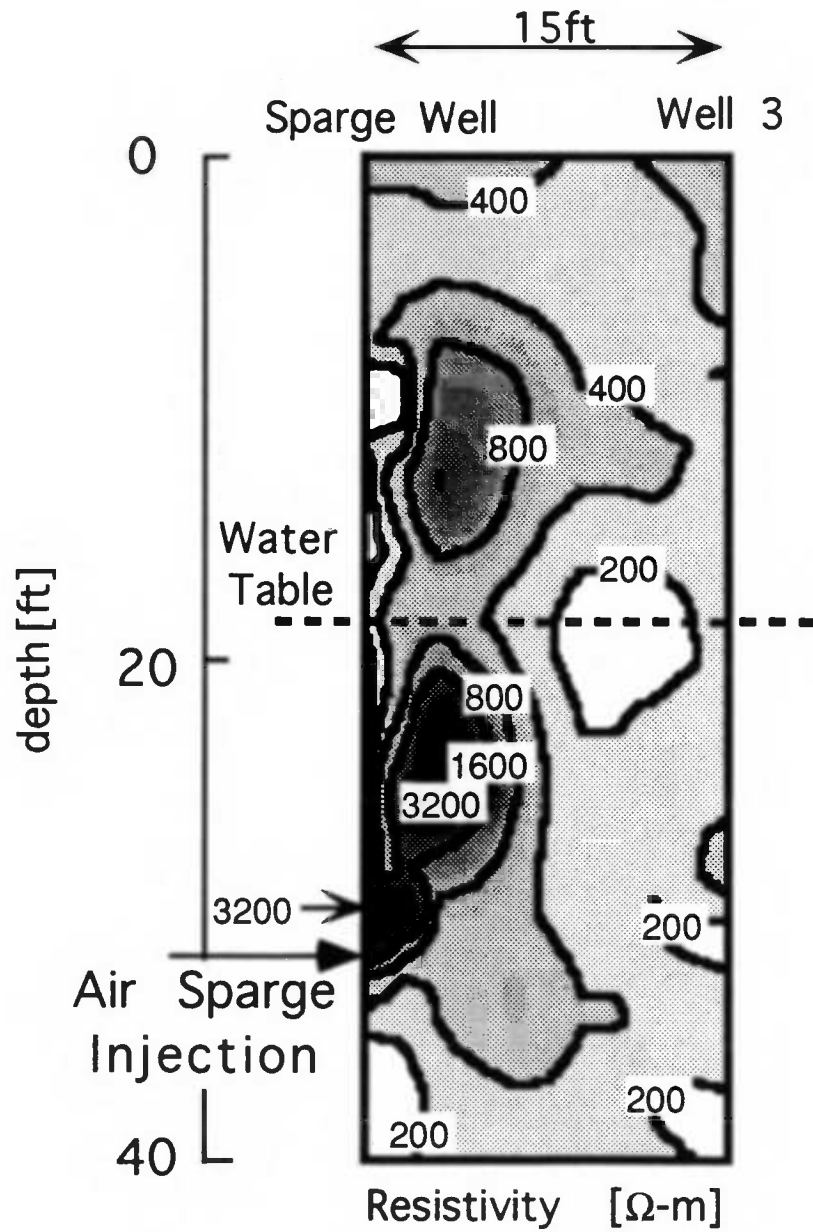


Figure A9. Resistivity reconstruction, C Plane, 2 hr after sparge began, July 15, 1993.

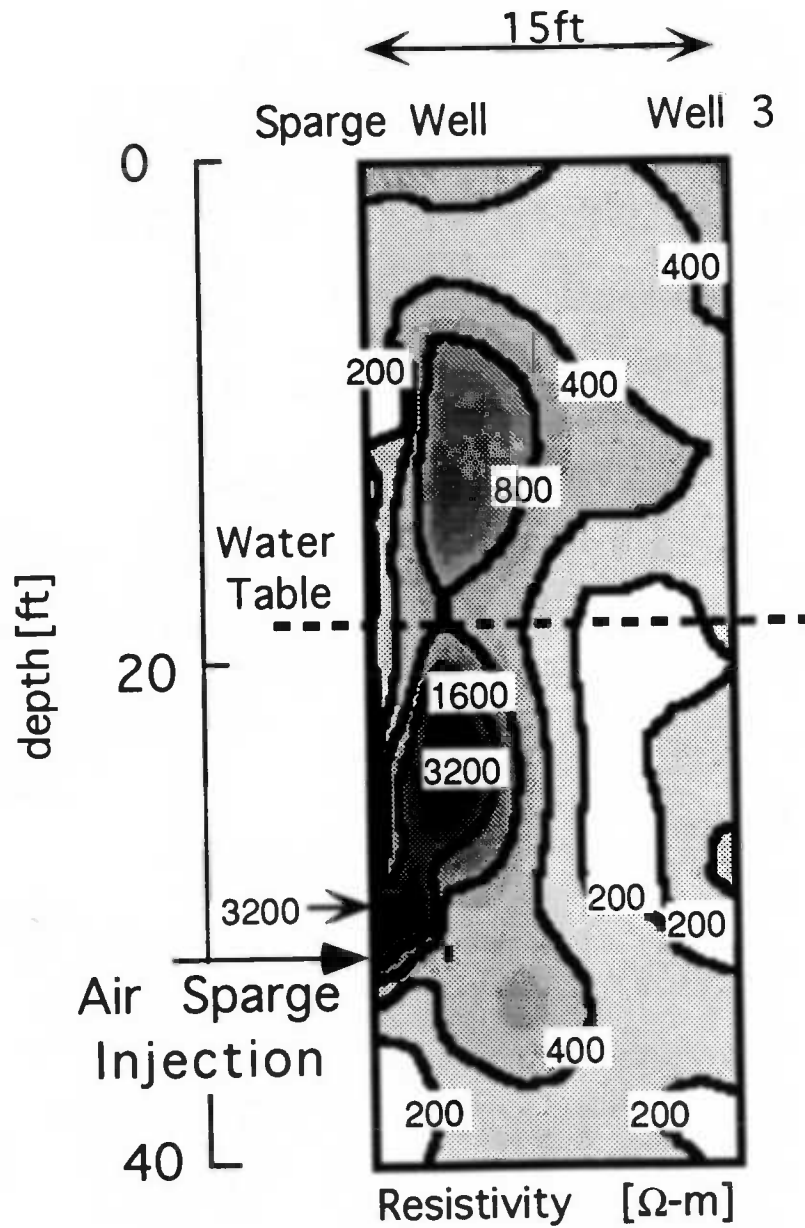


Figure A10. Resistivity reconstruction, C Plane, 3 hr after sparge began, July 15, 1993.

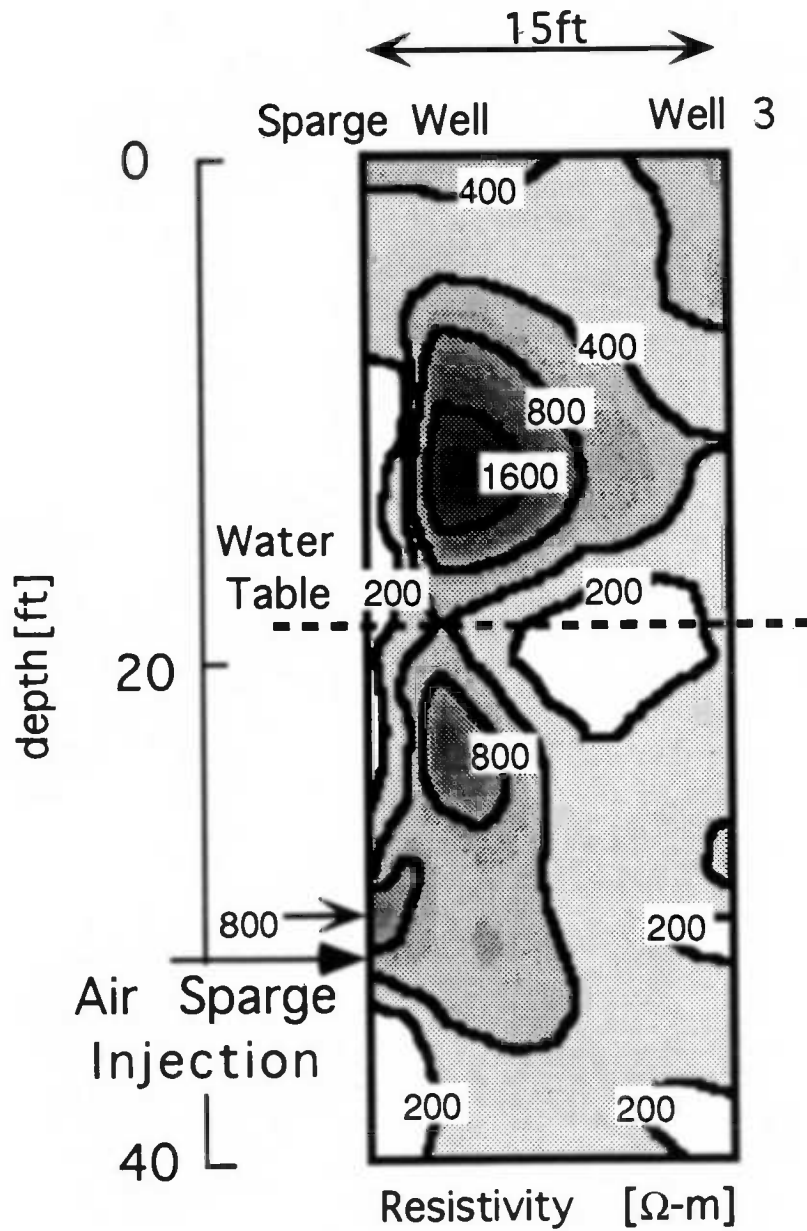


Figure A11. Resistivity reconstruction, C Plane, 1 hr after sparge off, July 15, 1993.

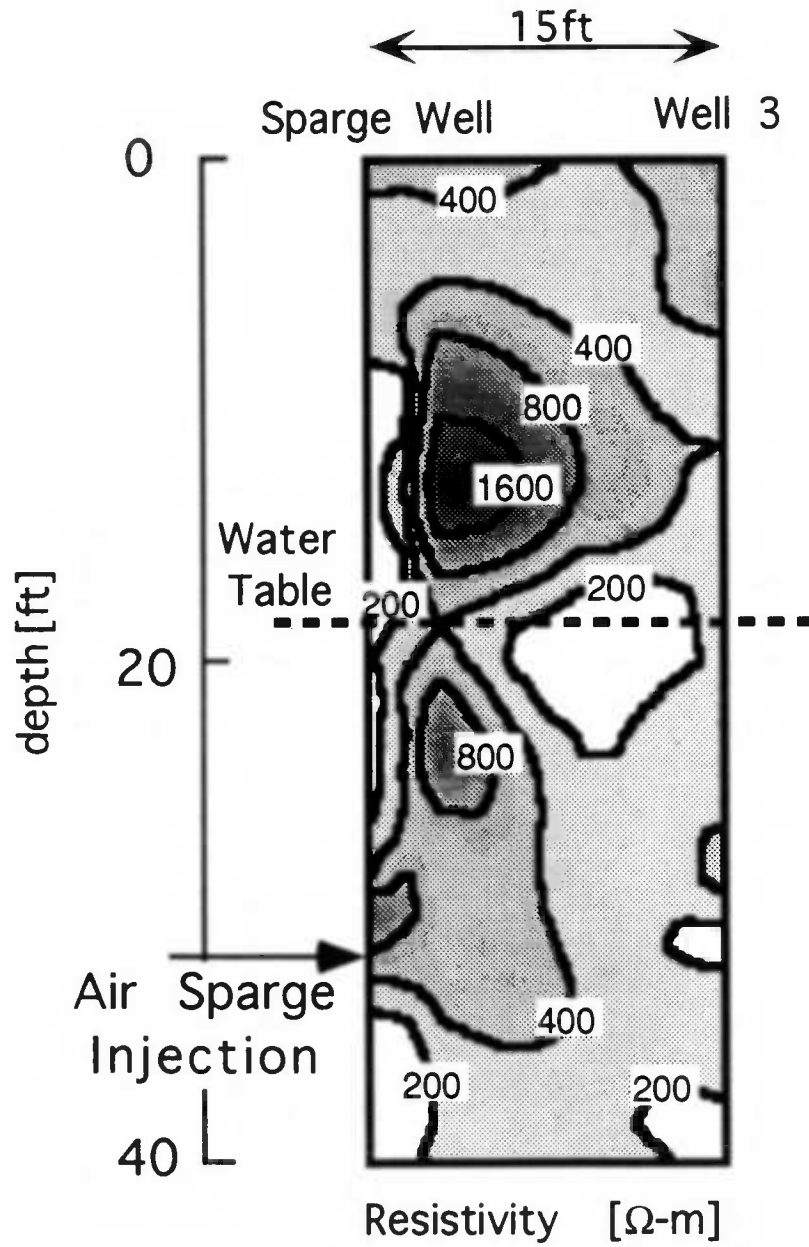


Figure A12. Resistivity reconstruction, C Plane, Background, July 16, 1993.

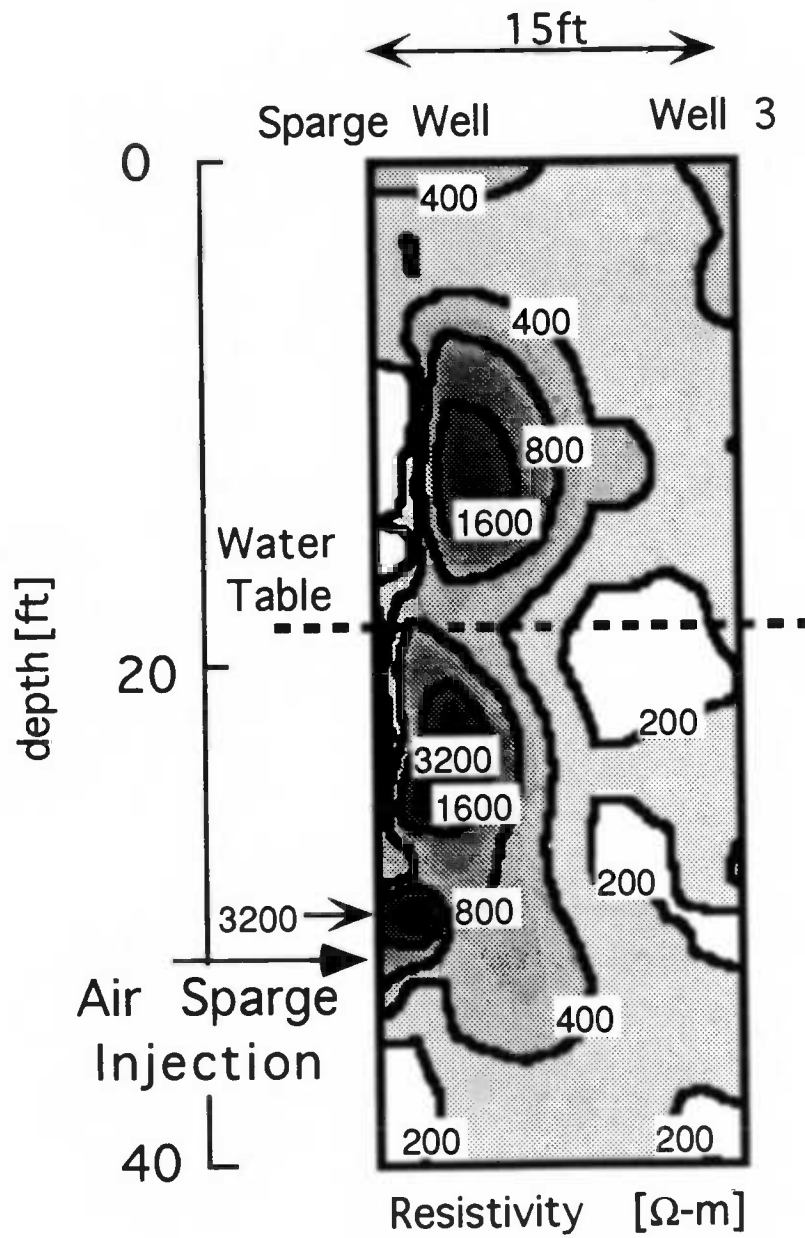


Figure A13. Resistivity reconstruction, C Plane, after 3 half-hour sparge events, July 16, 1993.

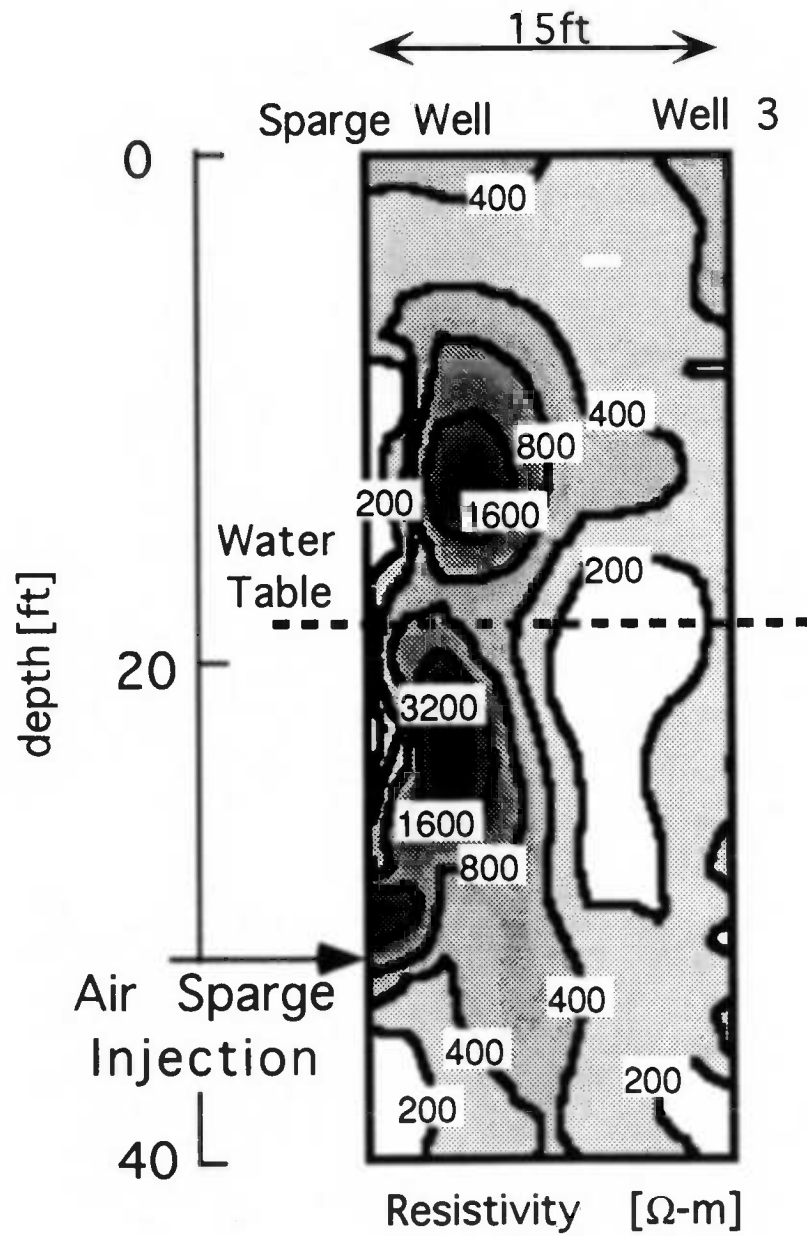


Figure A14. Resistivity reconstruction, C Plane, after about 24 hr of continuous sparging, July 17, 1993.

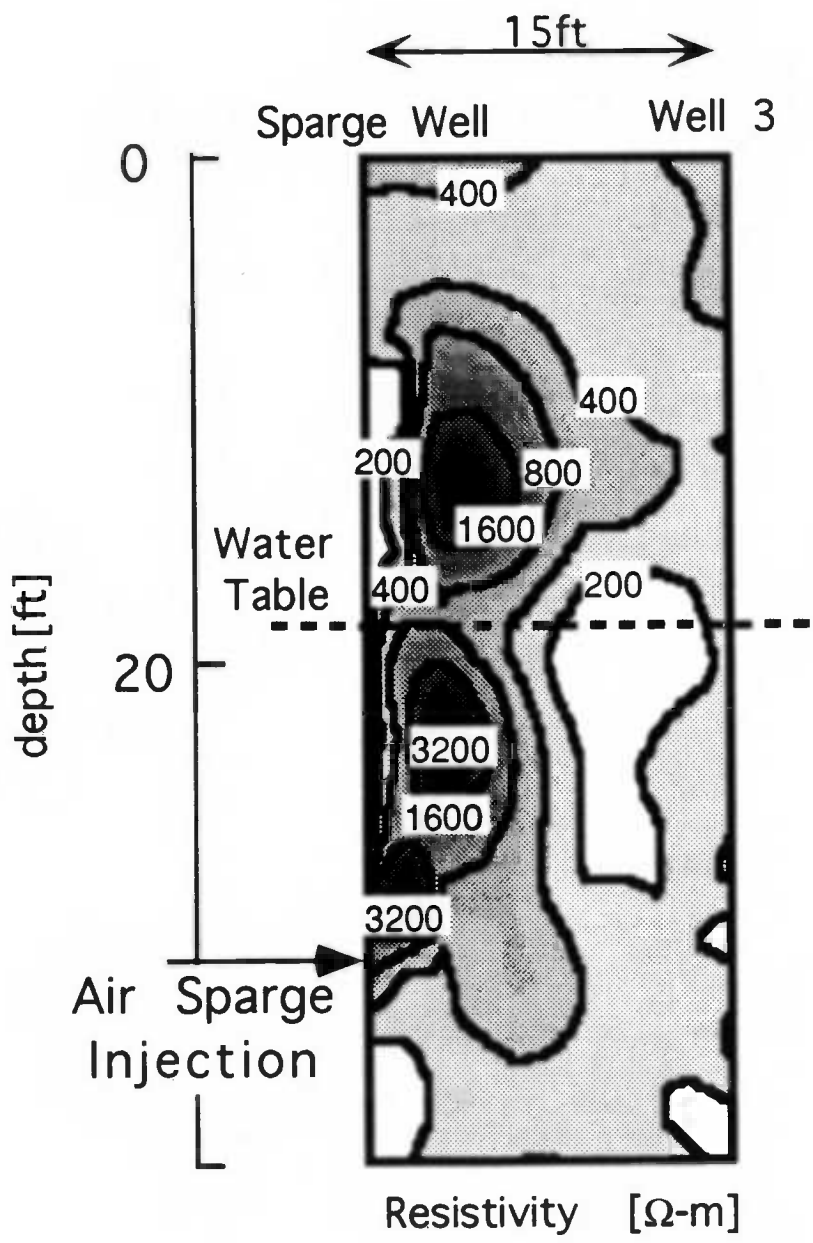


Figure A15. Resistivity reconstruction, C Plane, after about 42 hr of continuous sparging, July 18, 1993.

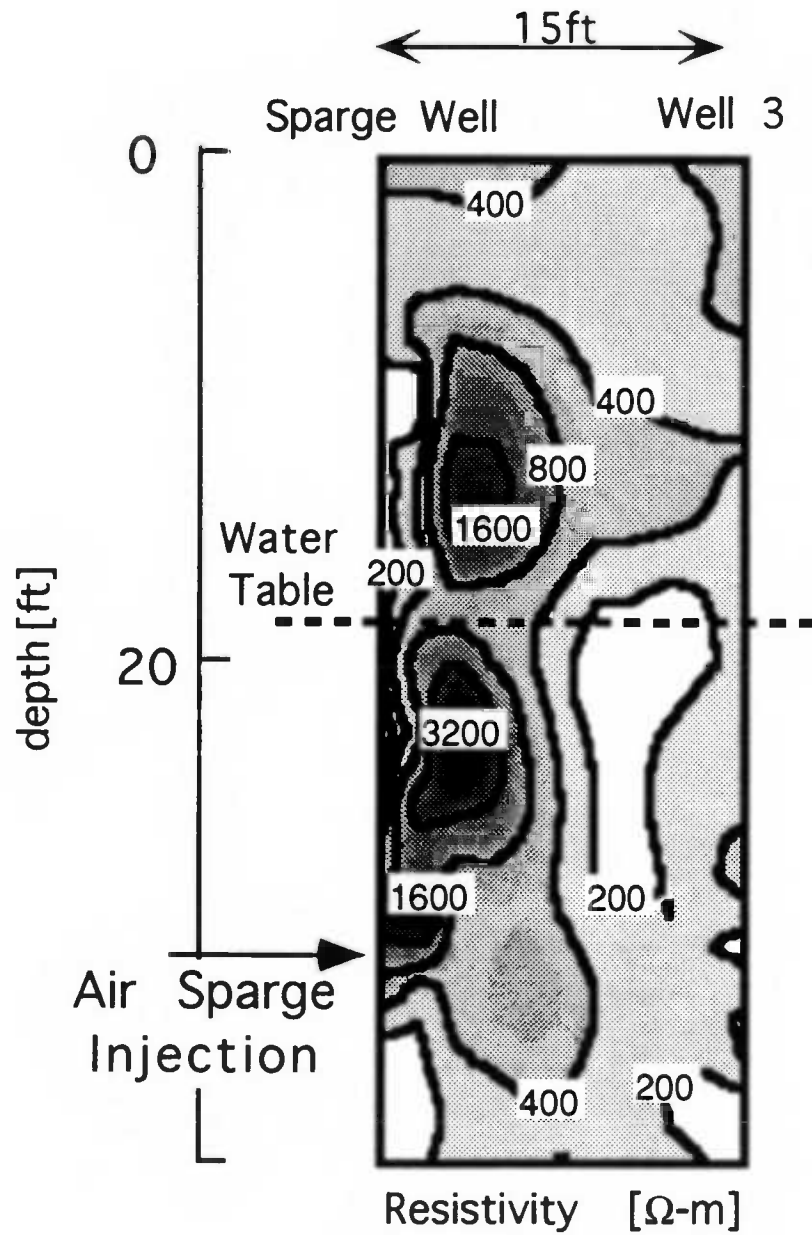


Figure A16. Resistivity reconstruction, C Plane, after about 47 hr of continuous sparging, July 18, 1993.

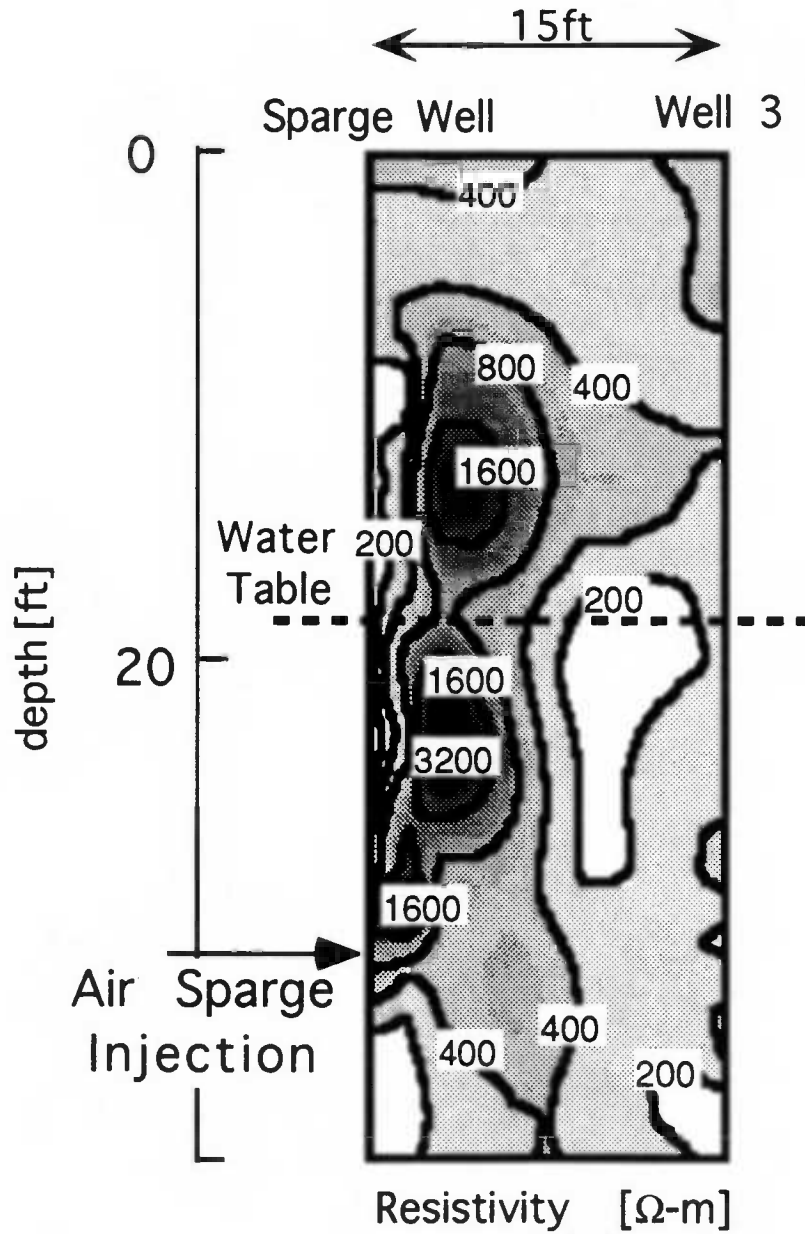


Figure A17. Resistivity reconstruction, C Plane, after about 48 hr of continuous sparging, July 18, 1993.

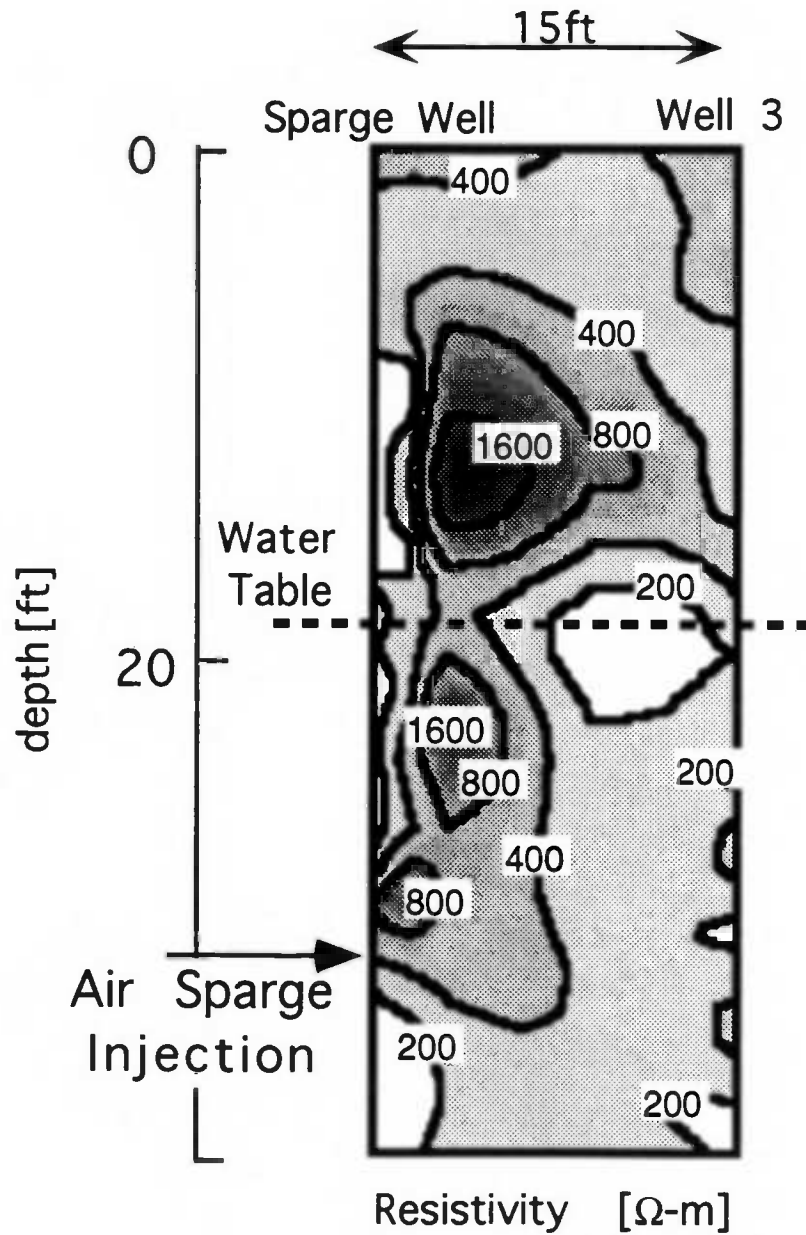


Figure A18. Resistivity reconstruction, C Plane, long term effects after sparge off, July 20, 1993.

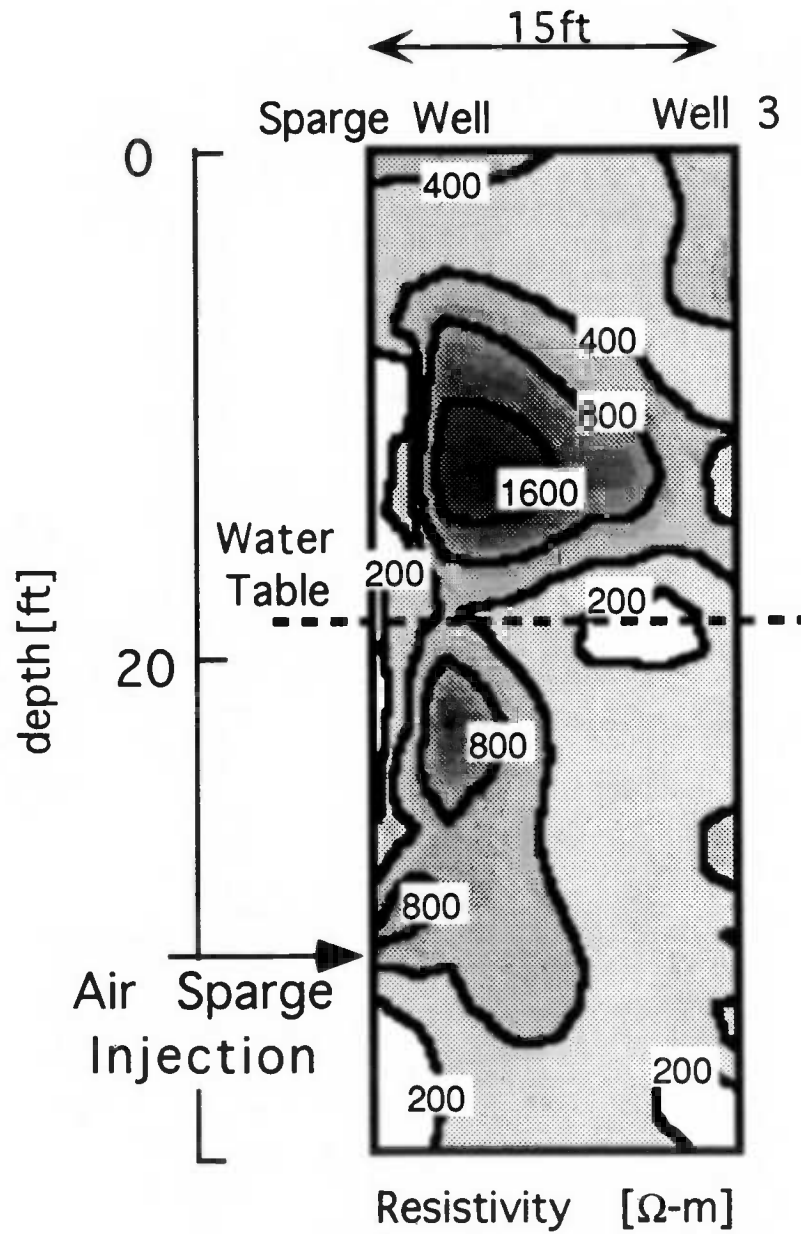


Figure A19. Resistivity reconstruction, C Plane, long term effects after sparge off, July 21, 1993.

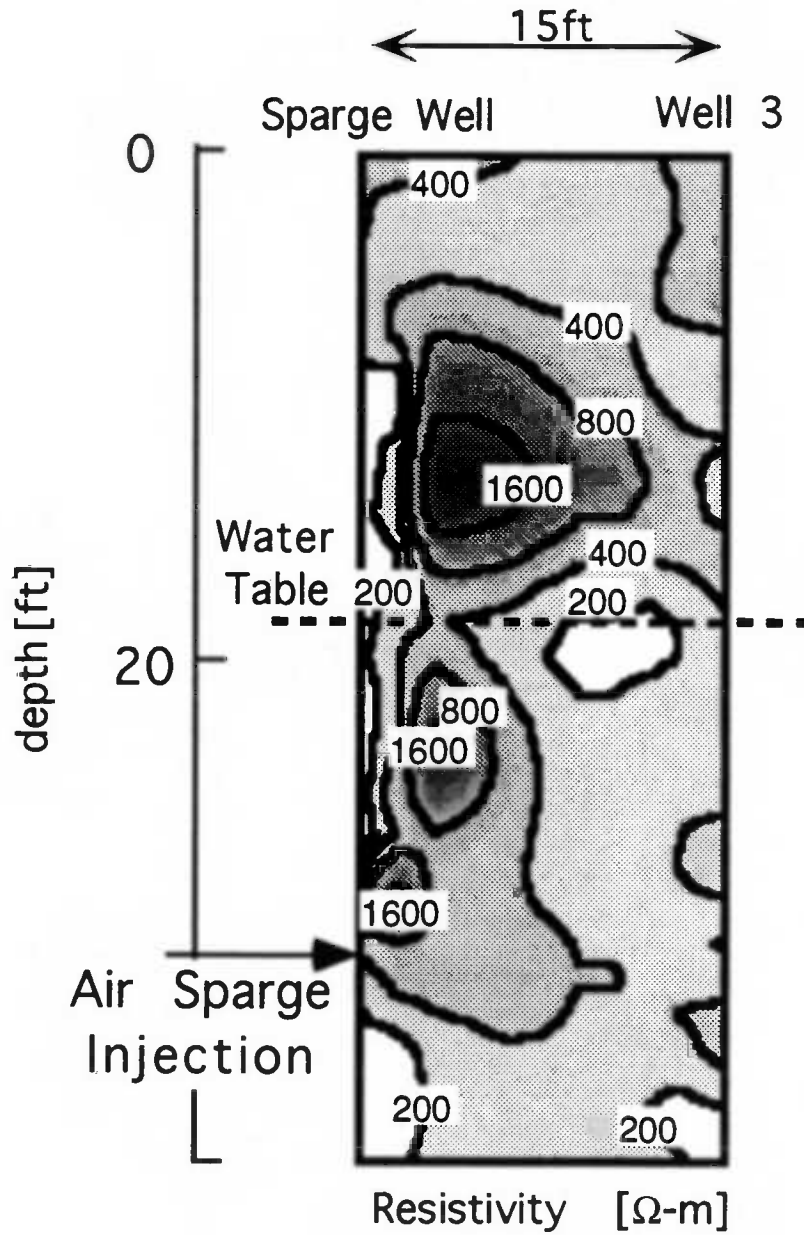


Figure A20. Resistivity reconstruction, C Plane, long term effects after sparge off, July 22, 1993.

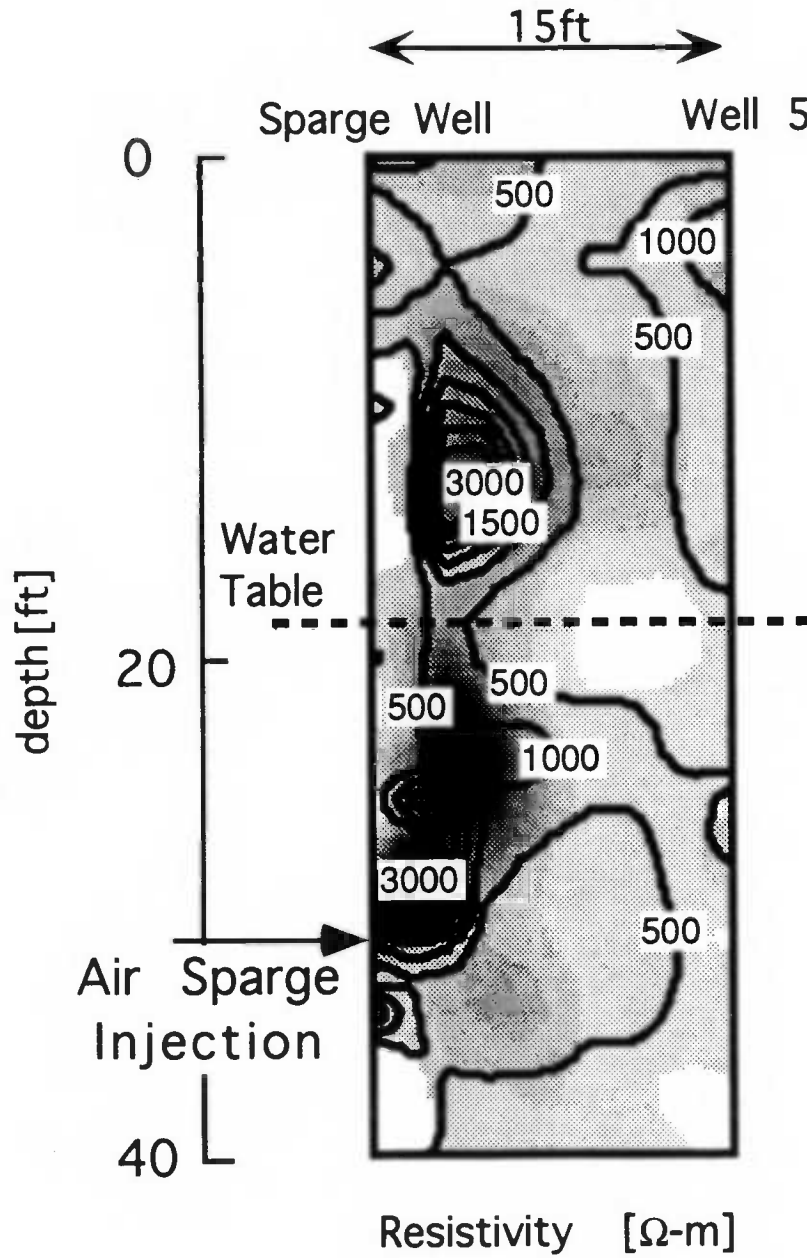


Figure A21. Resistivity reconstruction, H Plane, Background, July 20, 1993.

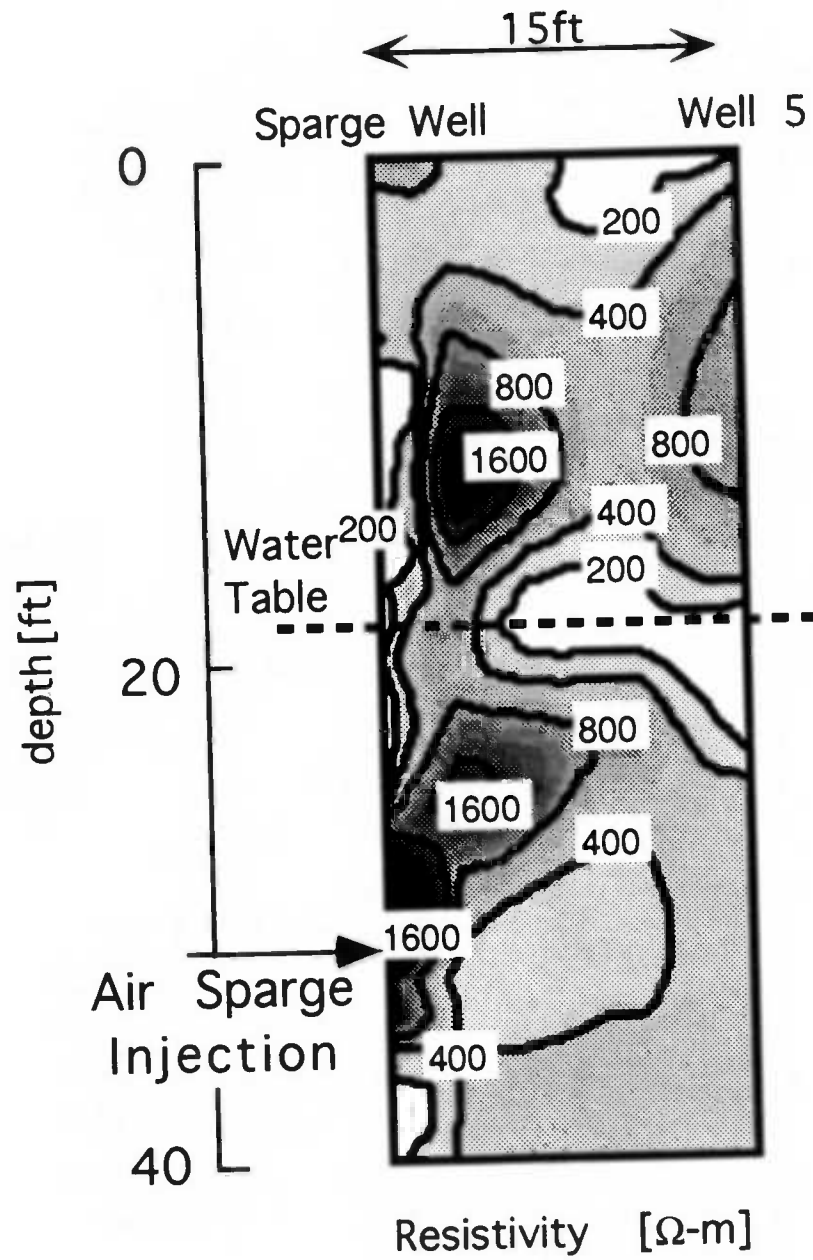


Figure A22. Resistivity reconstruction, H Plane, 10 min after sparge began, July 20, 1993.

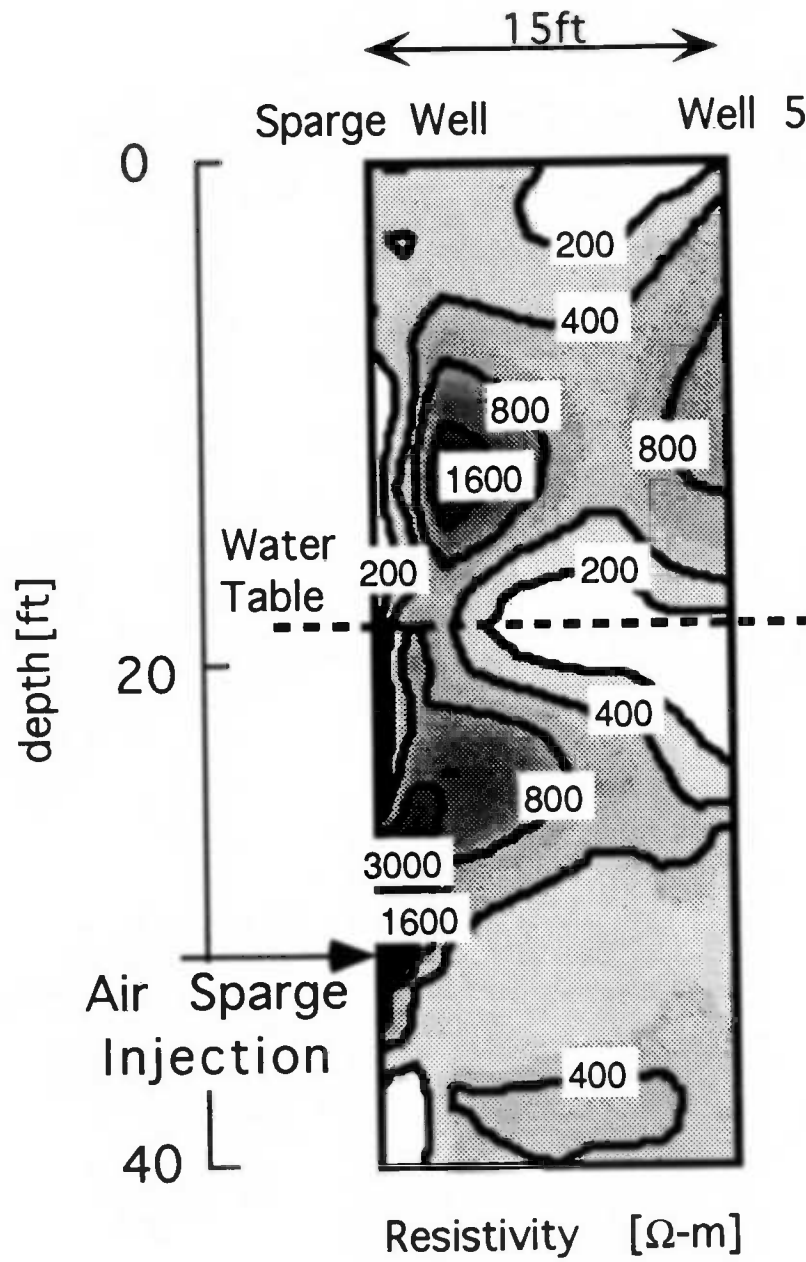


Figure A23. Resistivity reconstruction, H Plane, 20 min after sparge began, July 20, 1993.

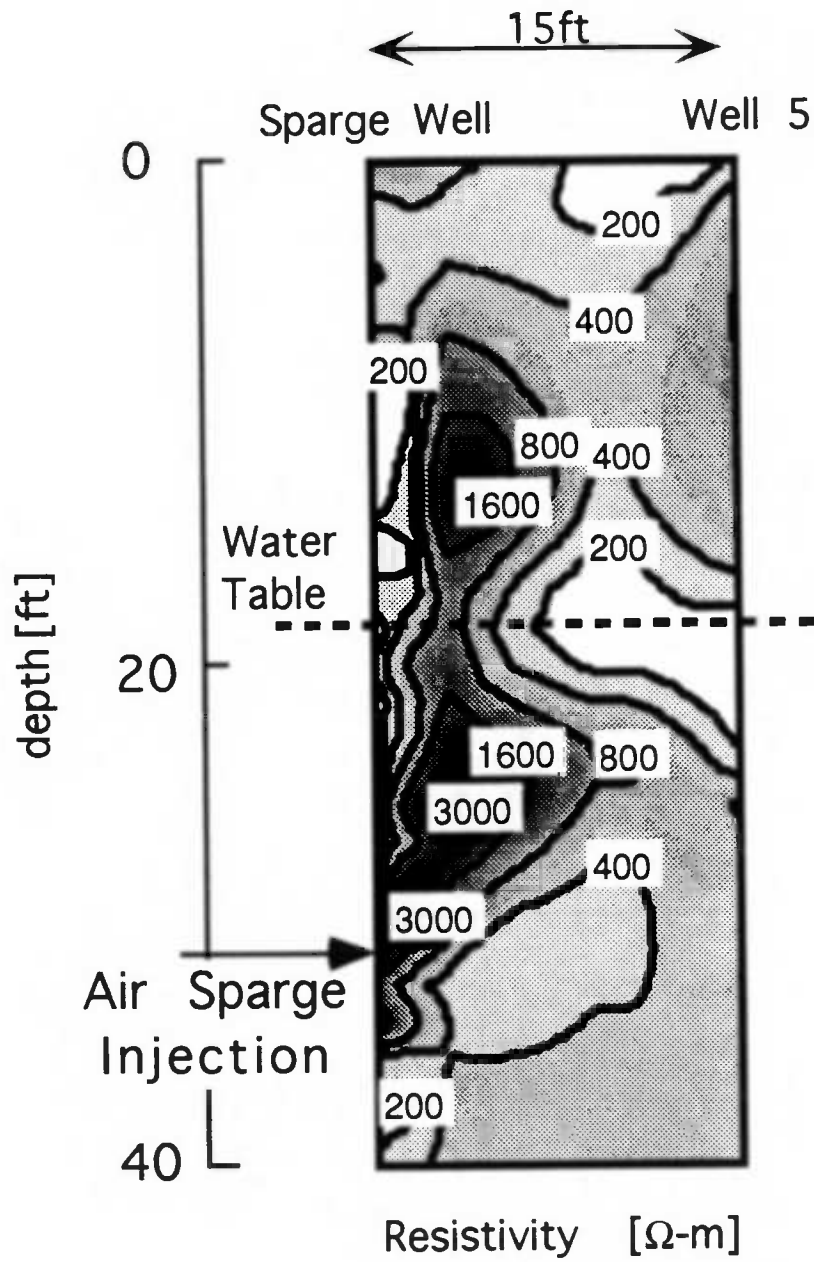


Figure A24. Resistivity reconstruction, H Plane, 1 hr, 30 min after sparge began, July 20, 1993.

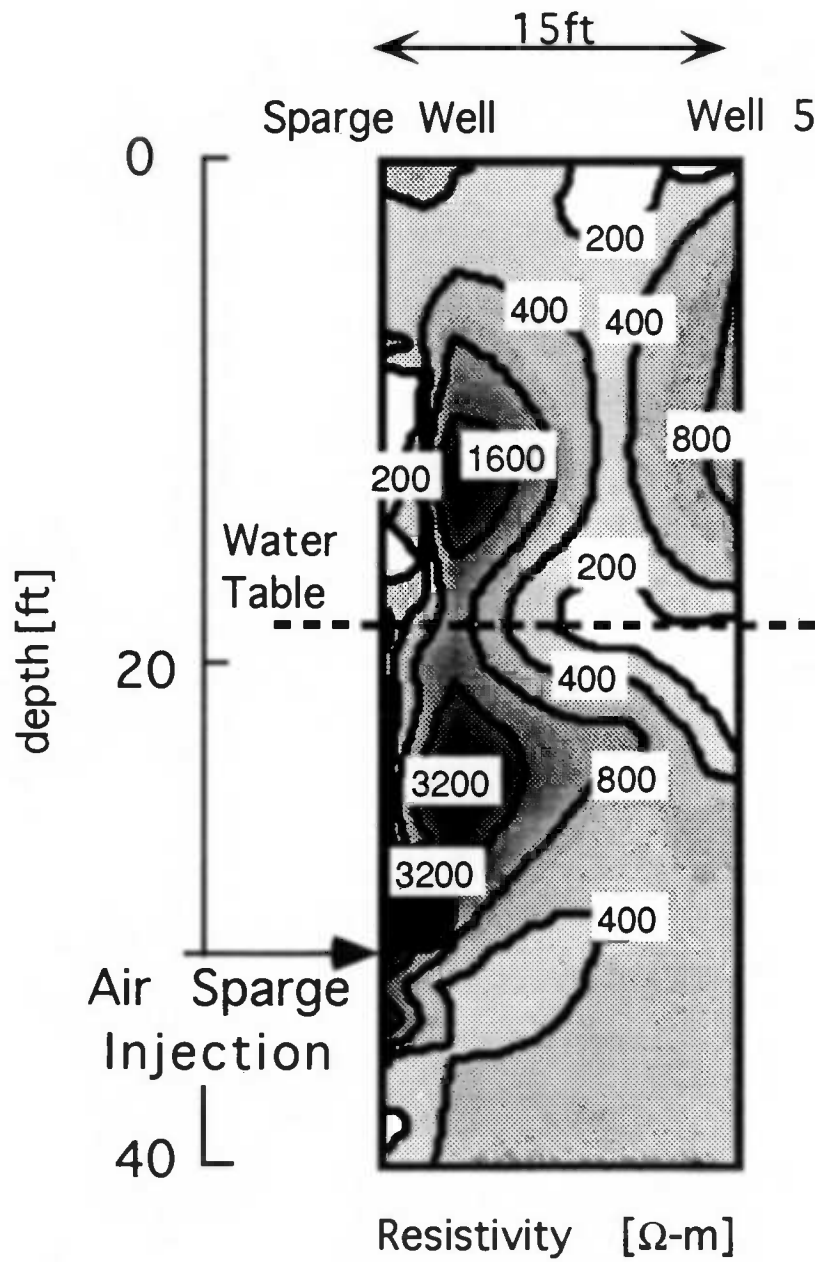


Figure A25. Resistivity reconstruction, H Plane, 2 hr, 20 min after sparge began, July 20, 1993.

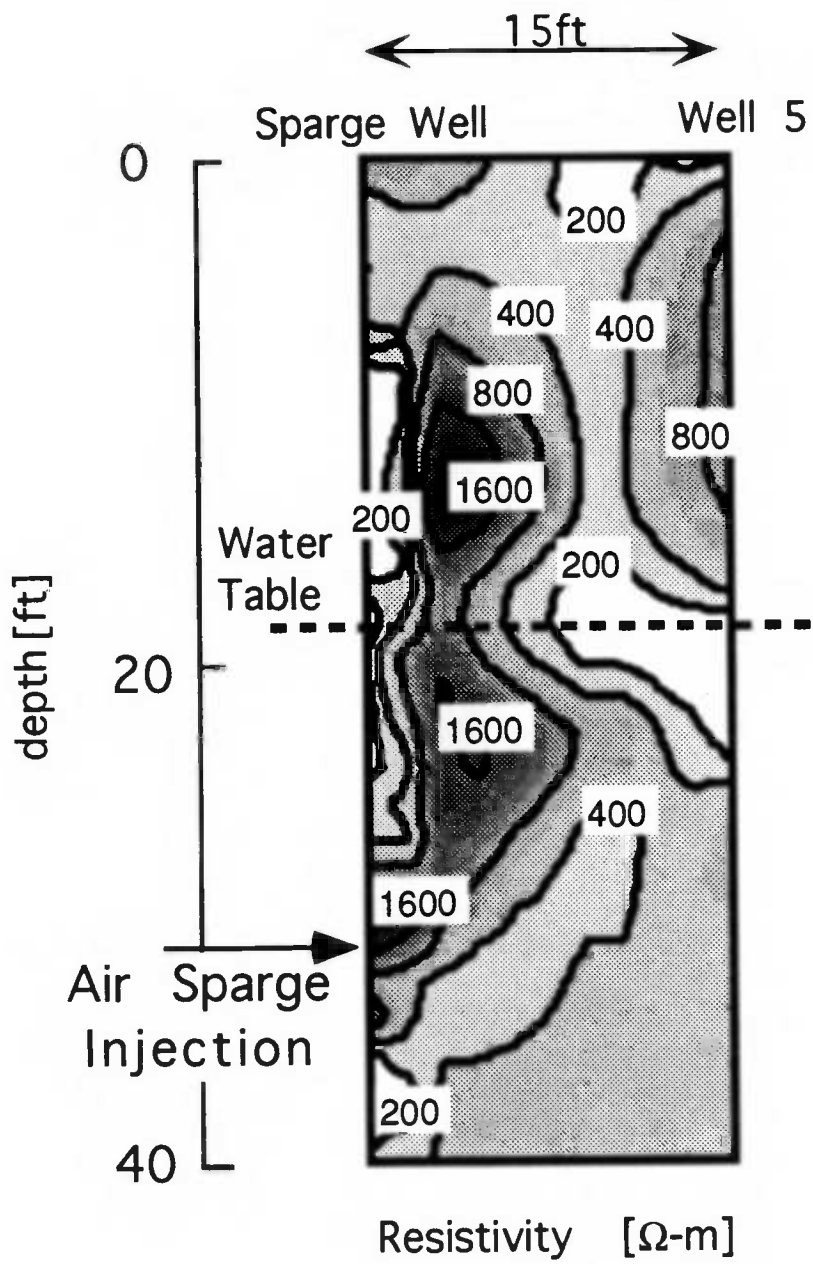


Figure A26. Resistivity reconstruction, H Plane, 10 min after sparge off, July 20, 1993.

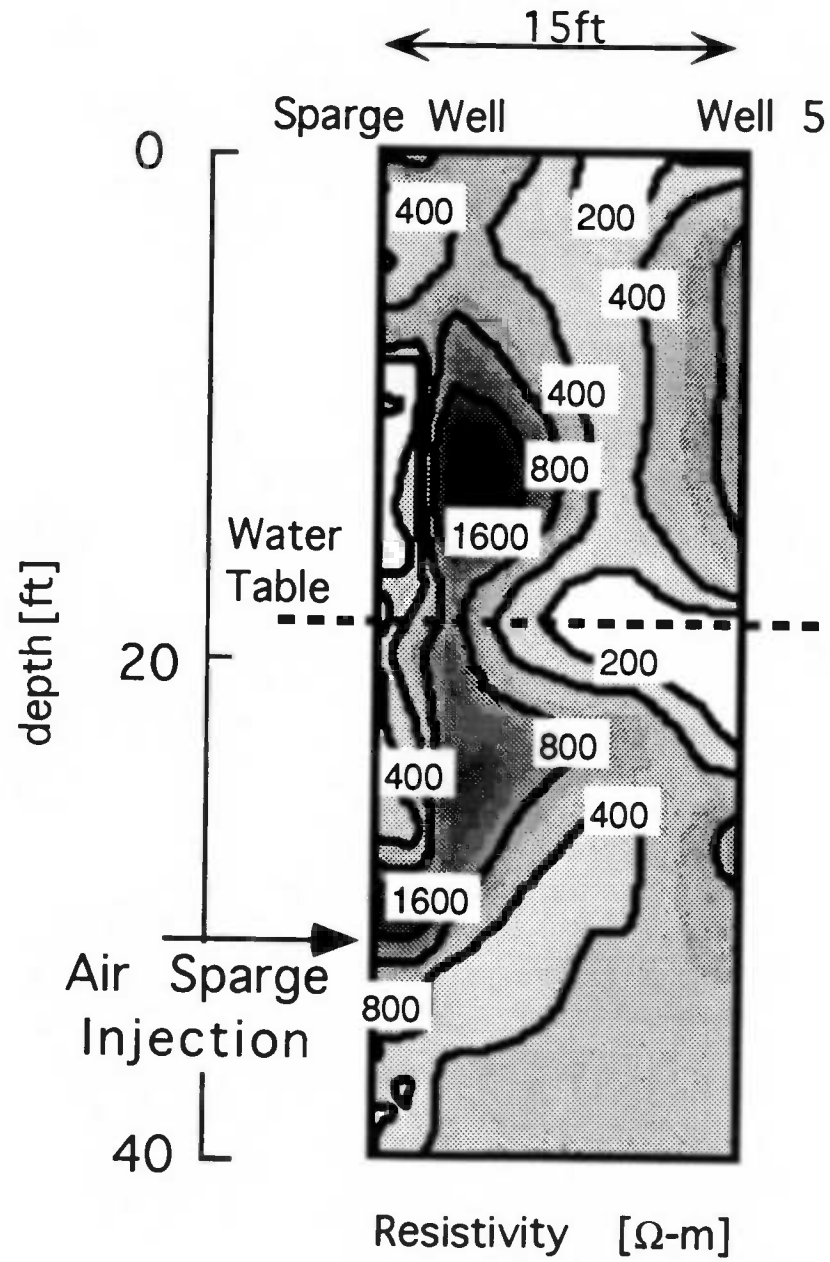


Figure A27. Resistivity reconstruction, H Plane, 20 min after sparge off, July 20, 1993.

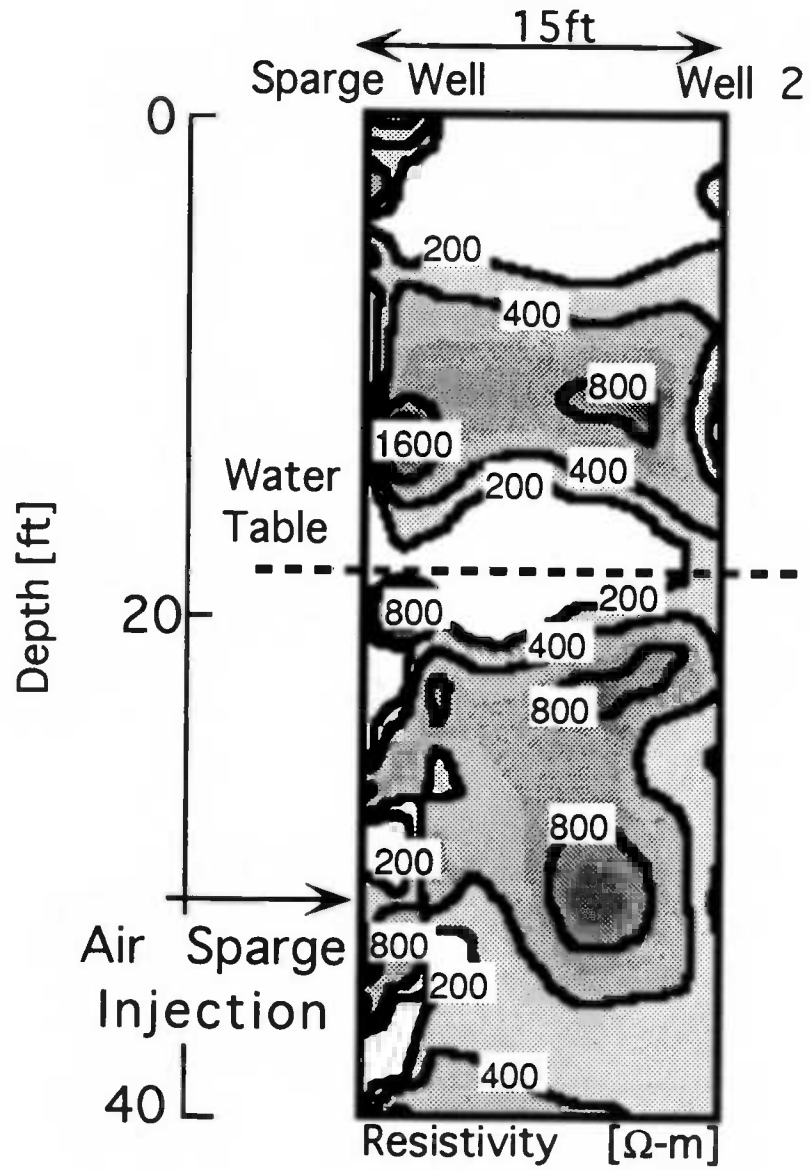


Figure A28. Resistivity reconstruction, B Plane, Background, July 13, 1993.

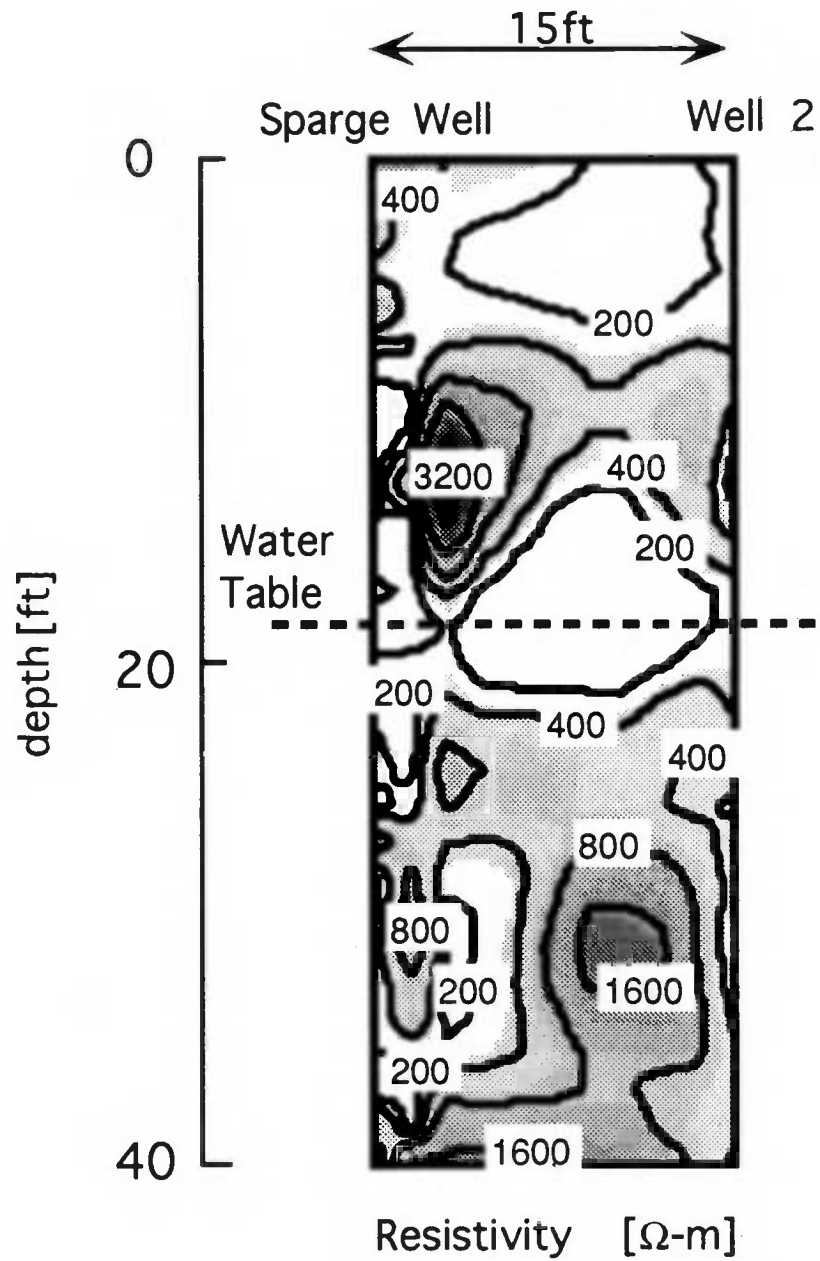


Figure A29. Resistivity reconstruction, B Plane, Background, July 14, 1993.

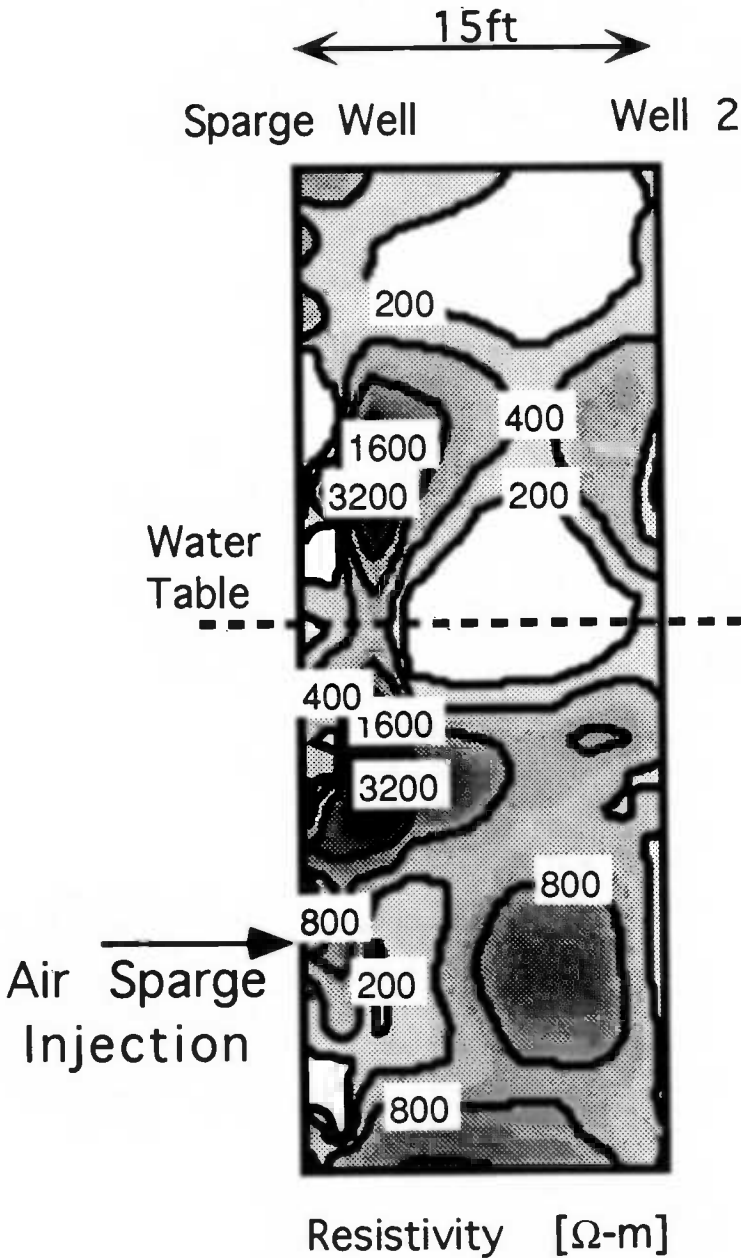


Figure A30. Resistivity reconstruction, B Plane, 1 hr, 30 min after sparge began, July 14, 1993.

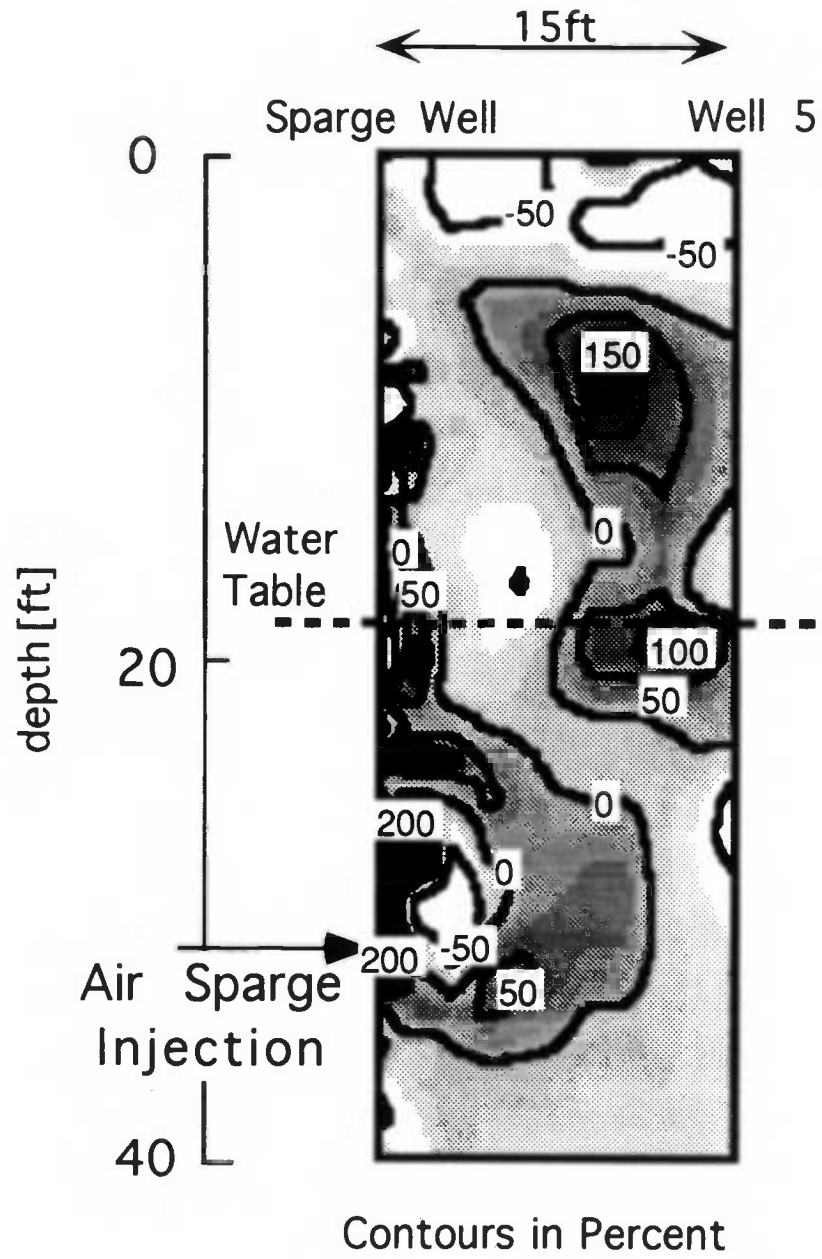


Figure A31. Percent difference reconstruction, H Plane, 10 min after sparge began, July 20, 1993.

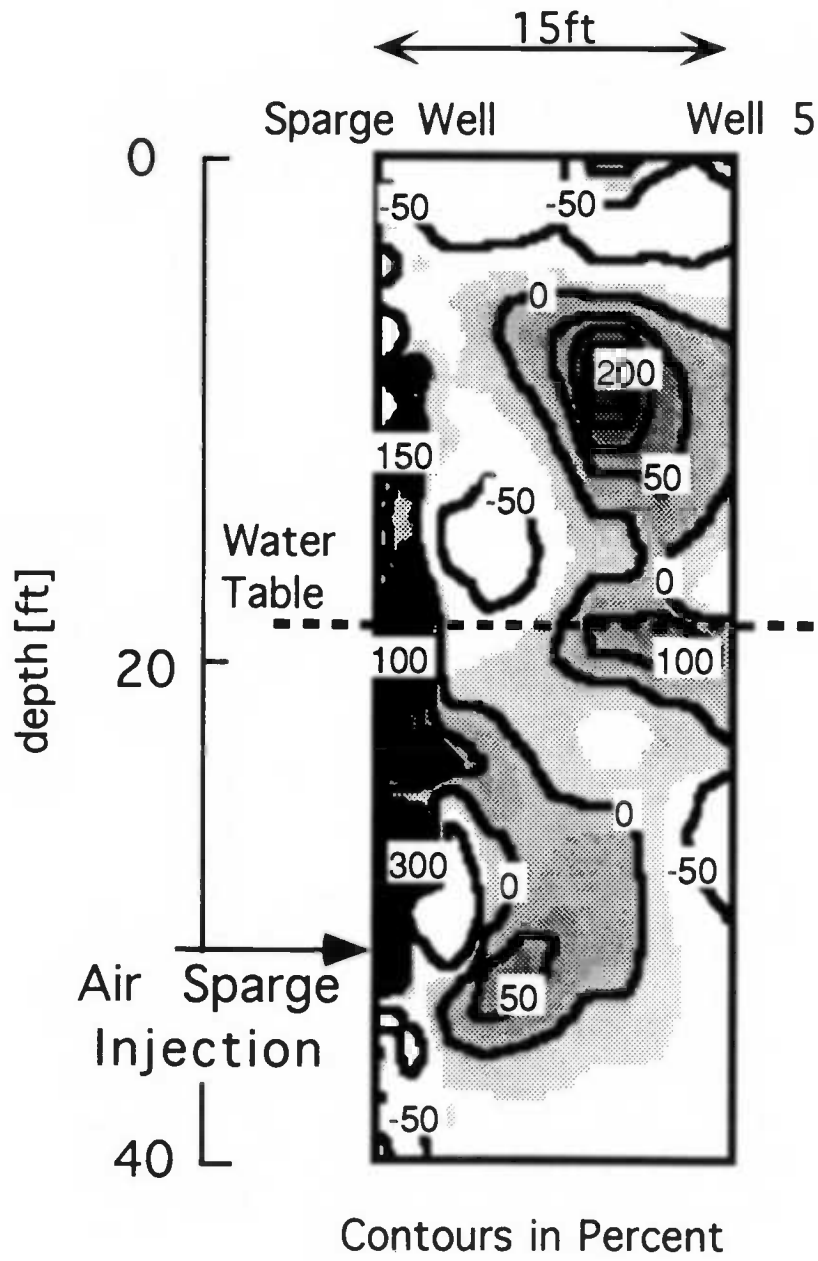


Figure A32. Percent difference reconstruction, H Plane, 20 min after sparge began, July 20, 1993.

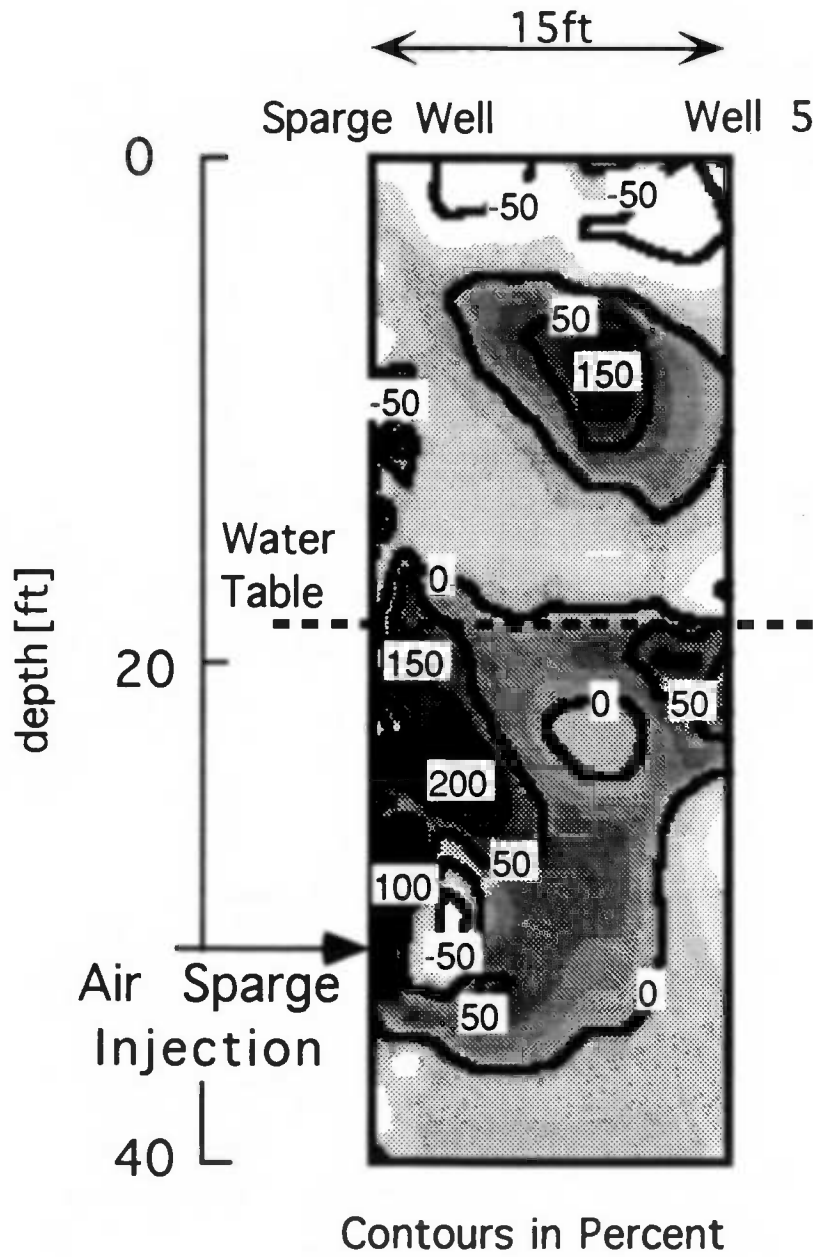


Figure A33. Percent difference reconstruction, H Plane, 1 hr, 30 min after sparge began, July 20, 1993.

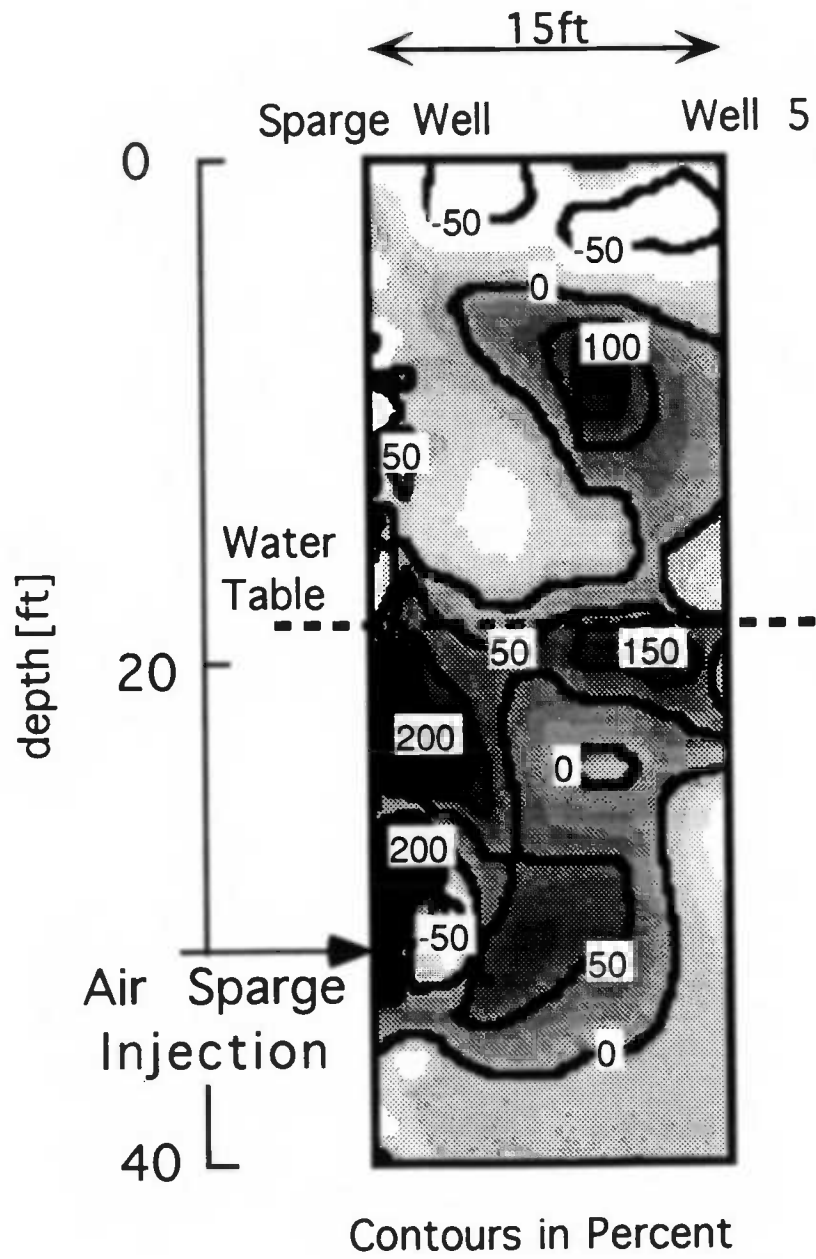


Figure A34. Percent difference reconstruction, H Plane, 2 hr, 20 min after sparge began, July 20, 1993.

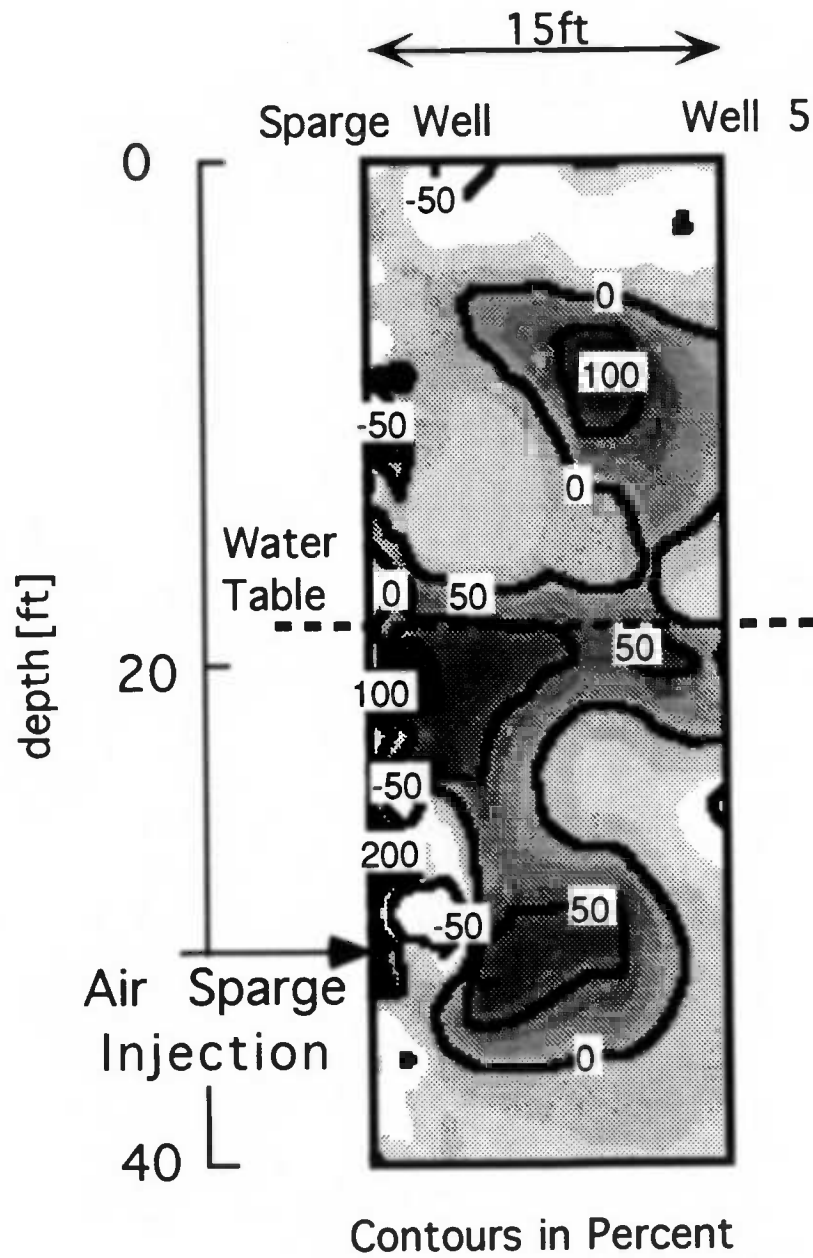


Figure A35. Percent difference reconstruction, H Plane, 10 min after sparge off, July 20, 1993.

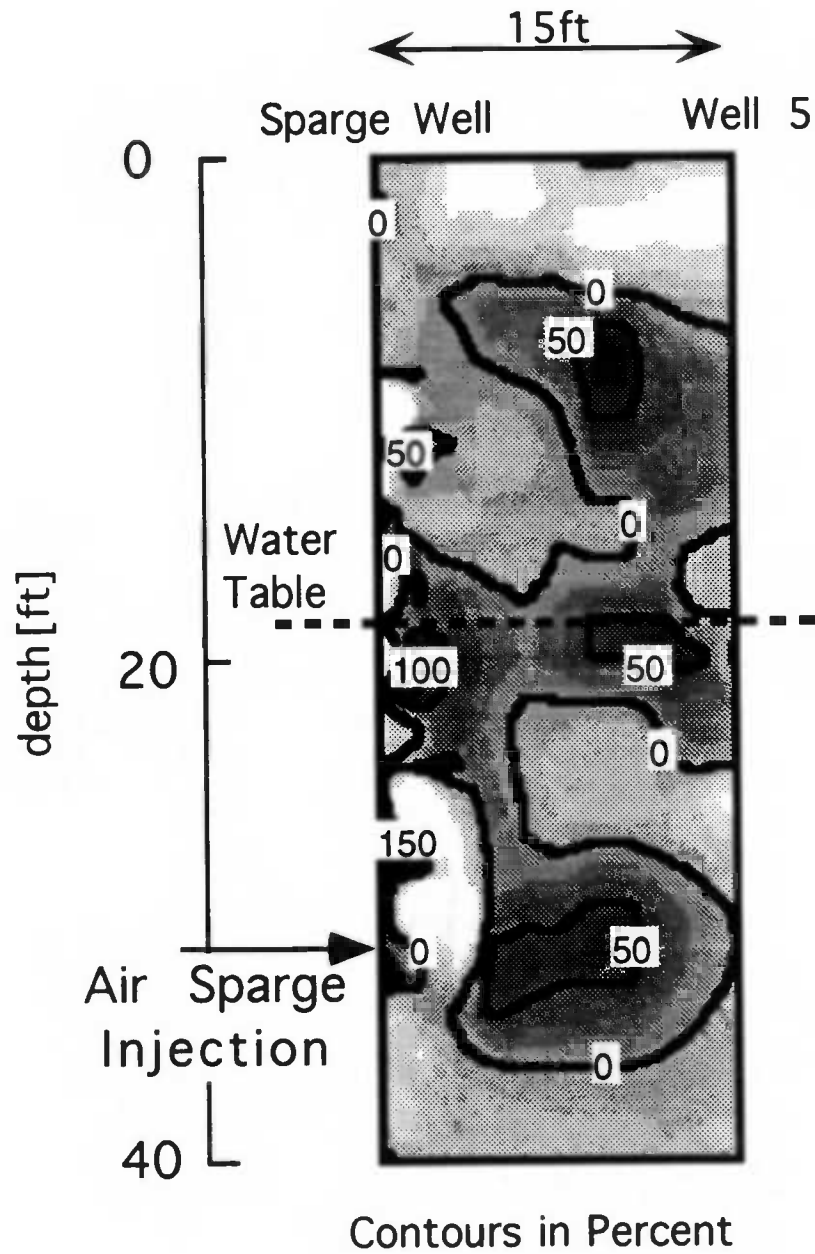


Figure A36. Percent difference reconstruction, H Plane, 20 min after sparge off, July 20, 1993.

REFERENCES

- Brown, R., Herman, C., and Henry, E., 1991, The Use of Aeration in Environmental Clean-ups: Groundwater Technology Inc., Haztech International Pittsburgh Waste Conference, David L. Lawrence Convention Center, Pittsburgh, Pennsylvania, May 14-16.
- Daily, W., Ramirez, A., LaBrecque, D., and Nitao, J., 1992, Electrical Resistance Tomography of Vadose Water Movement: *Water Resources Research*, v. 28, no. 5, p. 1429-1442.
- Doveton, J. H., 1982, Prolog, Kansas Geological Survey.
- Hampton, E. R., 1963, Ground Water in the Coastal Dune Area Near Florence, Oregon: U.S. Geological Survey Water-Supply Paper 1539-K, 36 p.
- Hohmann, G. W., 1988, Numerical Modeling for Electromagnetic Methods in Geophysics, in Nabighian, M. N., Ed., *Electromagnetic Methods in Geophysics*, 1: Society of Exploration Geophysics, Invest. in Geophysics, no. 3, p. 313-363.
- Ji, W., Dahmani, A., Ahlfield, D., Lin, J., and Hill, E., 1993, Laboratory Study of Air Sparging: Air Flow Visualization: *Ground Water Monitoring and Remediation*, v. 13, no. 4, p.115-126.
- Klein, J. D., and Sill, W. R., 1982, Electrical Properties of Artificial Clay-Bearing Sandstone: *Geophysics*, v. 47, no. 11, p. 1593 - 1605.
- LaBrecque, D. J., 1991, IP Tomography: Extended Abstracts of the 61st Annual International SEG Meeting and Symposium, p. 413-416.
- LaBrecque, D. J., Owen, E., Daily, W., and Ramirez, A., 1992, Noise and Occam's Inversion of Resistivity Tomography Data: Extended Abstracts of the 62nd Annual International SEG Meeting and Symposium, p. 397-400.
- Lundegard, P. D., and Anderson, G., 1993, Numerical Simulation of Air Sparging Performance: National Ground Water Association, Dublin, Ohio, Proceedings of Petroleum Hydrocarbons and Organic Chemicals in Ground Water, p. 461-476.
- Maxwell, J. C., 1891, A Treatise on Electricity and Magnetism: Volume 1, Dover Publication, Inc., p. 447-448.
- Nyer, E. K., and Suthersan, S. S., 1993, Air Sparging: Savior of Ground Water Remediations or just Blowing Bubbles in the Bath Tub?: *Ground Water Monitoring and Remediation*, v. 13, no. 4, p. 87-91.

- Ramirez, A., Daily, W., LaBrecque, D., Owen, E., and Chesnut, D., 1993, Monitoring an Underground Steam Injection Process Using Electrical Resistance Tomography: *Water Resources Research*, v. 29, no. 1, p. 73-87.
- Sasaki, Y., 1992, Resolution of Resistivity Tomography Inferred from Numerical Simulation: *Geophysical Prospecting*, 40, p. 453-463.
- Schima, S., LaBrecque, D. J., and Miletto, M., 1993, Tracking Fluid Flow in the Unsaturated Zone Using Cross-Borehole Resistivity and IP: *Proceedings of the Symposium on the Application of Geophysics to Engineering and Environmental Problems*, v. 2, p. 527-543.
- Seigel, H. O., 1959, Mathematical Formulation and Type Curves for Induced Polarization: *Geophysics*, v. 24, no. 3, p. 547-565.
- Shima, H., 1990, Two-dimensional Automatic Resistivity Inversion Technique Using Alpha Centers: *Geophysics*, v. 55, no. 6, p. 682-694.
- Shima, H., and Sakayama, T., 1987, Resistivity Tomography: An Approach to 2-D Resistivity Inverse Problems: *Expanded Abstracts with Biographies*, 57th International SEG Meeting, October 11-15, New Orleans, p. 59-61.
- Sternberg, B. K., Miletto, M. F., LaBrecque, D. J., Thomas, S. J., Poulton, M. M., 1991-1992, The Avra Valley (Ajo Road) Geophysical Test Site: Geophysical Surveys, Geologic Data, and Initial Development of the Test Site: *Laboratory for Advanced Subsurface Imaging Research Report, LASI-91-2*, Department of Mining and Geological Engineering, The University of Arizona, Tucson, Arizona.
- Sternberg, B. K., 1993, A lined Basin for Fluid Injection Experiments: *Electric Power Research Institute (EPRI) Report, Project RP 2485-11*, Laboratory for Advanced Subsurface Imaging (LASI), The University of Arizona, Tucson, Arizona.
- Stollar, R. L., and Roux, P., 1975, Earth Resistivity Surveys - A Method for Defining Ground-Water Contamination: *Groundwater*, v. 13, no. 2, p. 145-150.
- Vinegar, H. J., and Waxman, M. H., 1984, Induced Polarization of Shaly Sands: *Geophysics*, v. 49, no. 8, p. 1267 - 1287.
- Waxman, M. H., and Smits, L. J. M., 1968, Electrical Conductivities in Oil-Bearing Shaly Sands: *Society of Petroleum Engineers Journal*, June, p. 107 - 122.
- Waxman, M. H., and Thomas, E. C., 1974, Electrical Conductivities in Shaly Sands - I. The Relation Between Hydrocarbon Saturation and Resistivity Index; II. The Temperature Coefficient of Electrical Conductivity: *Journal of Petroleum Technology*, v. 26, p. 213-225.